Chapter 4A

Effect of Operating Conditions on Pyrolysis of *Tithonia Diversifolia*: Distribution and Characterization of Products

4A.1 Introduction

Various invasive plant species available in different regions are considered a threat to the biodiversity of that particular area. It's ability to spread quickly into the ecosystems is linked to adverse consequences like damage to agricultural ecosystems which affects food production, breakdown of natural ecosystems, and alteration of the survival of different species through competition or predation [3, 4]. *Tithonia diversifolia* (TD) or Mexican sunflower, is such an invasive weed species often seen in neglected farmlands, vacant lots, roadside areas, field margins, riverbanks, etc. [3, 5, 6]. Investigations have been performed on biofuel production from different invasive weeds such as *Ageratum conyzoides*, *Prosopis juliflora*, *Sachharum ravanae*, *Parthenium*, algae, and different aquatic biomasses such as duckweed, *Ipomea carnea,* water hyacinth, etc. [7-10]. While no previous literature deals with the thermochemical (pyrolytic) conversion of *Tithonia diversifolia* into bio-oil and other products, its wide abundance throughout the world makes it a potential candidate to explore its suitability for pyrolytic valorization. The objective of the current study is to investigate this biomass to explore its potentiality for sustainable energy, as well as biomaterials/chemicals production. Also in this chapter, an attempt has been made to assess the effect of process parameters on both the product distribution as well as their physicochemical characteristics.

4A.2 Physicochemical Characterization of Biomass

Table 4.1 depicts proximate and ultimate analyses results for TD biomass. Thermal conversion efficiency and heating value of biomass are highly dependent on moisture content (MC), which directly affects the energy value during storage. The MC of *T. diversifolia* was found to be low (6.26±0.21%), indicating its suitability for thermal processing such as combustion and pyrolysis [11-13]. TD biomass possessed high volatile matter (VM) contents i.e., 70.25±0.36% which shows its high reactivity and is a suitable property for achieving high power output during combustion [11]. A smaller amount of ash content (AC) (7.04±0.09 %) of the feedstock favors the thermochemical conversion process [13, 14]. The fixed carbon (FC) content (16.45±0.39%) is not particularly high, suggesting a fuel source with a significant portion of volatile matter that burns readily. However, this value alone does not definitively indicate exhaustion during thermochemical conversion. While low FC content can be associated with fuels that burn quickly, other factors, such as process conditions, also play a crucial role in determining how much fuel is consumed [13].

Table 4.1: Physicochemical characterization of biomass

Proximate Analysis (%)		Ultimate Analysis (%)	
Moisture (MC)	6.26±0.21	Carbon (C)	42.69
Volatile matter (VM)	70.25±0.36	Hydrogen (H)	5.85
Ash content (AC)	7.04±0.09	Nitrogen (N)	0.93
Fixed carbon (FC)	16.45±0.39	Oxygen (O)	51.53
Calorific Value (MJ/kg)	15.95		

During the ultimate analyses of TD, the nitrogen content was found to be as low as 0.93%, which means lower NO_x emission during combustion [7]. The obtained calorific value for the feedstock is 15.95 MJ/kg, which is comparable to few other lignocellulosic biomass such as tamarind residues [15], jackfruit wastes [16], etc. These results indicate the suitability of the feedstock for the thermochemical conversion process like pyrolysis. These findings are indicative of feedstock's suitability for the thermochemical conversion process.

The biochemical analysis of the TD biomass is shown in **Table 4.2**. For the TD biomass, cellulose (42.58 %) was the predominant component while both the hemicellulose (20.06 %) and lignin (21.21 %) content was in a similar range. The results from this study suggest that the TD biomass is a promising candidate for thermochemical conversion processes such as pyrolysis.

Table 4.2: Bio-chemical characteristics of biomass

Biochemical properties	
Components	**Wt. (%)**
Hemicellulose	20.06
Cellulose	42.58
Lignin	18.21
Extractive	19.15

4A.3 Fourier Transform Infrared Spectroscopy (FTIR) Analysis of Biomass

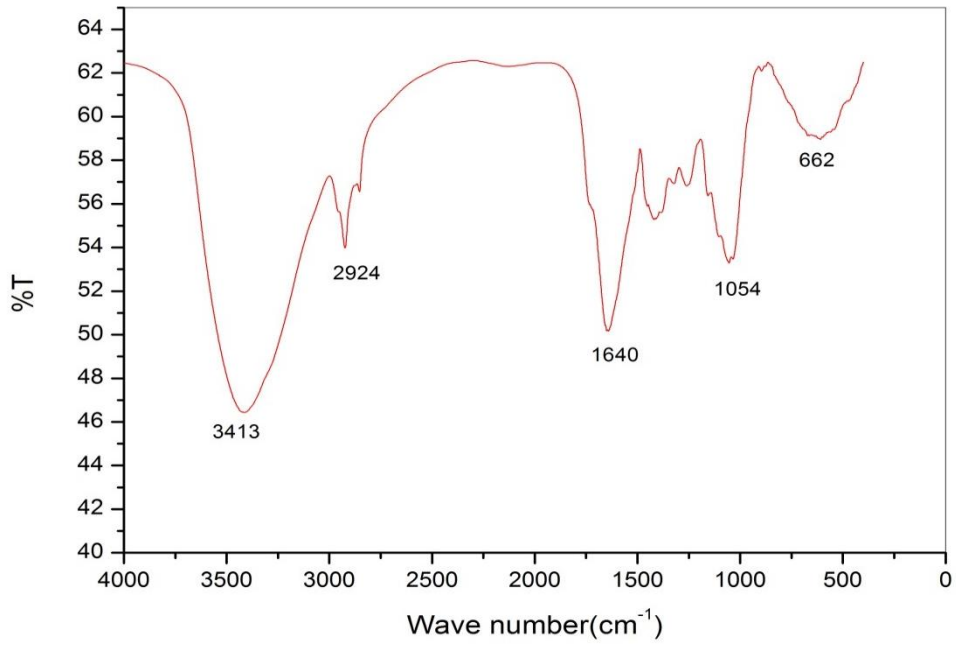

Fig. 4.1: Spectroscopic Analysis of Biomass

The spectroscopic characterization of TD is depicted in **Fig. 4.1**, which shows the presence of some significant functional groups of bioenergy relevance in TD. The wide band at 3413 cm^{-1} is related to O-H stretching vibrations of bonded and non-bonded hydroxyl groups from the glucoside linkages of cellulose or the hydroxyphenyl, guaiacyl, and syringyl groups of lignin or water [47]. The band around 2924 cm^{-1} is identified with stretching vibrations of the aliphatic C-H bond. These peaks around 3400 and between 2960-2850 cm^{-1} are also observed for other biomass such as paddy straw, spent mushroom straw, and *Parthenium hysterophorus* [17]. The band at 1640 cm^{-1} is ascribed to C=C vibrations in aromatic rings of lignin. The band at 1415 cm^{-1} is attributed to the presence of CH_2 groups in cellulose and lignin. The peak in the spectral region at 1250 cm^{-1} suggests the presence of C–H and O–H bending vibrations, indicating the presence of lignin. Similar observations have been reported for other biomass types, such as forest residues, energy crops, and agricultural residues [48]. The fingerprint region is more complex due to the presence of cellulosic materials in biomass. This region was mainly dominated by C–H, N–O, and O–H vibrations [17]. The broad peak at 662 cm^{-1} may be due to the β-glycosidic linkage between sugar units of cellulose and hemicellulose.

4A.4 Effects of Operating Parameters on Products Yield

4A.4.1 Temperature (T)

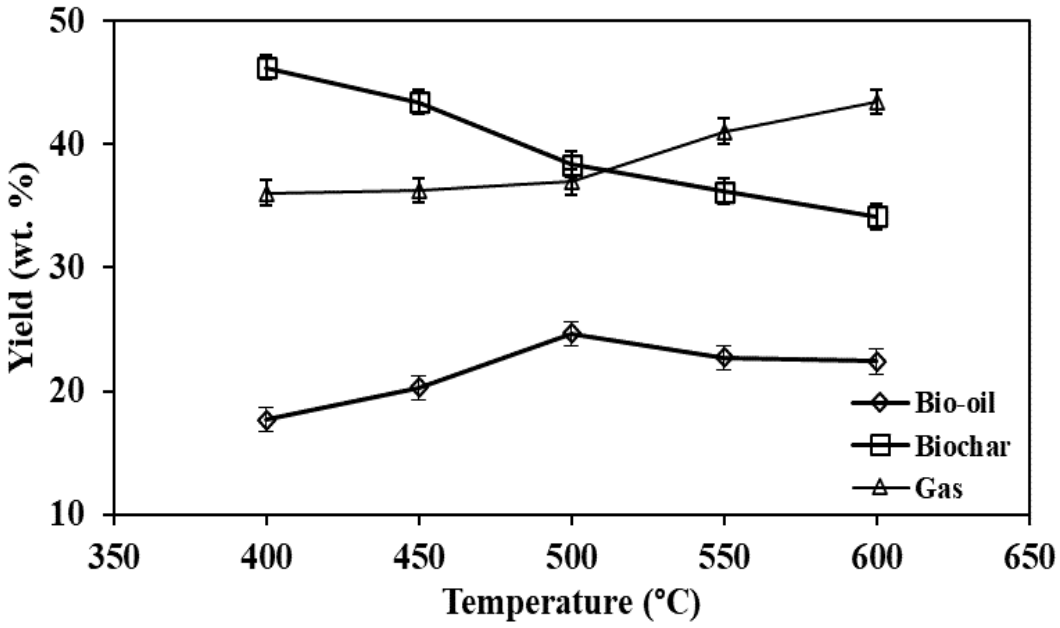

Fig. 4.2: Effect of temperature on pyrolysis product yield

Fig. 4.2, represents the effect of temperature on product yield. In this study, it was noticed that the biochar yield gradually decreased from 46.25±0.05 wt.% to 34.15±0.20 wt.% as T increased from 400 ºC to 600 ºC. Production of char (or char path) was more favored or dominated at lower temperatures which was similar to the findings of various researchers [18, 19]. VM exhaustion due to the higher breakdown of organic matter at a high temperature could explain the decrease in biochar generation at those temperatures. Another cause of this reduction is the char residues' secondary decomposition at elevated temperatures [30]**.**

At moderate T, higher bio-oil generation took place which is depicted in **Fig. 4.2** (*Table S1 in appendices)*. At T= 400°C, 17.65±0.09 wt.% of bio-oil was obtained which increased to 24.64±0.06 wt.% at 500°C. However, bio-oil yield reduced to 22.72±0.10 and 22.4±0.11wt.% with the further increase in pyrolysis temperature to 550 °C and 600 °C respectively, which may be ascribed to secondary cracking reactions [45]. At T> 500 °C, secondary reactions of condensable vapors occur, which contribute to the enhancement of the gas yield [18, 19]. The gas yield increased from 36.09±0.14 wt.% at 400 °C to 43.45±0.31 wt.% at 600 °C.

4A.4.2 Heating Rate (HR)

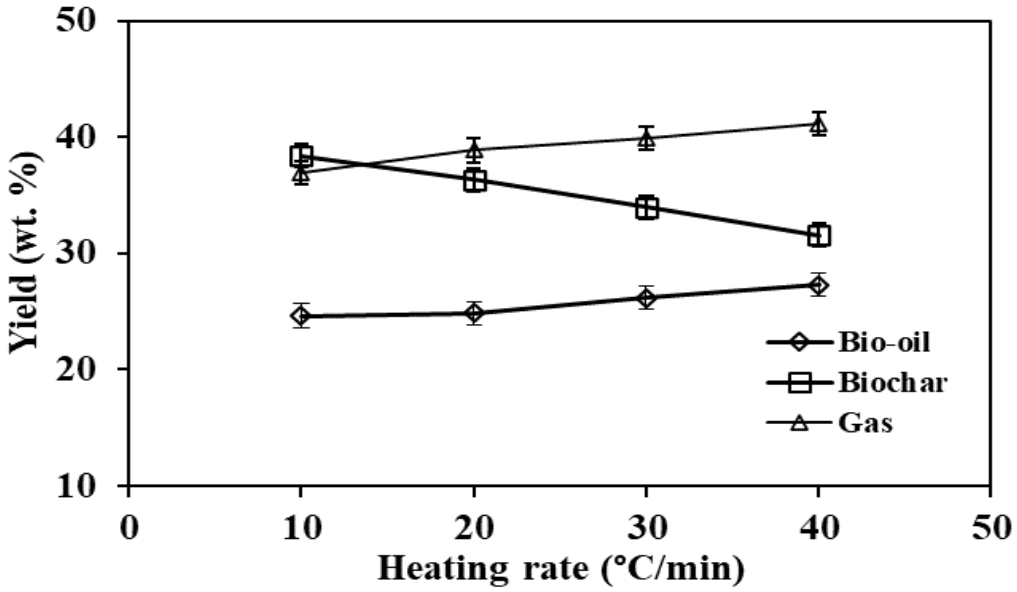

Fig.4.3: Effect of heating rate on pyrolysis product yield

Fig. 4.3 (*Table S2 in appendices*) illustrates that a lower heating rate of 10 °C min^{-1} resulted in a lower gas and liquid yields, concomitant with an increase in char yield. This phenomenon can be attributed to the incomplete pyrolysis of biomass at lower heating rates. The lower production of liquid fuels at low HRs is due to resistance toward heat as well as mass transfer within biomass. As HR increases, this constraint is overcome and as a result, higher conversion rates and a higher yield of bio-oil are observed [21]. Additionally, a higher HR causes faster depolymerization of solid material to primary volatile components, resulting in a decrease in biochar production [20]. Furthermore, as the HR was increased the occurrence of a faster endothermic degradation of biomass leads to high gas yield [22]. The highest bio-oil yield was obtained at the HR of 40 °C min^{-1} and is considered as optimum among all the HRs employed in the current investigation.

4A.4.3 Particle Size (PS)

Fig. **4.4** illustrates the consequences of the PS on product distribution (*Table S3 in appendices)*. The highest bio-oil yield of 27.63±0.05 wt% was achieved at 0.25-0.5 mm particle sizes, which is attributed to the high heat and mass transfer that results in complete biomass conversion. There is a minor rise in bio-oil yield obtained from PS of less than 0.25 mm (27.28±0.2 wt%).

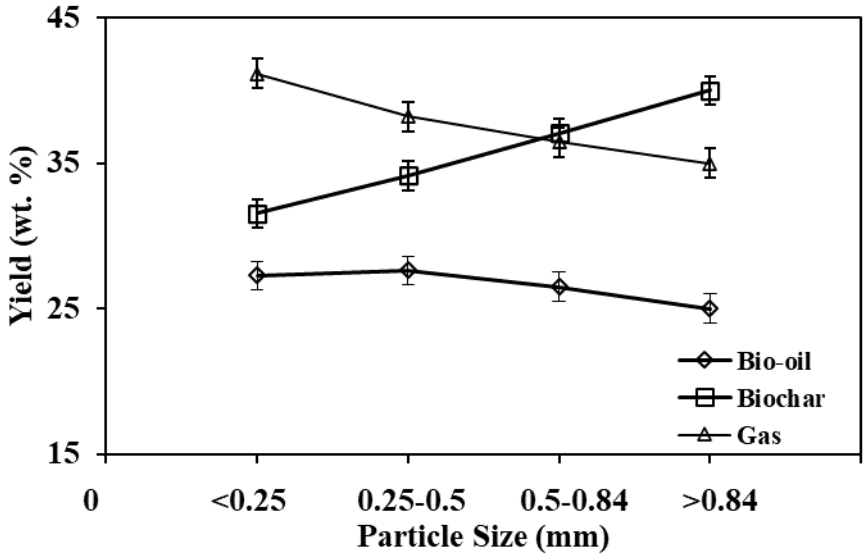

Fig.4.4: Effect of particle size on pyrolysis product yield

As the PS increases from 0.25-0.50 mm to >0.84mm, bio-oil yield decreases. Reduced heat and mass transfer within larger particles at lower heating rates hinders complete pyrolysis. This results in lower bio-oil yields and higher char yields, as the biomass may not reach the temperatures necessary for complete devolatilization [23, 24].

The smaller PS is also favourable for higher gas formation, which reduced gradually with the increase in PS of less than 0.25 mm (41.16±0.12 wt.%) to a PS of greater than 0.84 mm (35±0.06 wt.%). A high gas yield is a result of the breakdown of larger molecules into smaller ones, facilitated by extended residence times for volatiles within the reactor. This is particularly evident when biomass with smaller particle sizes is used, as it receives more heat within the reactor and promotes the condensable vapors into gases [25].

Whereas, with the increase of PS from <0.25 mm to >0.84 mm, the char yield increased from 31.55±0.12 to 40±0.04 wt.%. The highest bio-oil production was achieved for this biomass with PS between 0.25-0.50 mm, and may be considered as the most suitable PS range for liquid fuel production which is consistent with reported literature [26].

4A.4.3 Inert Gas Flow Rate (NFR)

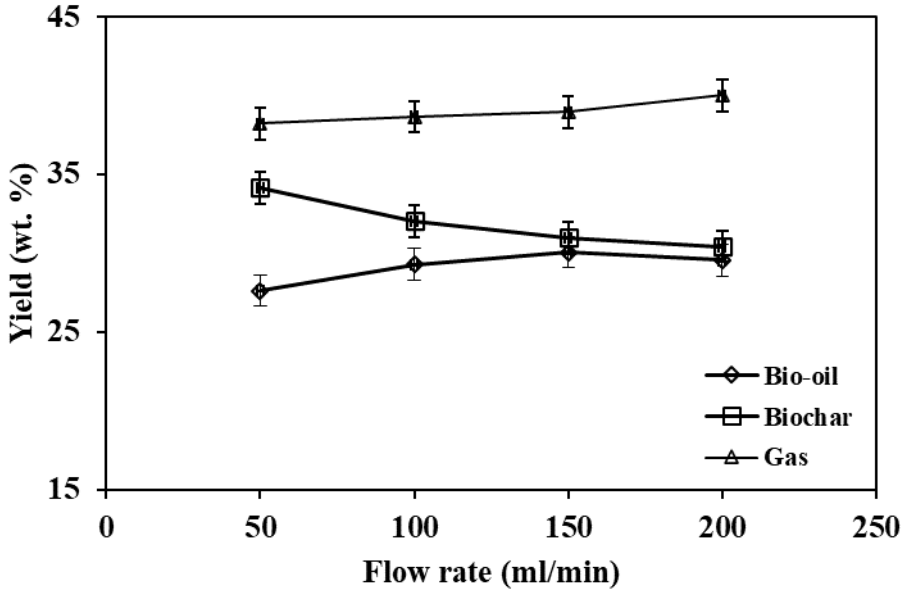

Fig.4.5: Effect of N_2 gas Flow Rate on Pyrolysis Product Yield

Fig. 4.5 and **Table S4** (*in appendices*) depicts the pyrolytic product yield versus NFR. During the study, it was observed that the NFR had also an affirmative influence on bio-oil yield from 50-150 ml/min. The bio-oil yield rises from 27.63±0.05 wt % (FR= 50 ml/min) to a maximum of 30.16±0.09 wt % (150 ml/min) and then reduced to 29.56±0.40 wt % for the FR, 200 ml/min. This bio-oil yield reduction with the NFR increases from 150 to 200 ml/min was reportedly due to the lack of sufficient time for condensation of the hot vapors by the cooling condenser in the system. The higher NFR reduces the pyrolysis vapors' residence time inside the reactor, and that leads to the discontinuation of chemical reactions, thereby inhibiting the degradation of the valuable initial reaction products [26].

4A.5 Product Characterization

4A.5.1 Physicochemical Characterization of Bio-oil

Physico-chemical characteristics of bio-oil obtained from *T. diversifolia* has been shown in **Table 4.3**. Elemental analysis depicts low oxygen content (42.85 %) of the bio-oil compared to raw biomass feedstock (51.53 %). Oxygen content is an influential factor since higher oxygen content lowers bio-oil's HHV than the transportation fuel [27]. The HHV of bio-oil was 23.84 MJ/kg which is lower than the HHV of diesel as the O content of bio-oil was much higher than that of diesel [28]. The high O content in bio-oil necessitates its upgradation. Bio-oil's higher amount of C (48.75 %) and H (7.25 %) in

comparison to the raw biomass feedstock (42.69 % and 5.85 %) indicate the higher energy density of bio-oil [29]. Bio-oil's H/C molar ratio of 1.78 is quite similar to that of petroleum products (1.5 to 2.0) [28].

Table 4.3: Physico-chemical analysis of TD bio-oil

Properties	**Methods**	**Value**
Appearance		Dark brownish color
Density, @15 °C (kg/m^3)	ASTM D1298-99	1008
Viscosity (cP)		86.1
Pour point (°C)	ASTM D5853-09	+8
Cloud point (°C)	ASTM D1310-01(2007)	20
Fire point (°C)	ASTM D1310-01(2007)	57
Flash point (°C)	ASTM D6450-05(2010)	45
Calorific value (MJ/kg)		23.84

Ultimate analysis					
O	N	H	C	H/C	O/C
42.85	1.15	7.25	48.75	1.78	0.66

Density, viscosity, and flash point are considered standard properties for various combustion applications. The bio-oil's density was higher (1008 kg/m^3) in comparison to that of the transportation fuels (820-860 kg/m^3 at 15 °C). The higher density of bio-oil can be attributed to its complex chemical composition, including high-molecular-weight oxygenated compounds, and its inherent water content. The high density of bio-oil is disadvantageous which severely affects the engine's pumping and injection processes at low temperatures and therefore, blending of bio-oil with transportation fuels is essential for its use as a transportation fuel [30]. Bio-oil was more viscous than diesel fuel [31]. However, the higher flash point of bio-oils (45 °C) ensures its safe storage, and the pour point (8 °C) of bio-oils is ideal for many environmental conditions [21].

4A.5.2 FTIR Analysis of Bio-Oil

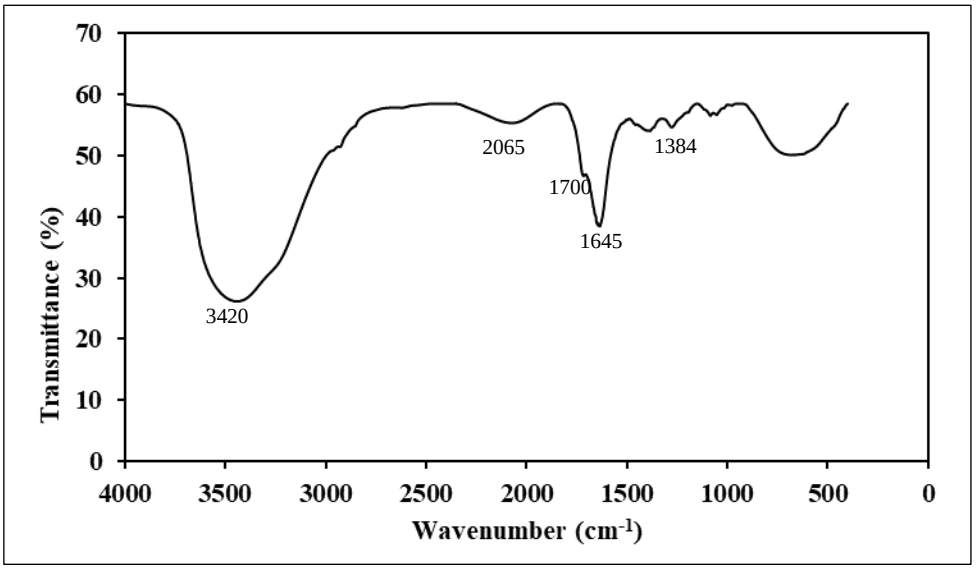

Fig. 4.6: FTIR of TD Bio-oil

Bio-oil consists of a large number of complex organic chemicals. **Fig. 4.6** depicts the FTIR spectra of TD bio-oil obtained under the process conditions that produced the maximum bio-oil yield. The broad O–H absorption peak at 3420 cm^{-1} indicates the presence of phenolic and alcoholic compounds [32]. A weak, broad peak at 2065 cm^{-1} suggests the presence of alkynes or cyanide groups. These peaks are also observed in bio-oil derived from biomass such as coir pith [49]. However, the characteristic peak of methylene or the stretching vibration of alkanes, typically observed in the region 2850–2900 cm^{-1}, is absent in TD bio-oil. In contrast, bio-oil from other feedstocks, such as coir pith and perennial grass (*Arundo donax L.*), exhibits peaks in this region [12]. The peak at 1700 cm^{-1} suggests the presence of carbonyl groups, which may be attributed to ester or carboxylic acid structures [33]. The presence of alkenes and aromatic compounds is indicated by the C=C stretching vibration at 1640 cm^{-1}. This peak is comparable to the peak observed for coir pith at 1602 cm^{-1} and for freshwater algae (*Spirogyra*) at 1556.55 cm^{-1} [49, 50]. Peaks in the region 1300–950 cm^{-1} may result from O–H bending and C–O stretching, indicating the presence of primary, secondary, and tertiary alcohols, as well as phenols [32]. The C–H deformation vibration band at 1384 cm^{-1} is indicative of alkanes. Additionally, absorption peaks between 900–650 cm^{-1} and 1610–1420 cm^{-1} suggest the presence of mono-, polycyclic, and substituted aromatic groups [34]. These peaks are also observed in the FTIR spectra of bio-oils derived from *Arundo donax L.*, coir pith, and various other biomass feedstocks. While the overall spectral features of TD bio-oil are largely similar to those of bio-oils derived from other biomass sources, such as coir pith

and *Arundo donax*, subtle differences in peak intensities and positions can be attributed to variations in the composition of the feedstock.

4A.5.3 ^{1}H NMR Analysis

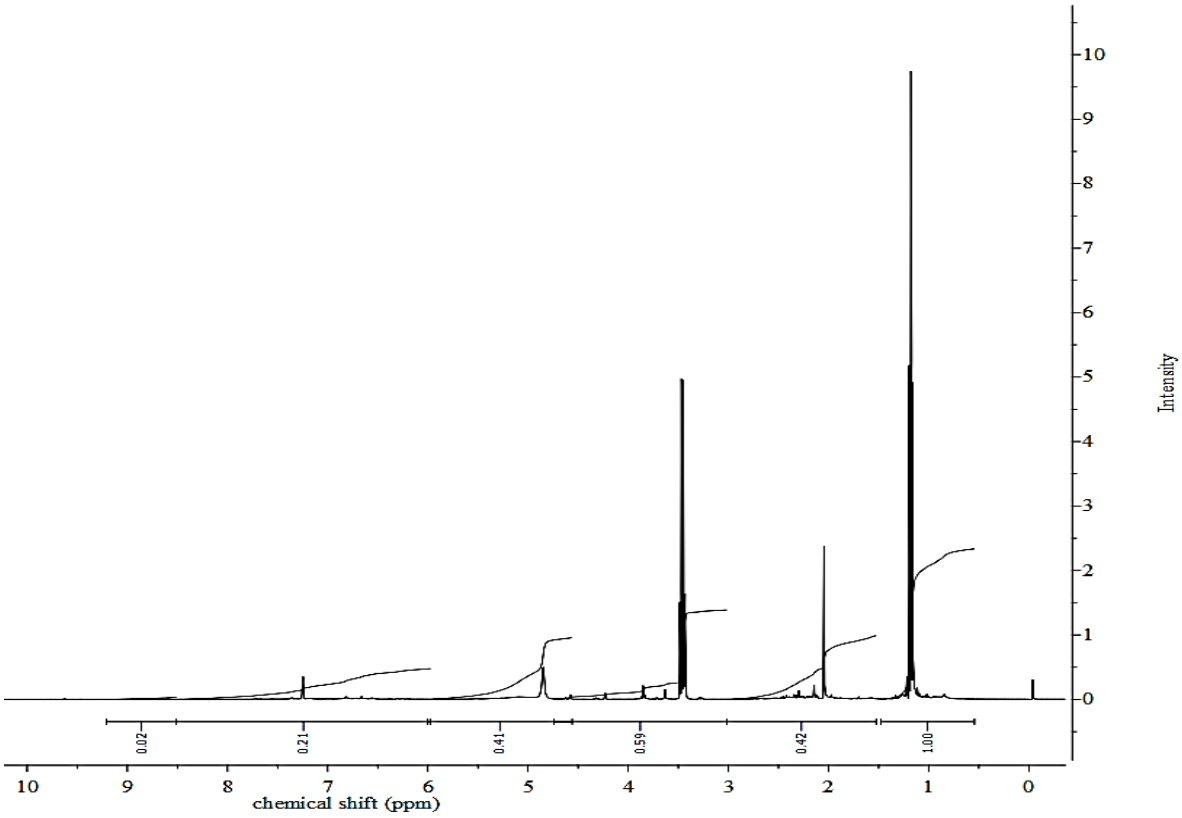

Fig. 4.7: ^{1}H-NMR Spectrum of the Bio-Oil

Bio-oil comprises different organic compounds such as aldehydes, sugars, phenols, and other alcohols, compounds with hydroxyl and ketone functional groups, and organic acids, etc. which show a widespread chemical functionality [8, 35]. Analytical methods including spectroscopic (MS, IR) and chromatographic (HPLC, GC) are unable to do a complete evaluation of bio-oil compounds [18, 36] because of its chemical complexity. To overcome these mentioned drawbacks, NMR spectroscopy was used (**Fig. 4.7**). **Table 4.4** presents integral data pertaining to distinct segments of the ^{1}H-NMR spectra of bio-oil, organized by % H content.

The integrated regions in the spectra are divided according to different chemical shift ranges from 0.5-10.1 ppm as shown in **Table 4.4**. The region within the spectral range of 6.0 to 8.5 ppm is attributed to the protons within the aromatic rings (4.60 %), likely derived from lignin-derived compounds. It also indicates hydrogen atoms' existence in benzenoids and the presence of heteroatom i.e. O and N. Additionally, the integrated region

within the range of 4.4 to 6.0 ppm encompasses the methoxy protons (39.93 %), which are again often associated with lignin-derived compounds. The proton signals within the chemical shift range of 3.0 to 4.4 ppm signify alcohols and aromatic ring-joining methylene groups (13.81 %), indicating the presence of compounds like phenols, alcohols, and other oxygenated compounds. Whereas, the signals between 1.5 - 3.0 ppm indicate CH_3, CH_2, and CH proton in alpha and aromatic ring (34.67 %). Also, the alkane presence (8.37 %) is depicted by the leftmost region, ranging from 0.5 to 1.5 ppm on the chemical shift scale.

Table 4.4: ^{1}H-NMR result of the bio-oil

Chemical Shift Range (ppm)	Assignment	Hydrogen, %
0.5-1.5	Alkanes	8.37
1.5-3.0	Aliphatics -α to heteroatom or unsaturation	34.67
3.0-4.4	Alcohols, methylene- dibenzene	13.81
4.4-6.0	Methoxy, carbohydrates	39.93
6.0-8.5	(Hetero-) aromatics	4.60
9.5-10.1	Aldehydes	1.59

4A.5.4 GC-MS

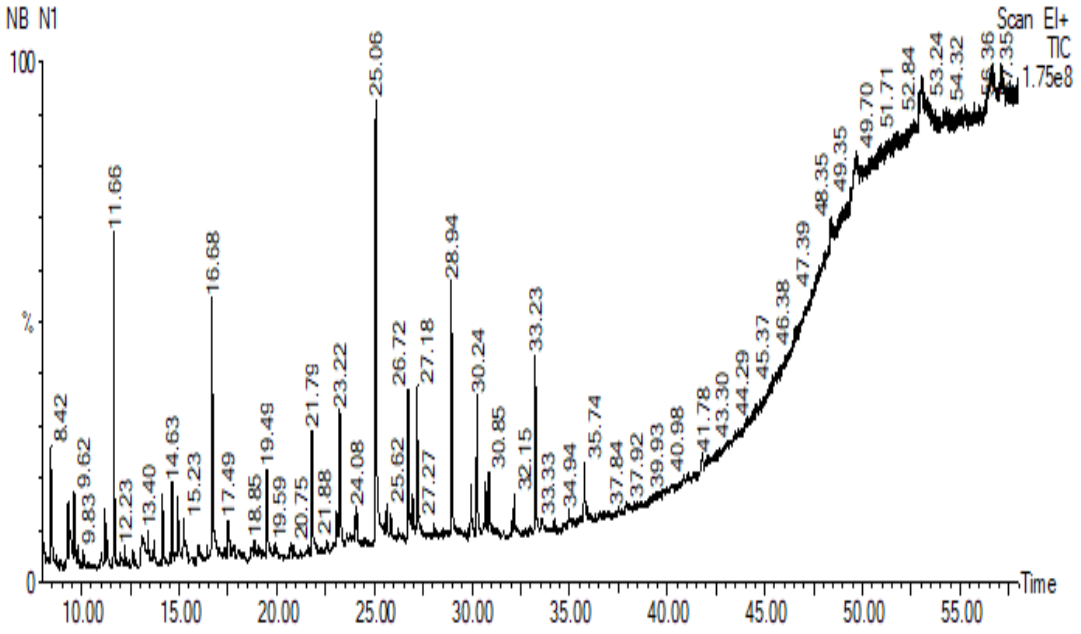

Fig. 4.8: Total ion chromatogram of TD bio-oil

Table 4.5: GC-MS compounds for non-catalytic pyrolysis oil

RT	Compounds name	Molecular formula	Area %
8.419	Butanedioic Acid, Hydroxy-, Dibutyl Ester	$C_{12}H_{22}O_5$	1.606
9.314	Cyclohexene, 1-Isopentyl	$C_{11}H_{20}$	0.501
9.409	3-Furanmethanol	C_5H_6O	0.597
9.619	1H-Pyrazole, 3-Methyl	$C_4H_6N_2$	0.688
11.19	1-Ethylcyclopentene	C_7H_{12}	0.669
11.66	3-Cyclobutene-1,2-Dicarboxylic Acid, Dimethyl Ester	$C_8H_{10}O_4$	3.189
13.105	Benzene, (1,1-Dimethylethoxy)	$C_{10}H_{14}O$	0.704
13.181	Benzene, (2-Methylpropoxy)	$C_{10}H_{14}O$	0.694
14.141	Pentane, 1,1'-Oxybis-	$C_{10}H_{22}O$	0.878
14.916	2-Cyclopenten-1-One, 2-Hydroxy-3-Methyl-	$C_6H_8O_2$	1.076
15.226	Bicyclo[4.1.0]Heptan-2-One	$C_7H_{10}O$	0.928
16.682	Phenol, 2-Methoxy	$C_7H_8O_2$	3.68
17.492	Cyclohexanol, 1-Ethenyl	$C_8H_{14}O$	0.54
19.488	Benzene, 1,2-Dimethoxy-	$C_8H_{10}O_2$	1.171
21.794	Phenol, 4-Ethyl-2-Methoxy	$C_9H_{12}O_2$	1.593
23.055	Bicyclo[3.1.1]Heptan-3-One, 6,6-Dimethyl-2-(2-Methylpr	$C_{13}H_{22}O$	0.805
23.22	Phenol, 2,3,5,6-Tetramethyl-	$C_{10}H_{14}O$	2.046
24.085	Phenol, 2-Methoxy-3-(2-Propenyl)	$C_{10}H_{12}O_2$	0.5
25.055	Phenol, 2,6-Dimethoxy	$C_8H_{10}O_3$	6.563
26.721	Phenol, 2-Methoxy-4-(1-Propenyl)	$C_{10}H_{12}O_2$	1.821
26.946	Phenol, 3,5-Bis(1,1-Dimethylethyl)	$C_{14}H_{22}O$	0.507
27.176	1,2,3-Trimethoxybenzene	$C_9H_{12}O_3$	1.868
28.937	Benzene, 1,2,3-Trimethoxy-5-Methyl-	$C_{10}H_{14}O_3$	3.16
29.932	Benzene, 1,2,3-Trimethoxy-5-Methyl	$C_{10}H_{14}O_3$	0.775
30.242	4-Methyl-2,5-Dimethoxybenzaldehyde	$C_{10}H_{12}O_3$	1.816
30.693	2,4-Dimethoxybenzyl Alcohol	$C_9H_{12}O_3$	0.622
30.858	Benzene, 2-(1,1-Dimethylethyl)-1,4-Dimethoxy-	$C_{12}H_{18}O_2$	0.773
32.158	Benzene, 1,4-Dimethoxy-2,3,5,6-Tetramethyl-	$C_{12}H_{18}O_2$	0.639
33.234	Benzene, 1,4-Dimethoxy-2,3,5,6-Tetramethyl-	$C_{12}H_{18}O_2$	2.314
35.745	Benzene, 1,1'-Butylidenebis	$C_{16}H_{18}$	0.851

Bio-oil is a complex mixture of several hundred organic compounds with a wide range of chemical functions. GC-MS analyses of bio-oil, as shown in Fig. 4.8 were tabulated in Table 4.5. A total of 30 compounds were identified having more than 0.5% of peak area; and it has been observed that bio-oil consisted mainly of phenols, aliphatic hydrocarbons, aromatic hydrocarbons, alcohols, and some acids, etc. The carbon distributions of the identified compounds were found to be in the range of C_4–C_{16}. Phenols present in the bio-oil were more than 16.71%, which were made up of various phenol derivatives such as methoxy phenols and alkylphenols (methyl phenols, methyl-ethyl phenols). Aromatic hydrocarbons in the bio-oil accounted for about 12% of the bio-oil and consisted mainly of several benzene derivatives. Out of these compounds, a few compounds like 4-ethyl-2-methoxyphenol can be used as a flavouring agent. Moreover, 1,2-dimethoxybenzene is used as a building block for the organic synthesis of other aromatic compounds.

4A.6 Characterization of Biochar

4A.6.1 Physico-chemical characterization

Biochar possesses various characteristics that impact its interactions with the environment and the organisms that it comes into contact with. The physicochemical properties of biochar are essential in assessing its possible applications and efficacy in different domains. Proximate analysis includes moisture content, volatile matter, fixed carbon, and ash content of the biochar. These factors are crucial for comprehending its capacity for carbon storage, enhancement of soil fertility, and remediation of pollution. The presence of ash in biochar can influence its pH level and reactivity. The reactivity and calorific value of biochar are greatly influenced by its elemental composition and carbon quantity, which play a crucial role in determining its applicability for many purposes, including energy production. Evaluation of biochar's electrical conductivity (EC) is considered important in terms of its potential application in varied fields ranging from soil amendments to supercapacitor.

Table 4.6 represents the physicochemical compositions of the TD biochar prepared at 400, 500, and 600 °C. Both MC and VM of the biochars were found to be reduced from 4.06±0.05 wt.% to 3.25±0.02 wt.% and 19.41±0.12 wt.% to 10.52±0.11 wt.% with rise in temperature. Lignin availability in biomass partly inhibits the pyrolytic breakdown at 400 °C, which is not seen at higher temperatures, resulting in a high VM of biochars at low

temperature. Furthermore, with the temperature rise the ash content increased which is caused by the higher concentration of minerals, as well as the destructive volatilization of lignocellulosic materials at higher temperatures [37]. The FC content of the biochars increased from 65.08±0.09 wt.% to 72.45±0.12 wt.%. with the rise in temperatures from 400 – 600 °C (**Table 4.6**).

Table 4.6: Variations in biomass and biochar characteristics across different temperatures

	Properties	**Raw biomass**	**Biochar**		
			400 °C	**500 °C**	**600 °C**
Ultimate Analysis	O (wt. %)	51.53	40.95	37.52	31.21
	N (wt. %)	0.93	0.50	0.31	0.16
	H (wt. %)	5.85	2.90	2.48	2.21
	C (wt. %)	42.69	55.65	59.69	66.42
	O/C	-	0.55	0.47	0.35
	H/C	-	0.63	0.50	0.40
Proximate Analysis	VM (wt. %)	70.25±0.36	19.41±0.12	15.78±0.14	10.52±0.11
	MC (wt. %)	6.26±0.21	4.06±0.05	3.62±0.04	3.25±0.02
	AC (wt. %)	7.04±0.09	6.15±0.03	7.54±0.05	8.48±0.08
	FC (wt. %)	16.45±0.39	65.08±0.09	68.05±0.11	72.45±0.12
	Calorific value (MJ/kg)	15.95	18.62	20.10	22.63
	pH		7.25	9.18	10.38
	EC (dS/m)		0.76	1.01	1.24

Oxygen contents in biochar obtained at all the temperatures were found to be lower than the parent feedstock, while the reverse was true for C-contents (**Table 4.6**). Biochars had a CV of 22.63 MJ/kg (at 600 °C), compared to 15.95 MJ/kg for the parent biomass feedstock. The assessment of aromaticity levels, and carbonization, is expressed by the H/C and O/C ratios [38]. In this context, the H/C and O/C ratios decreased as pyrolysis temperature increased, owing to a rise in the aryl C proportion and biochar carbonization [39]. The decomposition of decarbonylation and decarboxylation, accompanied by the

conversion of alkyl-aryl carbon-carbon bonds involves the linkage of compact aromatic rings through cross-linking and is also attributed to O/C ratio reduction [40]. Biochars have a lower H/C ratio, indicating greater aromaticity, which implies higher resistance towards decomposition and thus, becomes recalcitrant. This property of biochar helps it to stay in the soil for longer periods thereby sequestering carbon [1]. The pH of biochars increased from 7.25 to 10.38 as the pyrolysis temperature rose from 400 to 600 °C, likely due to the release of alkali salts from organic matrix and their subsequent accumulation in the biochar. This temperature-dependent increase in pH can also be attributed to the formation of basic inorganic compounds, such as carbonates and oxides, as well as the reduction of acidic functional groups during pyrolysis [2]. As all the resulting biochar was alkaline, demonstrating that the most of acidic groups were lost during the pyrolysis process. The elevated pH levels of biochar can be advantageous for addressing soil acidity concerns and serve as a soil amendment. Biochar has the potential to be utilized as a liming agent in agricultural soils in India's northeastern region because the soils of this region are generally acidic in nature. The electrical conductivity (EC) of biochars also increased as pyrolysis temperature rises signifying higher degree of aromatization, and higher ash content [46].

4A.6.2 FTIR Analysis

The presence of functional groups and the chemical characteristics of biochar can have an impact on its interactions with microbes and other substances. Biochars possessing distinct functional groups and chemical characteristics have the ability to facilitate microbial proliferation, enhance nutrient accessibility, and promote various biological activities.

The FTIR spectra of biochar and biomass exhibit distinct differences due to the thermal decomposition and chemical transformations occurring during pyrolysis. Biomass typically shows strong absorption bands corresponding to hydroxyl (O–H) stretching, cellulose and hemicellulose (C–O, C–H), and lignin-derived aromatic groups. In contrast, biochar spectra reveal a progressive reduction in functional groups as the pyrolysis temperature increases, reflecting the transformation of organic matter into more thermally stable structures.

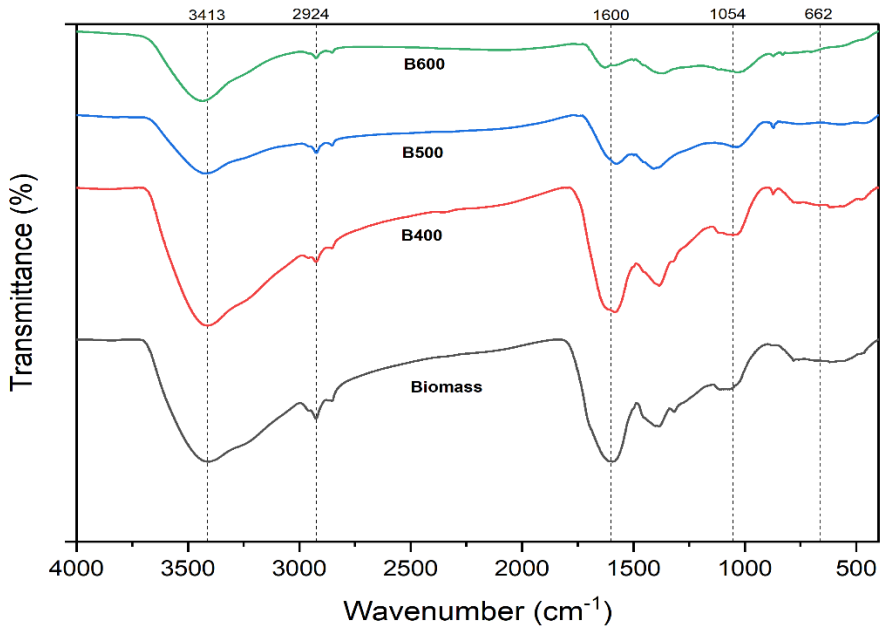

Fig. 4.9: FTIR analysis of biochar at different temperatures

The FTIR spectra of biochars obtained at temperatures between 400 °C and 600 °C (**Fig. 4.9**) indicate that increasing pyrolysis temperature significantly alters functional group composition. For instance, the O–H stretching vibrations (3600–3200 cm^{-1}), attributed to hydroxyl groups and bound water in biomass, decrease due to dehydration and water release during pyrolysis. Similarly, the weak aliphatic C–H stretching bands (2940–2840 cm^{-1}) diminish as temperature rises, reflecting the thermal breakdown of alkyl groups, leading to the release of hydrocarbons like CH_4 and C_2H_4. The absorbance associated with carbonyl (C=O) groups (1850–1650 cm^{-1}) also decreases at higher temperatures, indicating the decarboxylation reactions that release CO and CO_2 gases. Likewise, the intensities of bands corresponding to C=C stretching (1650–1580 cm^{-1}) and C–O stretching (1350–950 cm^{-1}) decline, showing a reduction in oxygenated functional groups and volatile formation with increasing temperature.

At 600 °C, the biochar spectra are dominated by bands indicative of aromatic structures, highlighting the conversion of biomass into a highly aromatic, thermally stable material. This transition reflects the loss of labile and oxygenated groups in the biomass, leaving behind condensed aromatic structures that are characteristic of biochar at elevated temperatures. The differences in FTIR spectra between biomass and biochar, and the temperature-dependent reduction in functional groups, underscore the significant impact of pyrolysis conditions on the chemical properties and reactivity of biochar.

4A.6.3 SEM Analysis

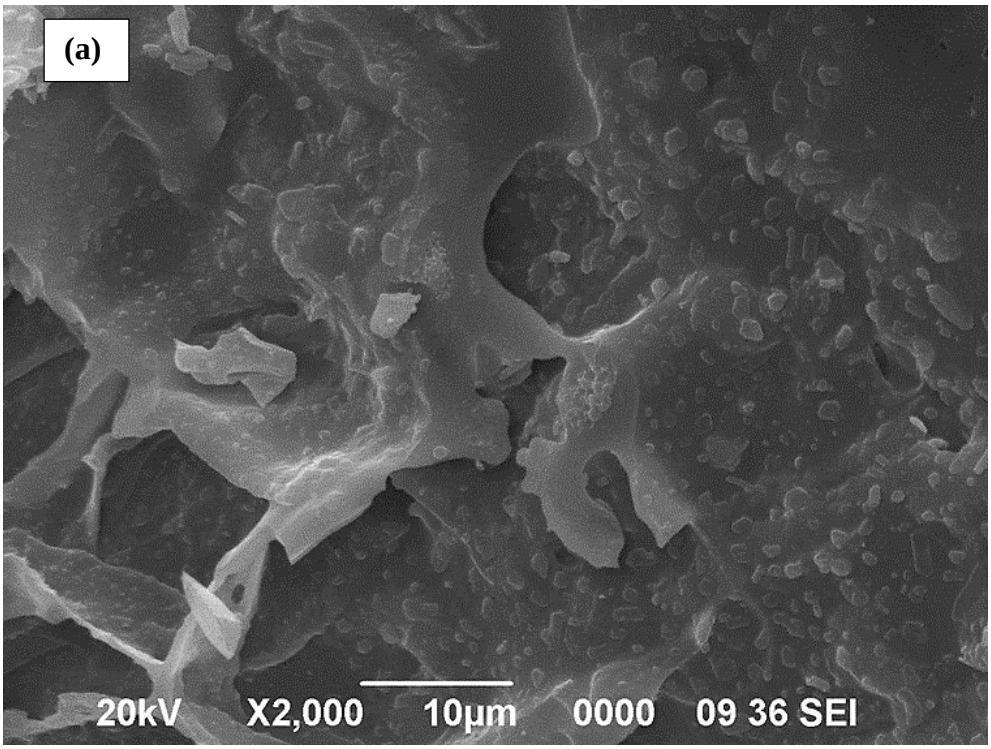

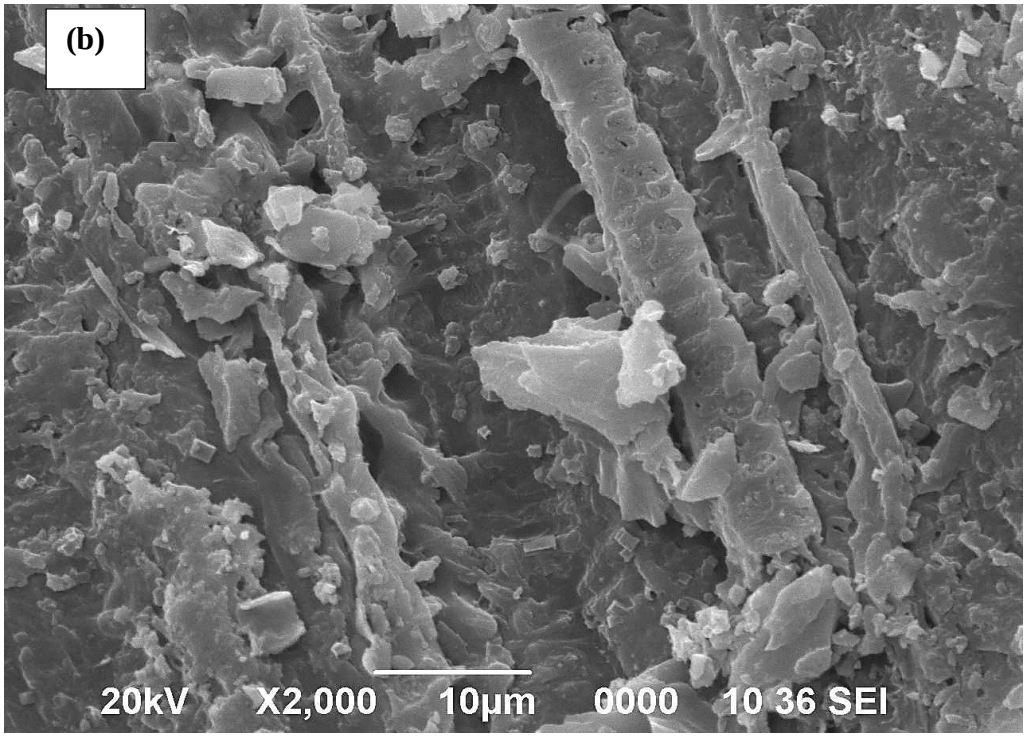

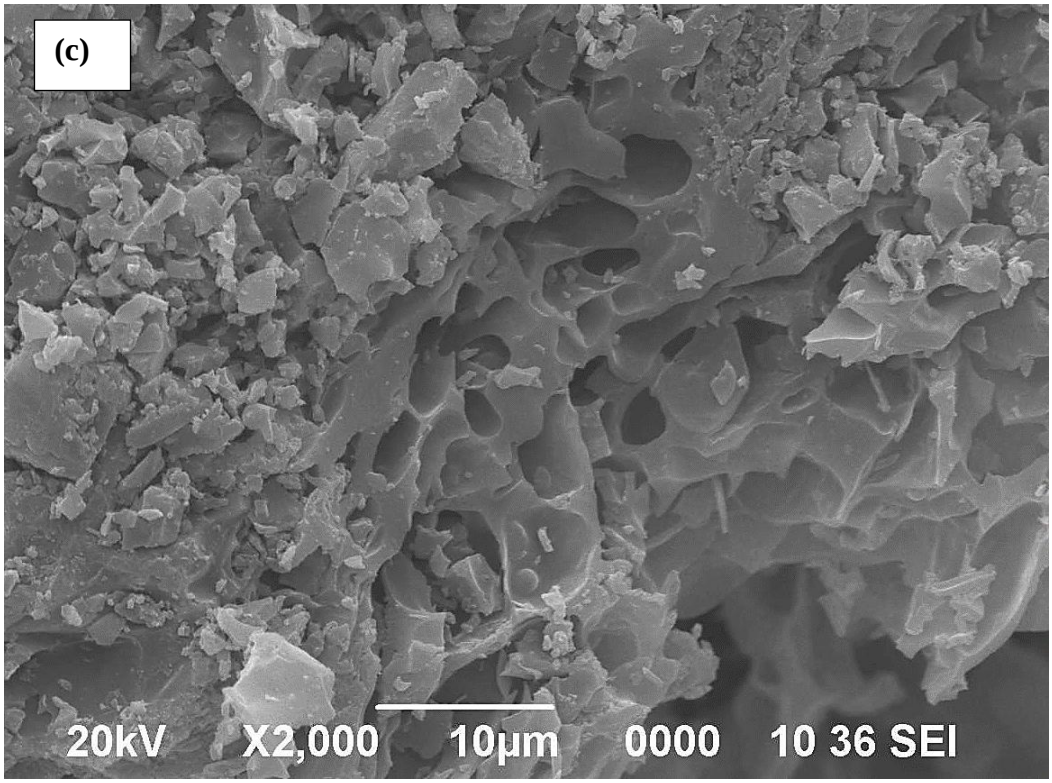

Fig. 4.10: SEM imagery of biochar at (a) 400 °C, (b) 500 °C and (c) 600 °C

The SEM was useful for the evaluation of biochar's surface characteristics. **Fig. 4.10** (a)-(c) show the SEM images depicting the biochars produced under different temperatures, specifically 400 °C, 500 °C and 600 °C, respectively.

The pyrolysis of TD biomass at varying temperatures alters the morphology of the surface in the resulting biochar. As illustrated in **Fig. 4.10**, pyrolysis temperatures significantly impact the biochar's structure. Micrographs reveal the amorphous and heterogeneous nature of the biochars. During the pyrolysis process, increased surface inhomogeneity, along with the formation of additional depressions, channels, and porous structures can be observed on the biochar surface. The porous structures are formed as volatile matter is released, creating pores and cracks [41]. The SEM image of biochar produced at 600 °C shows a knaggy surface with some crater formations. Generally, the surface area of biochar increases with increase in temperatures due to deformation. This suggests that the rate of pore formation exceeds that of pore destruction, with pores enlarging and collapsing at the early stage, and the opposite occurring later in the pyrolysis process [42]. The presence of pores indicates the biochar's potential for soil amendment, as its porosity can facilitate root movement, provide habitats for microorganisms, retain soil nutrients, and enhance water holding capacity [43, 44]. Larger pores allow easier

penetration of water, plant roots, and fungal hyphae into the soil particles. Typically, biochar porosity of less than 30 μm is effective in retaining water [44].

4A.7 Summary

The present study was conducted to examine how various pyrolysis parameters affect the bio-oil derived from *Tithonia diversifolia* along with the pyrolytic valorization of invasive weed for fuels, chemicals, and energy sources. Temperature ranging from of 400-600 ºC was used for performing pyrolysis with different operating conditions. The production of bio-oil was found to increase until temperatures reached 500 °C, after that it began to decline upon further increase in temperature. The best conditions for optimal bio-oil production of yield 30.16±0.09 wt.% were found at 500ºC (temperature), 150 ml/min (nitrogen flow rate), 0.25-0.50 mm (particle size), and 40 ºC/min (heating rate). Furthermore, the bio-oil exhibited a calorific value of 23.84 MJ/kg, which was greater than the biomass feedstock (15.95 MJ/kg), and this enhancement could be attributed to lower oxygen and higher carbon content of bio-oil (31.49 and 57.75 wt.%, respectively) than the original biomass feedstock (51.53 and 41.69 wt.%, respectively). Yield of biochar decreased with increasing final pyrolysis temperature. The biochars were subjected to physico-chemical evaluation to assess their suitability as a fuel source and for various additional uses. The biochar had a higher calorific value than the biomass it came from. The calorific value increased as the pyrolysis temperature increased. The H/C and O/C ratios of the biochar suggest that charring leads to an increase in aromaticity. This outcome suggests that the produced biochar is suitable for use as a source of energy and also may be useful for applications such as soil amendment and adsorbent for various impurities.

References

1. Ok, Y.S., Uchimiya, S.M., Chang, S.X., Bolan, N. (Eds.). Biochar: Production, Characterization, and Applications. *CRC Press*, 2015.
2. Yuan, J.H., Xu, R.K., and Zhang, H. The forms of alkalis in the biochar produced from crop residues at different temperatures. *Bioresource Technology*, 102(3):3488-3497, 2011.
3. Chukwuka, K.S., Ogunyemi, S., Osho, J.S.A., Atiri, G.I., and Muoghalu, J.I., Eco-physiological responses of *Tithonia diversifolia* (Hemsl.) A. Gray in nursery and field conditions, *Journal of Biological Sciences,* 7(5): 771-775, 2007.
4. Muoghalu, J.I. Growth, reproduction and resource allocation of *Tithonia diversifolia* and *Tithonia rotundifolia*, *Weed Research,* 48(2): 157-162, 2008.
5. Oluwafemi, and A.B., Olumide, A.T. Study on the effects of fresh shoot biomass of *Tithonia diversifolia* on the germination, growth and yield of cowpea (*Vigna unguiculata L.*). *Journal of Experimental Agriculture International*. 3(4): 1005-1011, 2013.
6. Rojas-Sandoval, J., *Tithonia diversifolia* (Mexican sunflower), Cabi compendium, Retrieved on 15/09/2018. https://www.cabidigitallibrary.org/doi/10.1079/cabicompendium.54020.
7. Bhattacharjee, N., and Biswas, A. B. Pyrolysis of *Ageratum conyzoides* (goat weed) Parametric influence on the product yield and product characterization. *Journal of Thermal Analysis and Calorimetry,* 139(2), 1515-1536, 2020.
8. Saikia, P., Gupta, U. N., Barman, R. S., Kataki, R., Chutia, R. S., and Baruah, B. P., Production and characterization of bio-oil produced from *Ipomoea carnea* bio-weed. *BioEnergy Research*, 8, 1212-1223, 2015.
9. Ramesh, N., and Murugavelh, S. (2020). A cleaner process for conversion of invasive weed (*Prosopis juliflora*) into energy-dense fuel: kinetics, energy, and exergy analysis of pyrolysis process. *Biomass Conversion and Biorefinery*, 12: 3067–3080, 2022.
10. Vuppaladadiyam, A.K., Zhao, M., Memon, M.Z., and Soomro, A.F. Microalgae as a renewable fuel resource: a comparative study on the thermogravimetric and kinetic behavior of four microalgae. *Sustainable Energy Fuels,* 3(5): 1283-1296, 2019.

11. Gogoi, M., Konwar, K., Bhuyan, N., Borah, R.C., Kalita, A.C., Nath, H.P., and Saikia, N. Assessments of pyrolysis kinetics and mechanisms of biomass residues using thermogravimetry. *Bioresource Technology Reports*, 4: 40-49, 2018.
12. Saikia, R., Chutia, R.S., Kataki, R., and Pant, K.K. Perennial grass (*Arundo donax L.*) as a feedstock for thermo-chemical conversion to energy and materials. *Bioresource technology*, 188:265-272, 2015.
13. Reza, M.S., Ahmed, A., Caesarendra, W., Abu, Bakar, M.S., Shams, S., Saidur, R., and Azad, A.K. *Acacia holosericea*: an invasive species for bio-char, bio-oil, and biogas production. *Bioengineering*, 6(2):33, 2019.
14. Tanger, P., Field, J. L., Jahn, C. E., DeFoort, M. W., and Leach, J. E., Biomass for thermochemical conversion: targets and challenges. *Frontiers in plant science*, 4, 218, 2013.
15. Alves, J. L. F., da Silva, J. C. G., Mumbach, G. D., Domenico, M. D., de Sena, R. F., Machado, R. A. F., and Marangoni, C., Demonstrating the suitability of tamarind residues to bioenergy exploitation via combustion through physicochemical properties, performance indexes, and emission characteristics. *BioEnergy Research*, 13, 1308-1320, 2020.
16. Alves, J. L. F., da Silva, J. C. G., Mumbach, G. D., Di Domenico, M., da Silva Filho, V. F., de Sena, R. F., ... and Marangoni, C., Insights into the bioenergy potential of jackfruit wastes considering their physicochemical properties, bioenergy indicators, combustion behaviors, and emission characteristics. *Renewable Energy*, 155, 1328-1338, 2020.
17. Deb, U., Bhuyan, N., Bhattacharya, S. S., and Kataki, R. Characterization of agro-waste and weed biomass to assess their potential for bioenergy production. *International Journal of Renewable Energy Development*, 8(3), 2019.
18. Chutia, R. S., Kataki, R., and Bhaskar, T., Characterization of liquid and solid product from pyrolysis of *Pongamia glabra* deoiled cake. *Bioresource technology*, 165, 336-342, 2014.
19. Sut, D., Chutia, R.S., Bordoloi, N., Narzari, R., and Kataki, R., Complete utilization of non-edible oil seeds of *Cascabela thevetia* through a cascade of approaches for biofuel and by-products. *Bioresource technology*, 213: 111-120, 2016.
20. Onay, O., Influence of pyrolysis temperature and heating rate on the production of bio-oil and char from safflower seed by pyrolysis, using a well-swept fixed bed reactor. *Fuel Processing Technology*. 88(5):523-531, 2007.

21. Haykiri-Acma, H., Yaman, S., and Kucukbayrak, S. Effect of heating rate on the pyrolysis yields of rapeseed. *Renewable Energy*, 31(6), 803-810, 2006.
22. Mishra, R. K., Kumar, V., and Mohanty, K., Pyrolysis kinetics behaviour and thermal pyrolysis of *Samanea saman* seeds towards the production of renewable fuel. *Journal of the Energy Institute*, 93(3), 1148-1162, 2020.
23. Azduwin, K., Ridzuan, M.J.M., Hafis, S.M., and Amran, T., Slow pyrolysis of *Imperata cylindrica* in a fixed bed reactor. *International Journal of Biological, Ecological and Environmental Sciences (IJBEES)*, 1(5), 176-180, 2012.
24. Uddin, M. S., Joardder, M. U. H., and Islam, M. N., Design and construction of fixed bed pyrolysis system and plum seed pyrolysis for bio-oil production. *International Journal of Advanced Renewable Energy Research*, 7(1): 405-409, 2012.
25. Park, H. J., Dong, J. I., Jeon, J. K., Park, Y. K., Yoo, K. S., Kim, S. S., ... and Kim, S., Effects of the operating parameters on the production of bio-oil in the fast pyrolysis of Japanese larch. *Chemical Engineering Journal*, 143(1-3), 124-132, 2008.
26. Wauton, I., and Ogbeide, S. E., Investigation of the production of pyrolytic bio-oil from water hyacinth (*Eichhornia crassipes*) in a fixed bed reactor using pyrolysis process. *Biofuels*, 13(2), 189-195, 2022.
27. Onay, O., and Koçkar, O. M. Fixed-bed pyrolysis of rapeseed (*Brassica napus L.*). *Biomass and Bioenergy*, 26(3), 289-299, 2004.
28. Choudhury, N. D., Chutia, R. S., Bhaskar, T., and Kataki, R., Pyrolysis of jute dust: effect of reaction parameters and analysis of products. *Journal of Material Cycles and Waste Management*, 16, 449-459, 2014.
29. Bridgwater, A. V., and Peacocke, G. V. C., Fast pyrolysis processes for biomass. *Renewable and sustainable energy reviews*, 4(1), 1-73, 2000.
30. Bordoloi, N., Narzari, R., Chutia, R. S., Bhaskar, T., and Kataki, R., Pyrolysis of *Mesua ferrea* and *Pongamia glabra* seed cover: characterization of bio-oil and its sub-fractions. *Bioresource Technology*, 178, 83-89, 2015.
31. Wongkhorsub, C., and Chindaprasert, N., A comparison of the use of pyrolysis oils in diesel engine. *Energy and Power Engineering*, 5(04), 350, 2013.
32. Lu, Q., Yang, X. L., and Zhu, X. F., Analysis on chemical and physical properties of bio-oil pyrolyzed from rice husk. *Journal of Analytical and Applied Pyrolysis*, *82*(2), 191-198, 2008.

33. Demiral, I., Atilgan, N. G., and Şensöz, S., Production of biofuel from soft shell of pistachio (Pistacia vera L.). *Chemical Engineering Communications*, *196*(1-2), 104-115, 2008.
34. Das, P., Sreelatha, T., and Ganesh, A., Bio oil from pyrolysis of cashew nut shell-characterisation and related properties. *Biomass and bioenergy*, *27*(3), 265-275, 2004.
35. Demiral, İ., Eryazıcı, A., and Şensöz, S., Bio-oil production from pyrolysis of corncob (Zea mays L.). *Biomass and Bioenergy*, *36*, 43-49, 2012.
36. Zou, S., Wu, Y., Yang, M., Li, C., and Tong, J., Thermochemical catalytic liquefaction of the marine microalgae *Dunaliella tertiolecta* and characterization of bio-oils. *Energy & Fuels*, *23*(7), 3753-3758, 2009.
37. Rafiq, M. K., Bachmann, R. T., Rafiq, M. T., Shang, Z., Joseph, S., and Long, R., Influence of pyrolysis temperature on physico-chemical properties of corn stover (Zea mays L.) biochar and feasibility for carbon capture and energy balance. *PloS one*, *11*(6), e0156894, 2016.
38. Baldock, J. A., and Smernik, R. J., Chemical composition and bioavailability of thermally altered Pinus resinosa (Red pine) wood. *Organic Geochemistry*, *33*(9), 1093-1109, 2002.
39. Fu, P., Yi, W., Bai, X., Li, Z., Hu, S., and Xiang, J., Effect of temperature on gas composition and char structural features of pyrolyzed agricultural residues. *Bioresource Technology*, *102*(17), 8211-8219, 2011.
40. Yuan, H., Lu, T., Zhao, D., Huang, H., Noriyuki, K., and Chen, Y., Influence of temperature on product distribution and biochar properties by municipal sludge pyrolysis. *Journal of Material Cycles and Waste Management*, *15*, 357-361, 2013.
41. Zhang, J., Huang, B., Chen, L., Li, Y., Li, W., and Luo, Z., Characteristics of biochar produced from yak manure at different pyrolysis temperatures and its effects on the yield and growth of highland barley. *Chemical Speciation & Bioavailability*, *30*(1), 57-67, 2018.
42. Liu, W. J., Jiang, H., and Yu, H. Q. Development of biochar-based functional materials: toward a sustainable platform carbon material. *Chemical reviews*, *115*(22), 12251-12285, 2015.
43. Xiao, X., Chen, B., Chen, Z., Zhu, L., and Schnoor, J. L. Insight into multiple and multilevel structures of biochars and their potential environmental applications: a critical review. *Environmental science & technology*, *52*(9), 5027-5047, 2018.

44. Lehmann, J., and Joseph, S., Biochar for environmental management: an Introduction. In: Lehmann, J., Joseph, S. (Eds.), *Biochar for environmental management: science, technology and implementation*. pp. 1–14 London, U.K. Routledge, 2015.
45. Putun, A.E., Apaydin, E., and Putun, E. Rice straw as a bio-oil source via pyrolysis and steam pyrolysis. *Energy*, 29 (12-15), 2171-2180, 2004.
46. Gabhi, R., Basile, L., Kirk, D. W., Giorcelli, M., Tagliaferro, A., and Jia, C. Q. Electrical conductivity of wood biochar monoliths and its dependence on pyrolysis temperature. Biochar, 2, 369-378, 2020.
47. Sasmal, S., Goud, V.V. and Mohanty K., Characterization of biomasses available in the region of North-East India for production of biofuels, Biomass & Bioenergy, 45, 212−220, 2012.
48. Nanda, S., Mohanty, P., Pant, K. K., Naik, S., Kozinski, J. A., and Dalai, A. K. Characterization of North American lignocellulosic biomass and biochars in terms of their candidacy for alternate renewable fuels. Bioenergy Research, 6, 663-677, 2013.
49. Choudhury, N. D., Bhuyan, N., Bordoloi, N., Saikia, N., and Kataki, R., Production of bio-oil from coir pith via pyrolysis: kinetics, thermodynamics, and optimization using response surface methodology. *Biomass Conversion and Biorefinery*, *11*, 2881-2898, 2021.
50. Shah, Z., Cataluña Veses, R., and Silva, R. D., GC-MS and FTIR analysis of bio-oil obtained from freshwater algae (spirogyra) collected from Freshwater. *International Journal of Environmental & Agriculture Research (IJOEAR). Bikaner. Vol. 2, no. 2 (Feb. 2016), p. 134-141*, 2016.

Chapter 4B

Comparative Assessment of Artificial Neural Network (ANN) and Response Surface Methodology (RSM) for Evaluation of the Predictive Capability on Bio-Oil Yield

4.B.1 Introduction

Pyrolytic conversion of biomass into fuel is considered one of the most sustainable and economical conversion processes [2, 3]. The liquid product obtained from pyrolysis may be used as a fuel or feedstock for many commodity chemicals. Pyrolysis depends on various factors viz., temperature, heating rate, particle size, residence time, and the method of condensation of vapors [5]. Most of the available literature deals with the understanding of the influence of specific parameters on the feedstock and its product yield while the other process parameters are kept constant. Although this approach provides in-depth information about the mechanism involved but requires multiple number of experiments to arrive at the conclusion and lacks integration of the interaction effect between the process parameters. In view of the above, the classical approach as applied in the previous chapter may not be suitable for all purposes. In addition to that, the classical way is a time-consuming as well as, an expensive approach towards attaining optimum conditions. Hence to overcome these limitations, mathematical modeling is considered an important tool to gather knowledge on the significance of the factors affecting the pyrolysis process performance. Generally, response surface methodology (RSM) and artificial neural network (ANN) are being used which enables the modelling and optimization of all the process parameters together [5]. Although these methods also suffer from some inherent disadvantages, but both of these have several advantages and are widely used [1, 4, 8]. However, there is a lack of established information on the comparative performance assessment of fixed bed-pyrolysis systems on bio-oil yield using RSM and ANN. Therefore, to bridge the knowledge gap on the comparative analysis of both models, the current investigation aims to evaluate the efficacy of both models for the prediction of bio-oil yield from a biomass sample taking several variables.

In the current study, four factors five levels central composite design (CCD) has been employed for RSM; and a multilayer perceptron (MLP) neural network consisting of 4 neurons in input, 14 neurons in hidden, and 1 neuron in output layer models has been employed. These models were used to predict the experimental variables like temperature, inert gas flow rate, rate of heating, and size of biomass particles on pyrolysis oil yield from biomass. The results obtained from both models were compared based on the coefficient of determination (R^2), mean average error (MAE), root mean square error (RMSE), standard error of prediction (SEP), and absolute average deviation (AAD).

4B.2 Experimental Design and Statistical Analysis by RSM

RSM was carried out to achieve a realistic model between the investigated factors with experimental response i.e., the yield of pyrolysis oil. A total of 30 experimental runs were conducted, utilizing various variables as prescribed by the Design Expert software, which is detailed in Chapter 3. The outcomes of these runs are presented in **Table 4.7**.

Table 4.7: Experimental and predicted bio-oil yield as per the CCD experimental design matrix

Expt No.	Experimental Bio-oil yield (%)	Predicted Bio-oil yield (%)	
		RSM	ANN
1	22.13	22.18	22.10
2	15.71	15.23	15.71
3	25.41	25.35	25.41
4	29.54	30.29	30.38
5	28.18	28.26	28.08
6	27.27	26.73	27.26
7	20.08	19.47	19.99
8	23.89	23.86	23.89
9	30.84	30.29	30.37
10	27.23	27.95	27.23
11	26.92	26.21	26.92
12	24.55	24.71	24.55
13	23.47	24.35	23.47
14	22.48	23.5	22.48
15	30.16	30.29	30.37
16	23.65	23.89	23.65
17	22.74	22.51	22.55
18	30.93	30.29	30.37
19	26.47	25.72	26.47
20	28.65	28.18	28.65
21	24.33	24.68	24.82
22	24.57	24.43	24.13
23	28.08	27.12	28.08

24	25.18	26.03	25.18
25	31.02	30.39	31.02
26	29.31	28.75	29.19
27	29.65	30.29	30.37
28	26.93	27.54	26.93
29	24.71	25.9	24.71
30	30.61	30.29	30.37

A polynomial equation of second-order defines the overall relationship between independent variables, which can be presented by Eq. (1) and Eq. (2) in coded and actual factors, respectively.

$$Bio-oil = +30.29 + 1.06 \times A + 0.80 \times B - 0.67 \times C - 0.51 \times D - 0.069 \times AB - 0.22 \times AC - 0.25 \times AD - 0.26 \times BC + 0.63 \times BD + 0.033 \times CD - 3.23 \times A^2 - 0.12 \times B^2 - 1.13 \times C^2 - 0.64 \times D^2 \quad (1)$$

$$Bio-oil = -159.10625 + 0.63944 \times T + 0.091292 \times HR + 0.16591 \times FR + 12.22833 \times PS - 9.25000E^{-005} \times T \times HR - 5.85000E^{-005} \times T \times FR - 0.013233 \times T \times PS - 5.11250E^{-004} \times HR \times FR + 0.25225 \times HR \times PS + 2.65000\,E^{-003} \times FR \times PS - 5.75093\,E^{-004} \times T^2 - 1.24896\,E^{-003} \times HR^2 - 4.50958E^{-004} \times FR^2 - 10.17833 \times PS^2 \quad (2)$$

The statistical model was tested using F-tests, and the result from ANOVA has been summarized in **Table 4.8.**

From the results obtained it was observed that both regression and model are statistically significant with p<0.05 and F-value=37.26. The probability of occurrence of such a large Model F-value due to noise is 0.01. "Prob>F'' values suggest that the terms of the model are statistically significant. Also, it has been observed that A, B, C, D, BD, A^2, C^2, and D^2 are significant model terms, and among all the individual parameters temperature is the most significant term, followed by HR, FR, and PS. "Lack of Fit" is not significant with an F-value of 2.48 which indicates the fitness of the model. There is a 16.41% chance that noise could be a possible reason for such a large value for the "Lack of Fit F-value". The R^2 for the model was 0.9720. Moreover, the predicted R^2 is in reasonable agreement with the adjusted R^2. Adeq Precision was found as 27.009, which indicates the signal-to-noise ratio and its value of more than 4 is desirable.

Table 4.8: ANOVA for Response Surface Quadratic model

Sources	**Sum of squares**	**df**	**Mean square**	**F-value**	**P-value Prob>F**	
Model	373.60	14	26.69	37.26	< 0.0001	significant
A- T	26.90	1	26.90	37.56	< 0.0001	
B-HR	15.47	1	15.47	21.60	0.0003	
C-FR	10.84	1	10.84	15.13	0.0014	
D-PS	6.13	1	6.13	8.56	0.0104	
AB	0.077	1	0.077	0.11	0.7475	
AC	0.77	1	0.77	1.08	0.3162	
AD	0.99	1	0.99	1.38	0.2592	
BC	1.05	1	1.05	1.46	0.2457	
BD	6.36	1	6.36	8.88	0.0093	
A^2	287.03	1	287.03	400.72	< 0.0001	
B^2	0.43	1	0.43	0.60	0.4516	
C^2	34.86	1	34.86	48.67	< 0.0001	
D^2	11.10	1	11.10	15.50	0.0013	
Residual	10.74	15	0.72			
Lack of Fit	8.94	10	0.89	2.48	0.1641	not significant
Pure Error	1.80	5	0.36			
Cor Total	384.34	29				

R^2= 0.9720, Adjusted R^2= 0.9460, Pred R^2= 0.8593, Std. Dev.= 0.85, C.V.= 3.23 %

4B.2.1 Response Plots

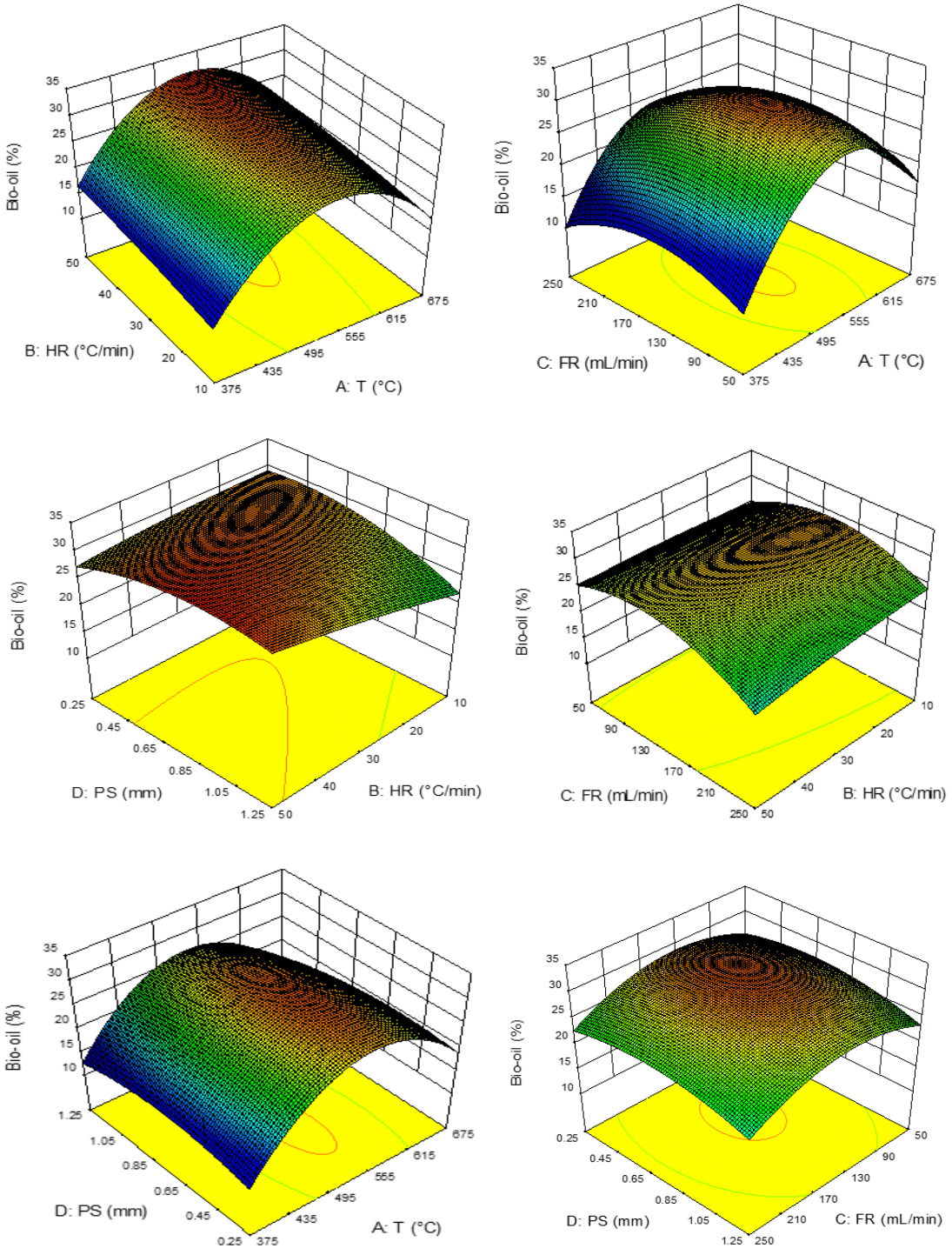

Fig. 4.11 3D-response surface plots showing the effects of different parameters on bio-oil yield (%) (A: T, Temperature (°C); B: HR, Heating rate (°C/min); C: FR, Nitrogen flow rate; D: PS: Particle size (mm))

The three-dimensional response surface plots vs. two variables at a time are presented in **Fig. 4.11**. The plots are very useful in providing valuable information about the simultaneous effect of independent parameters on the production of bio-oil in the

experimental temperature range of 375–675 ºC, N_2 flow rate of 50-250 mL/min, heating rate of 10–50 ºC/min, and particle size of 0.25-1.25 mm. From **Fig. 4.11**, it has been observed that with the increase in temperature, there has been an increase in bio-oil yield which declined beyond 525 °C. The disintegration of organic compounds into non-condensable smaller compounds due to high temperature may be held accountable for the decline [9]. However, with the increasing heating rate increase in the bio-oil yield was observed which may be due to the depolymerisation of biomass at a higher heating rate [4]. It can be observed that an increase in the nitrogen flow rate from 50 to 150 mL/min results in an increase in the bio-oil yield, however, a further increase in the flow rate has a negative impact on bio-oil yield. One of the possible reasons for such an outcome could be the escape of uncondensed volatiles with non-condensable gas from the reactor due to the increased flow rate. Again, when the particle size falls within the range of 0.25 mm to approximately 0.75 mm, a higher yield of bio-oil is obtained. However, beyond this range, the yield begins to decrease. This was related to the heating rate of particles, where the larger particles were heated more slowly than the smaller ones resulting in less volatile material release, which results in lower yields [10].

4B.2.1.1 Optimization and validation of model

The optimal condition values for the designated parameters were obtained by using Design expert tools to solve the regression equation. There were 15 solutions with a desirability of 0.953, found based on the provided experimental conditions. As predicted by the software, the optimal condition for bio-oil yield was a temperature of 536.74 °C, flow rate of 129.55 mL/min, heating rate of 40 °C/min, and particle size in the range of 0.5 to 0.85 mm to produce 31.65 % bio-oil. However, due to apparatus limitation, some correction has been done with some parameters such as temperature has been set as 537 °C and a flow rate of 130 mL/min has been maintained. Triplicate experiments were performed at above condition and an average yield of 31.33 ± 0.19 % of bio-oil has been recovered, which was very much similar to the predicted value.

4B.2.2 Prediction of Bio-Oil Yield by ANN

ANN has proved to be a more effective modeling and simulation method in different fields over the past two decades to predict the behaviour of a non-linear multivariate system [11]. Generally, ANN requires larger sets of experiments to construct an acceptable model

than the RSM. However, even with relatively small data, ANN can also work well if the data are statistically significant in the input and output domains, as is the case with the design of experiments (DOE). Thus, the experimental data obtained through RSM could be sufficient to construct effective ANN models [6, 11].

In this study, the LM back-propagation algorithm was employed using two hidden layers with varying the number of neurons from 1 to 16 through training of the feedforward network. Weight parameters were continuously iterated to achieve the best possible fit model and the best values were achieved after several performances of the iteration. Here, the performances of network topologies or the optimum neurons in the hidden layer were selected based on MSE values and correlation coefficient values (**Fig. 4.12**). A correlation value of 1 means a perfect relationship among the factors while, a value equating to 0 implies absence of a linear relationship. Low MSE, on the other hand, prefers the best possible model.

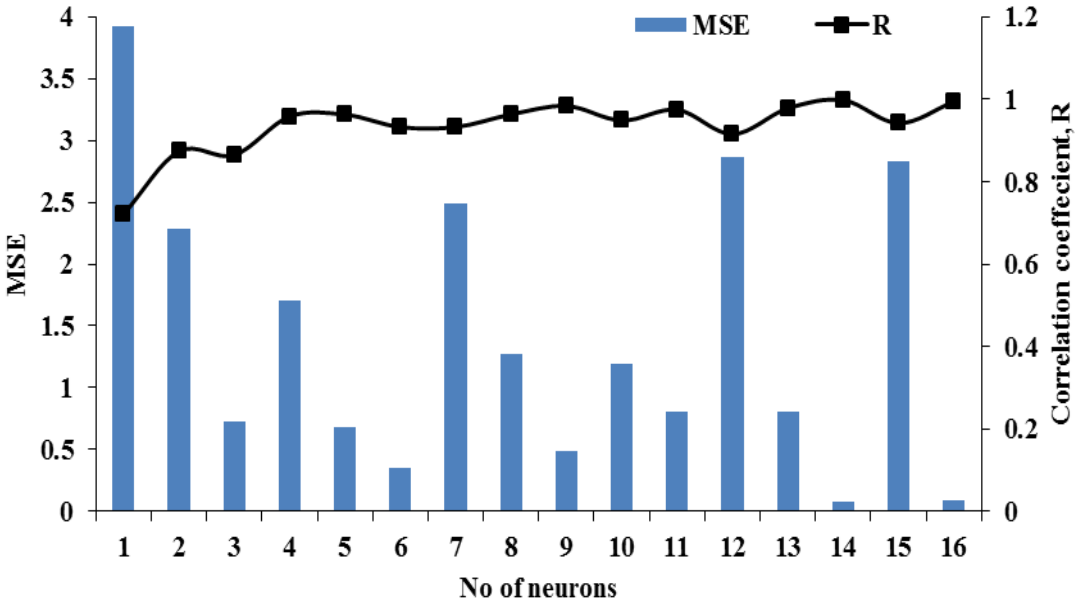

Fig. 4.12. Evaluation of the optimal number of neurons depending on the selected algorithms.

From **Fig. 4.12,** it has been observed that the best neural network topology was 4-14-1. The regression coefficient values for training, testing, validation, and all were 0.9977, 0.9980, 0.9993, and 0.9976, respectively as shown in **Fig. 4.13 (a-d).**

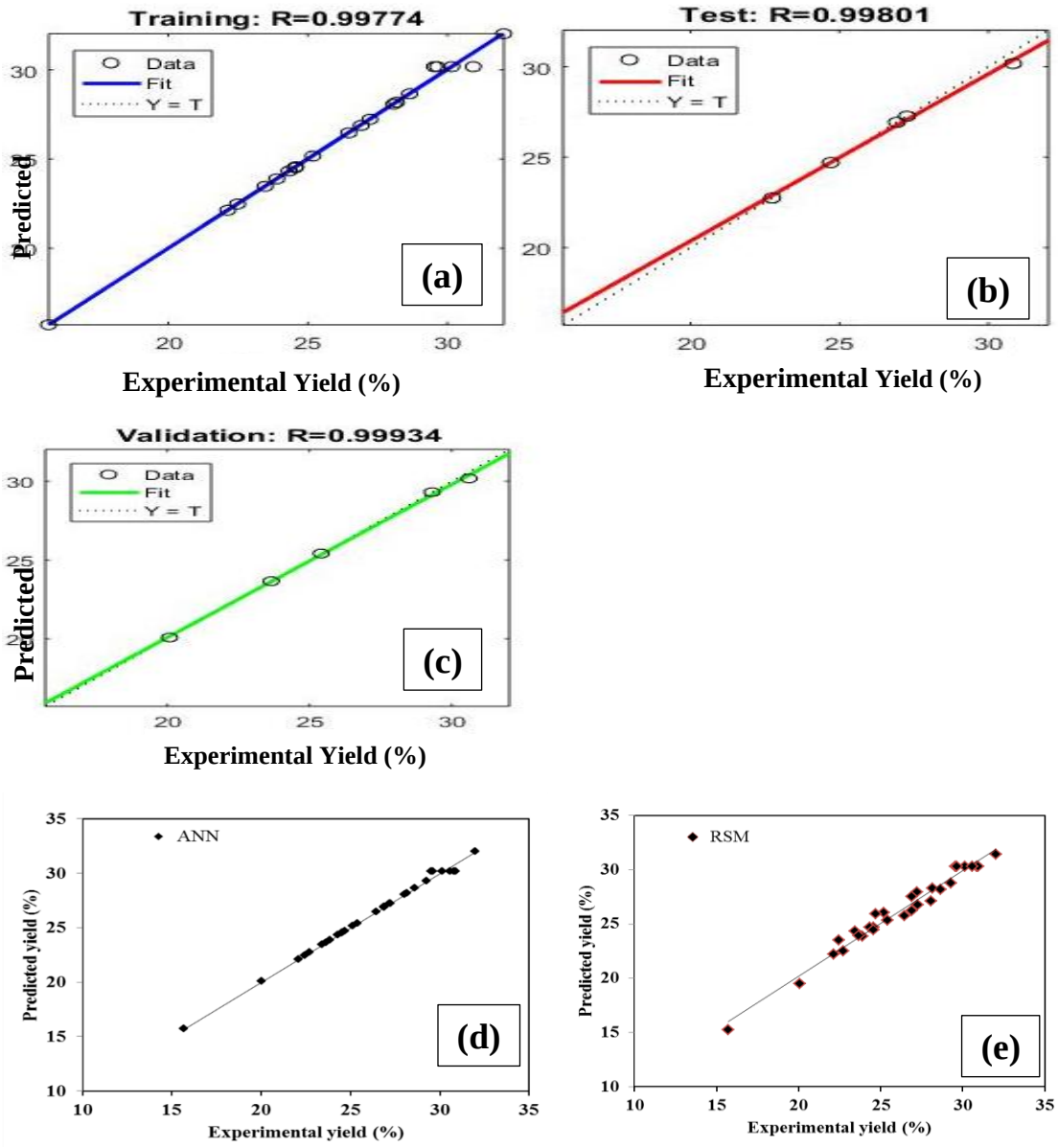

Fig. 4.13 (a) Training, (b) Test, (c) Validation, and (d) the best fit for all expected data sets for the ANN model and (e) all expected data sets for the RSM model

4B.3 Comparative Evaluation of RSM and ANN Models

The predictive capabilities of the RSM and ANN models were evaluated and measured according to certain statistical parameters: R^2, SEP, RMSE, AAD, and MAE, and the results are shown in **Table 4.9**. With an RMSE value of 0.5987; RSM showed more deviation compared to ANN prediction RMSE value of 0.2503. For RSM and ANN, R^2 values were found as 0.9712 and 0.9950 respectively, while the AAD values were found to be 1.98% and 0.53%. SEP, MAE, and AAD were used to check the significance and accuracy of the models [8]. The higher precision of the ANN model over the RSM model

was judged based on the higher value for R^2 and lower values for other statistical parameters obtained for both models.

Table 4.9: Comparison of RSM and ANN models using statistical parameters for design data

	RSM	**ANN**
R^2	0.9712	0.9950
RMSE	0.5987	0.2503
SEP	0.02286	0.0096
MAE	0.5117	0.1052
AAD	1.98%	0.53%

The following figure represents the values of both experimental and predicted bio-oil yield in each experimental run for the bio-oil yield and from the results; it was observed that both models were fitted well to experimental data. However, from **Fig. 4.13 (d) & (e)**, all the predicted values of the ANN model were observed close to the straight line relative to that of the RSM model, indicating the superior predictability of the ANN model.

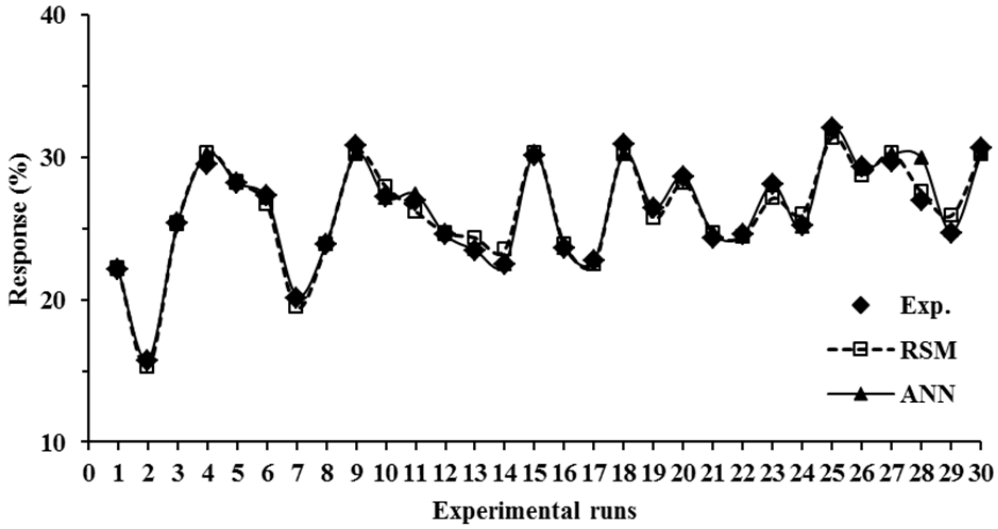

Fig. 4.14 Comparison of ANN and RSM predictive capabilities per experimental run.

The generalization capability can be best judged only with an unseen data set. Hence, the prediction capabilities of developed models were also tested for some additional data (**Table 4.10**). Some statistical parameters were again evaluated from these additional data for both the models and it was observed that the ANN model shows a higher R^2 value and lower RMSE and AAD value compared to the RSM model. Although RSM has the

benefit of having a predictive regression equation, showing and distinguishing insignificant major factors and interaction variables or insignificant quadratic terms in the model and thus the complexity of the problems can be reduced compared to ANN; higher accuracy in prediction of ANN model indicates its universal ability to approximate the nonlinearity of the system, whereas RSM is only restricted to second-order polynomials.

Table 4.10: Validation of RSM and ANN model for additional experimental data

Sl No.	Temp (°C)	HR (°C/min)	FR (ml/min)	PS (mm)	Bio-oil yield (%)		
					Experiment.	Predicted	
						RSM	ANN
1	400	10	100	>1	17.22	13.85	19.77
2	450	20	200	<0.25	20.05	22.84	17.73
3	500	30	150	0.25-0.5	30.30	29.36	30.37
4	500	10	200	<0.25	25.01	26.97	24.96
5	550	40	100	0.25-0.5	30.32	29.43	30.41
6	600	10	50	<0.25	27.01	24.01	27.30
					R^2	0.816	0.9099
					RMSE	1.05	0.63
					AAD	1.85%	0.93%

4B.4 Relative Importance of Parameters on Bio-Oil Yield

The Garson equation as shown in eq. (10) was used to evaluate the influence of input parameters on the output predictions, in which all the connection weights were used [7]

$$I_i = \frac{\sum_{j=1}^{j=n}\left(\left(\frac{|IW_{j,i}|}{\sum_{i=1}^{i=4}|IW_{j,i}|}\right).|LW_{j,i}|\right)}{\sum_{i=1}^{i=4}\{\sum_{j=1}^{j=n}((\frac{|IW_{j,i}|}{\sum_{i=1}^{i=4}|IW_{j,i}|}).|LW_{j,i}|)\}} \qquad (10)$$

Where i is the input variables, I_i is the relative influence of each input variable (T, HR, PS, and FR), j is the hidden layer neurons, n is the number of neurons, $IW_{j,i}$ is the weight to hidden layer from the j^{th} neuron of the input layer, and $LW_{j,i}$ is the weight to output layer from the j^{th} neuron of the hidden layer. In the equation, the sum of the absolute product of weights for each input is presented by the numerator while the denominator describes all the absolute weights feeding into a hidden unit.

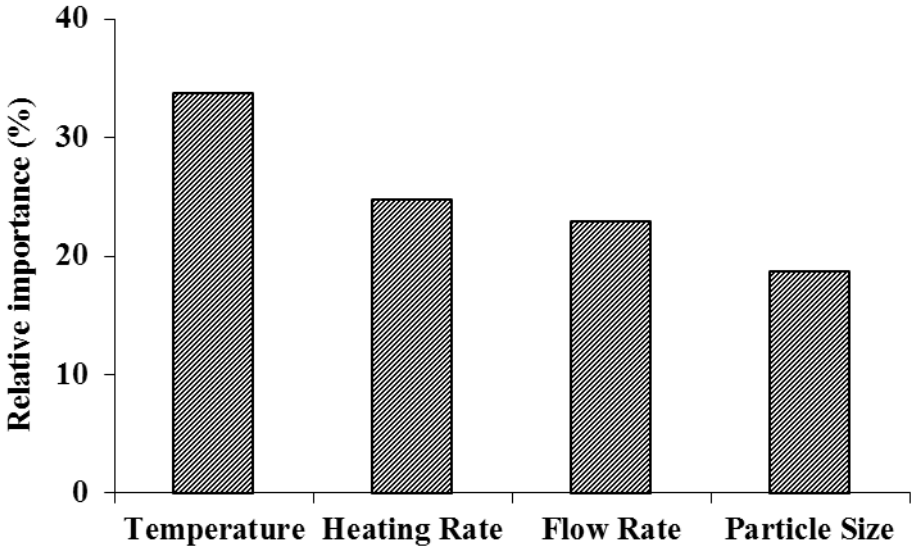

Fig. 4.15: Level of importance of process variables on the bio-oil yield.

Fig. 4.15 depicts the influence of input variables on each of the outputs for the developed ANNs. It is observed that variables accounting for temperature had the strongest effect as it represents 33.68 % of the influence on the bio-oil yield. Heating rate and gas flow rate also have a strong influence on the outputs with variations in the range of 22-25%, and the particle size had the lowest effect among the four variables with a value of 18.71%.

4B.5 Optimization and Modelling of Bio-oil Yield: A Comparison of Classical Approach vs. RSM and ANN Modelling

The traditional approach involves conducting experiments with different process parameters and identifying the combination that produces the highest bio-oil output. During the present study, as described in Chapter 4(a), the highest yield of 30.16% was obtained when conducted at a temperature of 500 °C, a nitrogen flow rate of 150 ml/min, a particle size ranging from 0.25 to 0.50 mm, and a heating rate of 40°C/min. While the RSM model predicted slightly lower yield (29.43%) but the predicted yield (30.01%) by ANN model was almost identical to the experimental yield of 30.16%. This may be attributed to inherent limitations of the models or potential inaccuracies in the conventional approach.

Nevertheless, the real power of RSM lies in its capacity to determine the optimal conditions for achieving the highest possible yield, and in this investigation RSM model predicted a maximum yield of 31.65 % at a temperature of 536.74 °C, a flow rate of 129.55 ml/min, a particle size range of 0.5-0.85 mm, and a heating rate of 40°C/min. This implies

that by modifying the process parameters according to the RSM model, it is possible to achieve a potentially greater yield compared to the traditional or classical approach. The ANN model also predicted a yield of 31.57 % under the specified scenario. However, experimental results show that the measured yield is 31.33 ± 0.09 %, which is quite near to the ANN predicted results.

While the improvement in yield on employing RSM is not dramatic as compared to classical methods, however, it can be economically relevant depending on the scale. RSM offers a more systematic approach and might lead to further optimization in the future. However, the cost-effectiveness and potential limitations of the RSM model also need to be considered.

Therefore, it can be concluded that the classical approach yields reliable empirical findings but requires significant resources. RSM provides a statistical technique for correctly predicting the optimal conditions, resulting in a slightly higher predicted yield of 31.65% compared to the conventional approach's 30.16 %. ANN modeling demonstrates exceptional proficiency in accurately predicting output, closely approximating actual outcomes. Collectively, these techniques can be used collaboratively to improve the efficiency and efficacy of bio-oil production optimization.

4B.6 Summary

During this comprehensive investigation, the focus has been on developing two distinct models that could effectively predict and analyze the biomass pyrolysis outcomes i.e., bio-oil yield. To achieve a robust and accurate analysis, a Four factors-five levels Response Surface Methodology-Central Composite Design (RSM-CCD) and an Artificial Neural Network-Multi-Layer Perceptron (ANN-MLP) model, employing the Levenberg-Marquardt (LM) training algorithm, have been used. The ANN-MLP model was specifically configured with a structure comprising 14 neurons in the hidden layer. Both the mentioned models were rigorously evaluated and subsequently compared for their respective predictive capabilities within the context of biomass pyrolysis. The utilization of the RSM-CCD technique provided insights into the individual and interactive effects of four key factors, each varied at five different levels, on the pyrolysis process. Simultaneously, the ANN-MLP model, with its sophisticated architecture and training algorithm, offered a complementary perspective by capturing complex non-linear relationships inherent in the biomass pyrolysis process. The comparison of these models

not only enhances the reliability of predictions but also provides a nuanced understanding of the interplay between experimental factors and outcomes.

Based on statistical parameters such as R^2, RMSE, SEP, MAE, and AAD, it was found that the ANN was more efficient than the RSM model in predicting bio-oil yield. Better accuracy, as well as the generalization capability of ANN, was also observed even after feeding some additional data. Thus, it can be established that even though RSM is the most widely used method for modeling biomass pyrolysis, the ANN methodology can also satisfactorily model the pyrolysis process. From the relative importance of process parameters, as calculated from the ANN model, it was observed that the pyrolysis temperature was the most significant factor for bio-oil yields, followed by heating rate, nitrogen flow rate, and particle size. A similar finding was observed for the RSM model as well.

References

1. Thoai, D.N., Tongurai, C., Prasertsit, K. and Kumar, A. Predictive capability evaluation of RSM and ANN in modeling and optimization of biodiesel production from palm (*Elaeis guineensis*) oil. *International Journal of Applied Engineering Research*, *13*(10): 7529-7540, 2018.
2. Mehmood, M.A., Ibrahim, M., Rashid, U., Nawaz, M., Ali, S., Hussain, A. and Gull, M., 2017. Biomass production for bioenergy using marginal lands. *Sustainable Production and Consumption*, *9*: 3-21, 2017.
3. Premjet, S. Potential of Weed Biomass for Bioethanol Production. In Basso, T.P. and Basso, L.C. (Eds) *Fuel Ethanol Production from Sugarcane*. IntechOpen., 2018. doi: 10.5772/intechopen.77507
4. Saikia, R., Baruah, B., Kalita, D., Pant, K.K., Gogoi, N. and Kataki, R. Pyrolysis and kinetic analyses of a perennial grass (*Saccharum ravannae* L.) from north-east India: optimization through response surface methodology and product characterization. *Bioresource technology*, *253*: 304-314, 2018.
5. Abnisa, F., Daud, W.W. and Sahu, J.N. Optimization and characterization studies on bio-oil production from palm shell by pyrolysis using response surface methodology. *Biomass and bioenergy*, 35(8): 3604-3616, 2011.
6. Desai, K.M., Survase, S.A., Saudagar, P.S., Lele, S.S. and Singhal, R.S. Comparison of artificial neural network (ANN) and response surface methodology (RSM) in

fermentation media optimization: case study of fermentative production of scleroglucan. *Biochemical Engineering Journal*, *41*(3): 266-273, 2008.

7. Garson, D.G. Interpreting neural network connection weights. *AI Expert* 6: 47-51, 1991.
8. Samuel, O.D. and Okwu, M.O. Comparison of Response Surface Methodology (RSM) and Artificial Neural Network (ANN) in modelling of waste coconut oil ethyl esters production. *Energy Sources, Part A: Recovery, Utilization, and Environmental Effects*, *41*(9): 1049-1061, 2019.
9. Onay, O. Influence of pyrolysis temperature and heating rate on the production of bio-oil and char from safflower seed by pyrolysis, using a well-swept fixed-bed reactor. *Fuel processing technology*, *88*(5): 523-531, 2007.
10. Montoya, J.I., Valdés, C., Chejne, F., Gómez, C.A., Blanco, A., Marrugo, G., Osorio, J., Castillo, E., Aristóbulo, J. and Acero, J. Bio-oil production from Colombian bagasse by fast pyrolysis in a fluidized bed: An experimental study. *Journal of Analytical and Applied Pyrolysis*, *112*: 379-387, 2015.
11. Maran, J.P. and Priya, B. Comparison of response surface methodology and artificial neural network approach towards efficient ultrasound-assisted biodiesel production from muskmelon oil. *Ultrasonics Sonochemistry*, *23*: 192-200, 2015.

Chapter 4C

Assessment of Kinetic Parameters, Mechanisms, and Thermodynamics of *Tithonia Diversifolia* Pyrolysis

4C.1 Introduction

Thermochemical conversion methods, especially pyrolysis, are versatile and efficient in processing biomass for biofuels and chemicals [1, 2]. Thermogravimetric analysis is a profoundly precise technique for the investigation of pyrolysis, and it is proven that each kind of biomass has unique pyrolysis characteristics due to the specific proportions of the components [3]. Kinetic parameters obtained from such analysis using several methods like model-fitting and model-free methods aid in optimizing biofuel production processes. Isoconversional methods, being model-free, offer advantages in determining apparent activation energy without assessing the reaction model, making them effective for analyzing complex pyrolysis reactions in solid feedstocks [4]. From the kinetic data, it is also possible to determine the thermodynamic parameters which are important to define the availability of the process and understand the variation of enthalpy (ΔH), entropy (ΔS), and Gibbs free energy (ΔG) with conversion [5]. These parameters in addition to kinetic parameters (such as activation energy, and pre-exponential factor) are useful in determining the nature of the pyrolysis process in terms of energy requirements and energy balance [6, 9]. For example, the information of ΔH provides an estimation of the energy consumed by pyrolysis to convert the biomass into bioenergy products. A deeper understanding of the reaction kinetics and thermodynamic aspects is indispensable to the design and optimization of a large-scale pyrolysis system [6].

While previous chapters have demonstrated the potential of *Tithonia diversifolia* (TD) as a feedstock for bioenergy through pyrolysis, a critical gap exists in the literature regarding the detailed kinetics, mechanism, and thermodynamics of this promising biomass source [10]. Hence, the objective of this investigation is to comprehend the detailed pyrolysis kinetics and degradation mechanism of TD with the help of thermogravimetric analysis (TGA). On the basis of these TGA data, kinetic parameters including apparent activation energy, and pre-exponential factor of TD were explored by various model-free methods and Craido's master plot method. The CK model offers significant advantages over conventional kinetic analysis techniques, allowing for more accurate and comprehensive determination of kinetic parameters and models for solid-state reactions [32]. The application of the CK model to biomass pyrolysis kinetics remains relatively unexplored in the literatures. In the current investigation, CK model was used to evaluate the kinetic parameters and equations obtained from the CK model at three different heating

rates are also numerically solved to compare experimental and theoretical conversion values. Thermodynamic parameters such as Enthalpy (ΔH), Gibbs free energy (ΔG), and Entropy change (ΔS) were also determined. The results obtained may provide useful knowledge to the research community working in the field of biofuel and bioenergy.

4C.2 Thermogravimetric Analysis

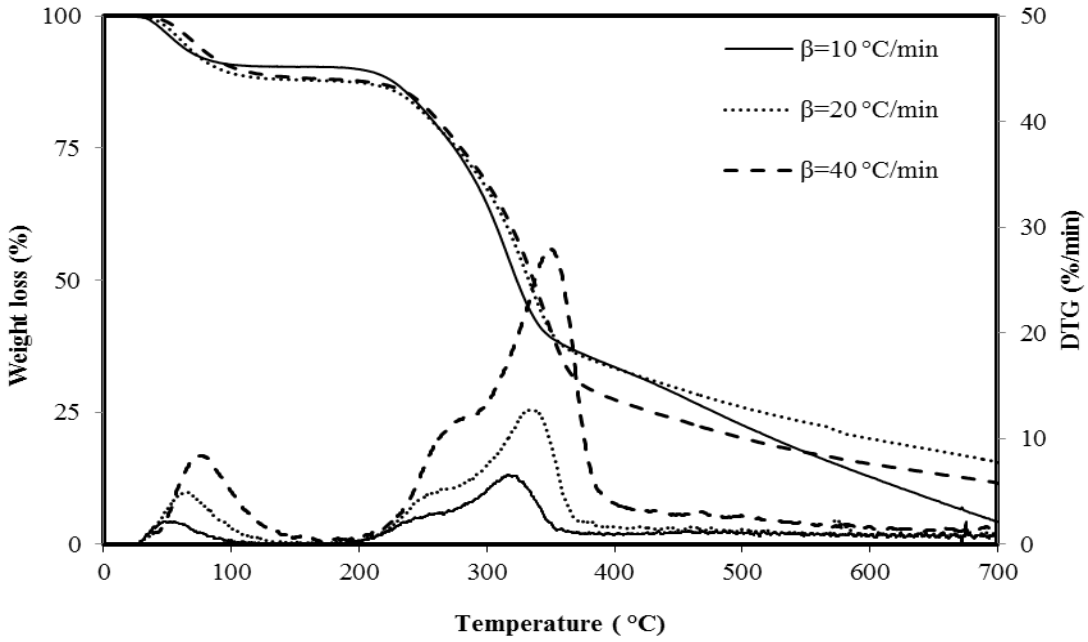

Fig. 4.16 TG/ DTG curves of TD at various heating rates

Fig. 4.16 shows the TG/DTG curves of TD at various heating rates. As can be seen from the figure, similar curves were obtained for all the heating rate conditions. The peak observed in the DTG curves indicates the maximum weight loss rate (dm/dt) as well as the maximum peak temperature (T_m) of a disintegration process. The pyrolysis process can be divided into three zones in the entire temperature range. The mass loss curves of TD exhibit three principal weight loss regions, which correspond to dehydration, devolatilization, and solid decomposition. Among the three zones, the dehydration zone (zone 1) took place in low-temperature region (below 130 °C) and it may be ascribed to the evaporation of physically adsorbed water [16]. This stage can be attributed to the loss of water and light volatile compounds as observed in the TG curve. For this region, a small peak was distinguished in the DTG curve at the temperature range of 40-60 °C. In this investigation, diminishing sample mass in zone 1 was around 6-8%, which correlates with the proximate analysis as the water content of the dry sample was 6.26±0.21 %. The slight increase in

weight loss in this zone compared to the moisture content may be due to the degradation of a few organic components before being released into light volatiles [16].

Table 4.11: Thermal characteristics of TD biomass for active pyrolysis zone (zone 2)

Heating Rate (°C min^{-1})	**T_i (°C)**	**T_m (°C)**	**T_f (°C)**	**-(dm/dt)$_{max}$ (%.min^{-1})**
10	191	313.17	358	6.79
20	197	329.33	362	13.01
40	203	346.33	369	28.98

T_i = Starting temperature of the active pyrolysis zone; T_f= Final temperature of the active pyrolysis zone; T_m =maximum decomposition temperature, -(dm/dt)$_{max}$ =maximum mass loss rate

Large mass loss was observed in Zone 2, which covers a temperature range from 190-370 °C with a peak at about 330 (±15) ºC. In this zone hemicellulose and cellulose components of the biomass decomposed. The characteristics of thermal curves and the weight losses (%) of this stage under heating rates of 10, 20, and 40 °C.min^{-1} are further summarized in Table **4.11**. The weight loss for Zone 2 ranged from 54% to 60%, indicating that this zone is the main pyrolysis stage. As revealed by the biochemical analysis of TD biomass (Table 8), cellulose and hemicellulose are the major components, and the major weight loss region is in accordance with the experimental results. Thus, the pyrolytic characteristics and kinetics of Zone 2 are further investigated in this study. The decomposition in this stage could be attributed to the devolatilization of TD.

From the TGA graph, it has been seen that the third stage starts from around 380 °C, which is described by gradual mass loss due to the slow degradation of the biomass. It demonstrates that at that temperature region, carbonaceous matter is continuously decomposed. It was shown by the horizontal portion of the DTG curve, and this zone is the characteristic of the decomposition of lignin.

From the DTG diagram (**Fig. 4.16)**, it can be seen that the curves generally shift to the right along the horizontal axis as the heating rate gradually rises. This phenomenon is typical for all non-isothermal experiments. The heating rate played an important role in

determining the characteristic temperatures as shown in **Table 4.11**. The characteristic temperatures were shifted to higher values with the increasing heating rate. The effect on characteristic temperatures is predominantly ascribed to the limited rate of heat conduction into the sample brought about by the thermal obstruction of biomass. The increase in the heating rate prompts a concurrent reduction of the temperature effect and an increase in the heat effect [16].

4C.3 Determination of the Thermal Decomposition Model

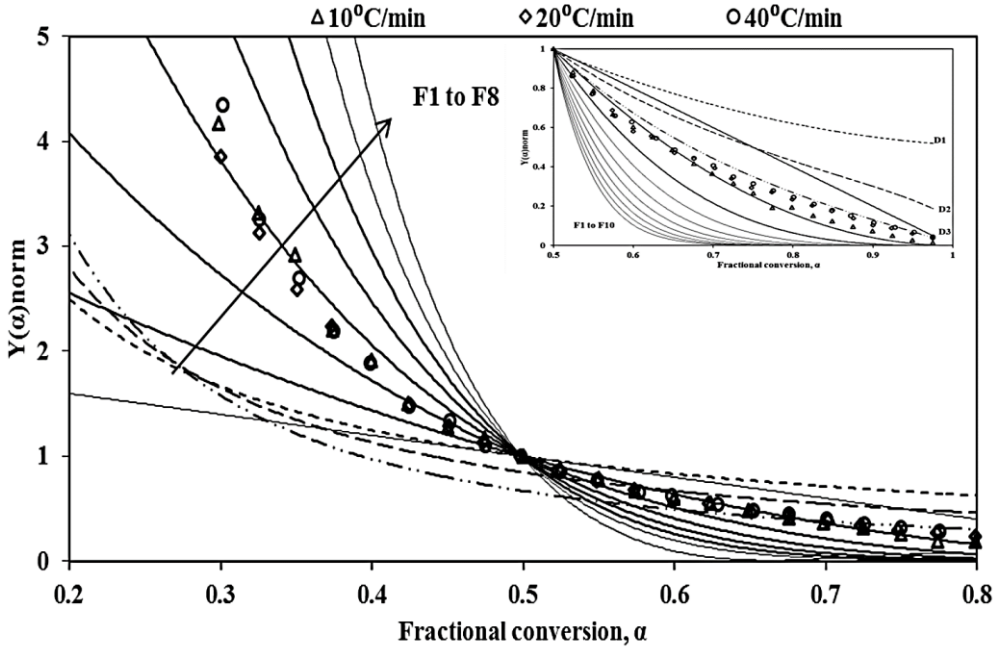

Fig. 4.17: Y(α) master plots

The Y(α) master plot for TD for the whole conversion range is presented in **Fig. 4.17.** Theoretical mechanisms that are suited most to the experimental results are presented in these figures. The results indicated that the degradation of TD follows a few order-based and diffusion models. For the conversion range of 0.20 to 0.725 three types of order-based chemical reaction models were observed. The conversion range of 0.20-0.375 follows the fourth order (F4) model followed by the third order model (F3) and second order model (F2) for the conversion range of 0.375-0.575, and 0.575-0.725, respectively. For the remaining conversion range up to 0.9, three-dimensional diffusion (D3) mechanisms were observed. Various other literatures are also available on biomass following diffusion and order-based models. Pyrolysis of invasive weed biomass, *Phalaris arundinacea*, was found to follow a global reaction mechanism of order F5, which had the main effect on the overall pyrolysis reaction [31]. For another herbaceous biomass, elephant grass or *Pennisetum*

purpureum, Collazzo et al. [8] observed that the experimental plot of the biomass overlaped with the plot of the diffusion (D3) mechanism for conversion (α) below 0.5, followed by an order-based model (F3 third order) thereafter. Sahoo et al. [7] found that *Prosopis juliflora* degradation followed an order-based (order=2–5) and diffusion (D3) reaction mechanism along with the nucleation model. Similarly, the thermal degradation of *Lantana camara* also followed order based (order=1–5), diffusion Dn (n: 3–4), nucleation, and geometrical contraction reaction model [7].

Similar reaction mechanisms were also observed for the thermal degradation of other biomass. For example, Guo and Lua [17] observed a two-step devolatization process during the pyrolysis of extracted oil palm fibers: a 3D diffusion (D3) model for the first stage of conversion and a first-order chemical reaction (F1) model for the later stage of conversion. Similarly, a two-stage mechanism with the same diffusion (D3) and order-based (F1) mechanism was also observed for the pyrolysis of Coir pith [9]. Gogoi et al. [15] obtained three-stage mechanisms of order base (F2), power law, and diffusion (D3) model for *Mesua ferrea* wood and sawmill dust. Carvalho and Tannoushen [18] also obtained the F4, F3, and F2 mechanisms in addition to the F7 mechanism for energy cane *Saccharum robustum* feedstock. Moreover, the n-order mechanism was also observed by Alves et al. [6, 36] for the pyrolysis of Pine-Fruit Shell and açaí seed. Therefore, by utilizing the master plots approach to interpret the reaction model, it becomes clear that the active pyrolysis zone in TD follows specific reaction orders and the diffusion model.

4C.4 Evaluation of Kinetic Parameters

The plots of various *Y-axis functions* as described by Friedman, FWO, and KAS methods against *1/T* for TD in the fractional conversion range of 0.025-0.900 at three heating rates are presented in **Fig. 4.18.**

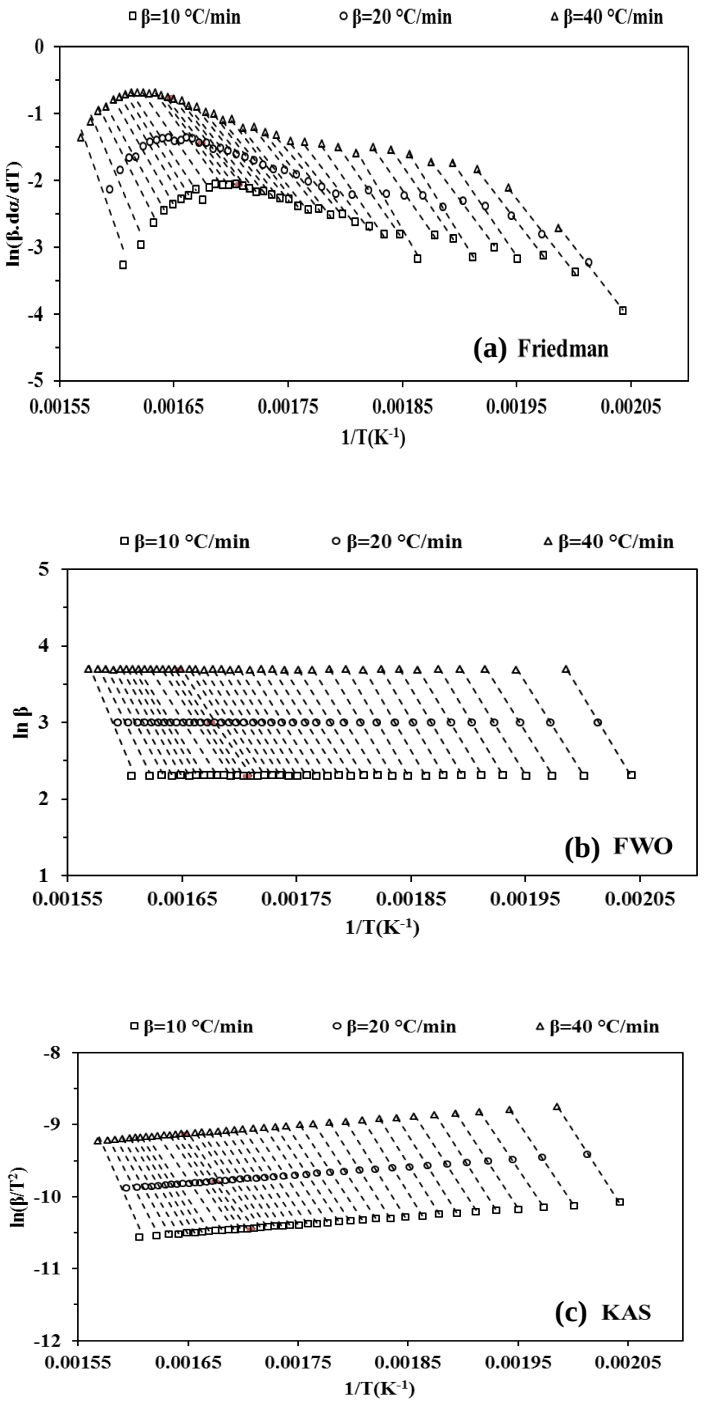

Fig. 4.18 (a) Friedman, (b) FWO and (c) KAS plots

The minimum energy required to start a chemical reaction or to produce an activated complex is considered as the activation energy of the reaction. Lower activation energy demonstrates that a higher reaction rate can be accomplished with lower energy supplies, while higher activation energy values indicate that product formation would require more energy to make a start [19]. The plots of apparent activation energies (E_α) as a function of

fractional conversions (α) for TD as determined by various methods are introduced in **Fig. 4.19**. The R^2 values of different linear plots presented in Fig 4.18 are found to be ≥0.98 for a fractional conversion range of 0.025-0.900. It demonstrates the precision of kinetic data. Slightly lower R^2 values (but greater than 0.91) for Friedman plots have appeared for a conversion range of >0.90. It could have occurred as a significant error during the analysis due to the lesser difference in weight loss data [11]. The apparent activation energies (E_α) determined by the FWO and KAS methods are almost equal and slightly different from the corresponding values as determined by the Friedman method. The reliance of activation energies on fractional conversions, as observed in these methods demonstrates that the decompositions of TD follow various disintegration mechanisms. The thermal transformation of biomass to products is not a simple process because different chemical reactions are generally involved during the pyrolysis depending on the chemical complexity of the biomass [19]. The pre-exponential factors may vary from 10^{13} to 10^{25} min^{-1} for different methods in this investigation, and a higher A-value at higher conversions indicates the dependability on the fractional conversion (α) [19].

The average activation energies and Arrhenius constants for the thermal decompositions of TD are presented in **Table 4.12**. Based on the recommendation given by Vyazovkin et al. [13], the E_o values were calculated by excluding E_α values which differed by more than 30% from the average activation energy value obtained by evaluating all the E_α values within the conversion range of 0.025-0.900. The E_o values for the thermal decompositions of TD determined by the Friedman method are 198.13 kJ mol^{-1}. Similarly, the corresponding values determined by the FWO method is 195.54 kJ mol^{-1} and by the KAS method is 196.15 kJ mol^{-1}. Nearly similar values of energy of activation were obtained with the integral isoconversional methods such as KAS and FWO methods. A similar range of values of activation energy was also observed for the differential method - Freidman method, and the result obtained are consistent with other published literature [33]. However, as mentioned earlier, the correlation coefficients were higher for the lineal integral methods at almost every conversion value.The Arrhenius constants of TD determined by the Miura-Maki method fluctuate between 2.27×10^{16} – 2.51×10^{24} min^{-1} for the conversion range of 0.025-0.900. The mean apparent Arrhenius constant (A_o) determined by the Miura-Maki method is 6.44×10^{22} min^{-1}. This value falls within the proximity of other reported invasive weed species, such as *Parthenium hysterophorus* (8.38×10^{23} min^{-1}) [20]. As the A values of the TD pyrolysis were larger than 10^{10} min^{-1}, it

indicates the active pyrolysis zone of TD was a simple complex process [21]. The E_o values obtained for TD are higher than few other weed plants such as *Parthenium hysterophorus* (145-148 kJ mol^{-1}) [20]; *Prosopis juliflora* (138-157 kJ mol^{-1}) [12]; Reed Canary (*Phalaris arundinacea*) (160 kJ mol^{-1}) [31], coastal Plant Species - *Artemisia annua* (169.69 kJ mol^{-1}) and *Chenopodium glaucum* (170.48 kJ mol^{-1}) [10]. Also, the E_o values are in close or within the range of other biomass such as *L. japonica* (117.4 to 295.3 kJ mol^{-1}) [22]; and Camel grass (96–192 kJ mol^{-1}) [23]. Likewise, the obtained E_o values were lower than water hyacinth (238.57 kJ mol^{-1}) [24]; *Spartina anglica* (291.57 kJ mol^{-1}) [14], and swine manure digestate (206.45–209.51 kJ mol^{-1}) [25], etc. These values indicated the feasibility of TD biomass for co-pyrolysis with several other biomass types.

Table 4.12: Mean activation energies and frequency factors determined by various methods

Methods	**Results**
Stage I	Fourth-order (F4) reaction model
Stage II	Third-order (F3) reaction model
Stage III	Second-order (F2) reaction model
Stage IV	Three-dimensional diffusion (D3) model
Average Activation energy (kJ mol^{-1})	
Friedman	198.13
KAS/Miura-Maki	196.15
FWO	195.54
Average Pre-exponential factor (min^{-1})	
Miura-Maki	9.51×10^{22}
Friedman	1.77×10^{20}
KAS	5.25×10^{18}
FWO	4.10×10^{18}

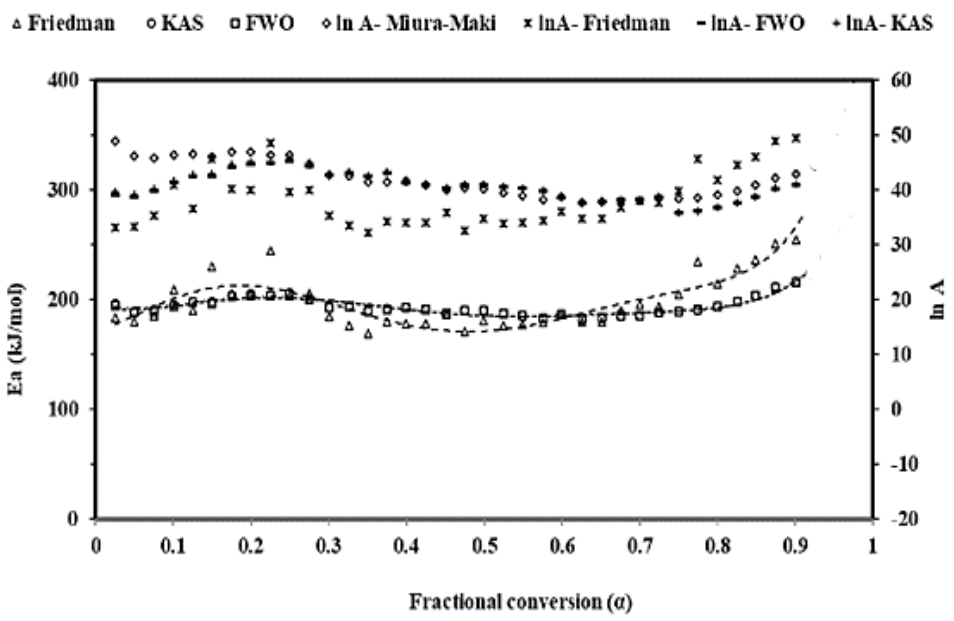

Fig. 4.19: *Apparent activation energies (E_α)* and *lnA* as a function of fractional conversions (α) for Friedman, KAS, FWO, and Miura-Maki method

4C.5 Evaluations of Thermodynamic Parameters

The thermodynamic parameters indicate the presence of favorable conditions for the pyrolysis of TD. **Fig. 4.20** shows the plots of enthalpy, entropy, and Gibbs free energy changes as a function of α for the TD degradation process for the Miura Maki method. Enthalpy change (ΔH) of a thermal conversion process reflects the energy contrasts between the activated complex and the reactants. As the ΔH>0 (**Fig. 4.20**), the pyrolysis of TD is an endothermic reaction, i.e., external energy is required to occur the reaction [21]. In addition, a small difference of ΔH and E_a value (5.01 kJ mol^{-1}) was obtained at a different conversion rate, indicating that the product formation is being favored in an energy-efficient manner due to lower potential energy [21, 26]. Similar differences were also observed for a few previously studied biomasses including microalgae, aquatic biomass, and other lignocellulosic biomasses [6, 19, 27].

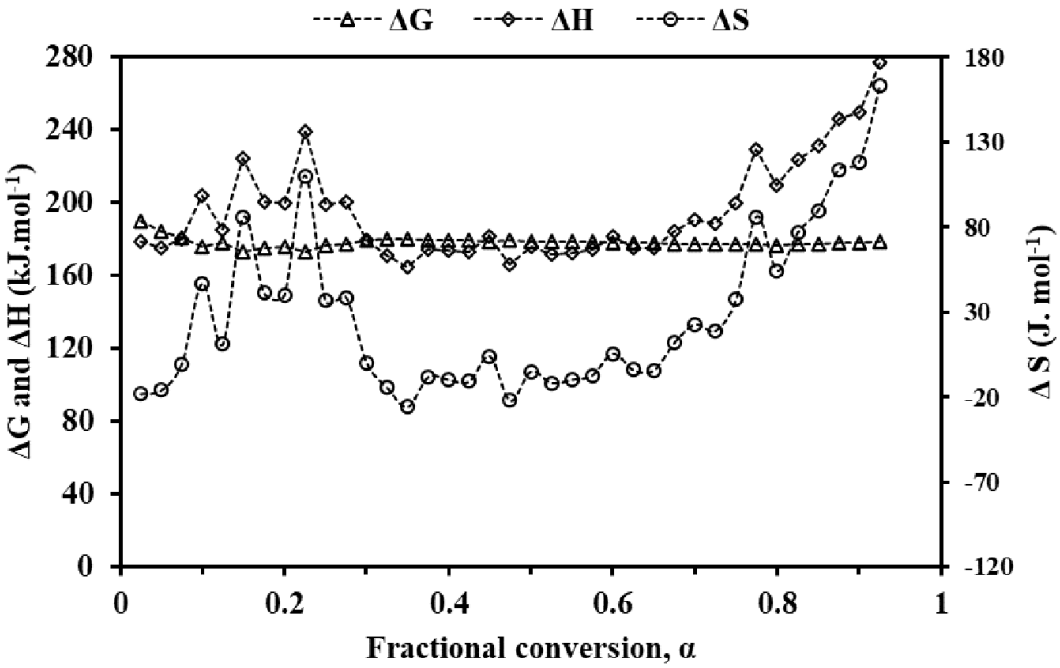

Fig.4.20: Plot of various thermodynamic parameters as a function of fractional conversion.

Gibbs free energy (ΔG) is the energy deposited in a material during thermal transformation. Gibbs free energy change (ΔG) represents the usable energy available in a reaction at constant temperature and pressure. It reflects the balance between enthalpy and entropy of a system. A negative ΔG indicates a spontaneous reaction that releases usable energy and proceeds readily. The more negative the ΔG, the greater the driving force for the reaction and the easier it is to form the products. Conversely, a positive ΔG signifies a non-spontaneous reaction requiring an energy input to occur [26]. The ΔG of TD decomposition is 123–180 kJ mol^{-1} (**Fig 4.20**), which is well within the values reported for some other biomass sources such as wolffia, camphorwood, and water hyacinth [26-28]. The positive ΔG value also indicates that TD pyrolysis is a nonspontaneous process.

Change in entropy (ΔS) can be used to foresee the product properties. While a negative ΔS (-ΔS) shows the products are more ordered compared to the reactants, a positive ΔS (+ΔS) reflects the opposite, indicating the products are more disordered than the reactants [26]. In the context of TD pyrolysis, both negative and positive ΔS values were observed, pointing to the complexity of the biomass and associated reactions.

The negative ΔS signifies proximity to thermodynamic equilibrium, suggesting a higher order in products like biochar than in the initial reactants. Conversely, positive ΔS

values across the conversion range suggest a high degree of disorder in the final product compared to the initial biomass, limiting the system's energy available to form the activated complex. Additionally, the positive entropy change suggests a less stable activated complex, leading to a dissociative pathway in biomass conversion [29, 34]. This may further indicate the formation of more gas and liquid products during TD pyrolysis. The values of thermodynamic parameters have shown that it has great significance in designing the pyrolysis reactor and choosing the target biofuels.

4C.6 Combined Kinetic Model

The TG data obtained for TD was also analyzed by using the Sestak-Berggren combined kinetic model (CK model). For obtaining the meaningful kinetic parameters namely, activation energy, Arrhenius constant, and parameters related to the mechanism of the conversion process (m, n, and p), optimization of eq. (29) was done by considering all the three heating rates. The m, n, and p parameters of the CK model provide information regarding the reaction order model, power law model, and nucleation model respectively and therefore a combination of these parameters in a single equation is quite useful for understanding kinetics and the mechanism of a conversion process. Considering the results obtained from Y(α) master plots, the mechanism parameters for this investigation are set within the intervals, nϵ{0, 7}, mϵ{-8, 8} and pϵ{-8, 8}. **Fig. 4.21** shows the plots of the left-hand side of eq.(31) as a function of -1/T for one-step thermal degradations of TD. Pearson's ratio of linear regressions for the sample is > 0.995, which indicates that the one-step mechanism parameters can be used to explain the pyrolysis of biomass.

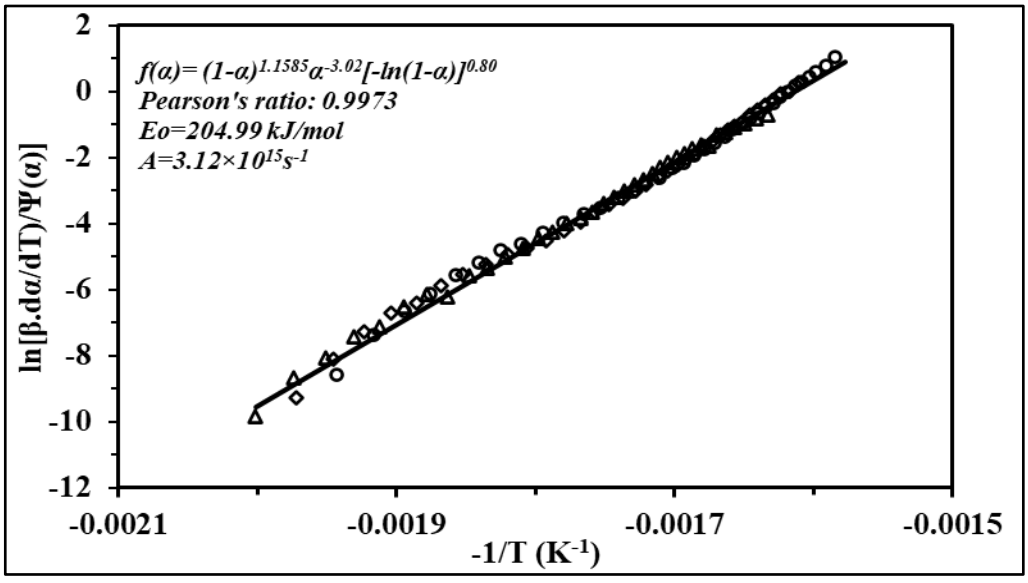

Fig. 4.21: Single-step combined kinetic model fit results

The activation energy of TD as determined by the CK model is 204.99 kJ mol^{-1}, which is similar to the values predicted by Friedman and other isoconversional methods with <5% deviations. The combined kinetic equations of the TD single-step devolatilization process can be expressed by the following equation:

$$\frac{d\alpha}{dT} = \frac{3.12\times10^{15}}{\beta}\exp(\frac{-204988}{RT})(1-\alpha)^{1.1585}\alpha^{-3.02}[-\ln(1-\alpha)]^{0.80} \quad \ldots\ldots(32)$$

The n-values greater than unity indicate that the devolatilizations of TD can be described by considering the order-based model as the primary devolatilization mechanism along with diffusion and geometrical contraction as weak counterparts. The negative m-value (-3.02) also indicates that the devolatilization of TD is controlled by diffusion mechanisms [30]. This supports our finding, i.e., the pyrolysis mechanism of TD is mostly an order-based model with a small part following a diffusion model. Although the p-value indicates the devolatilization of TD follows the nucleation mechanism, there is no nucleation mechanism observed in the master plot method.

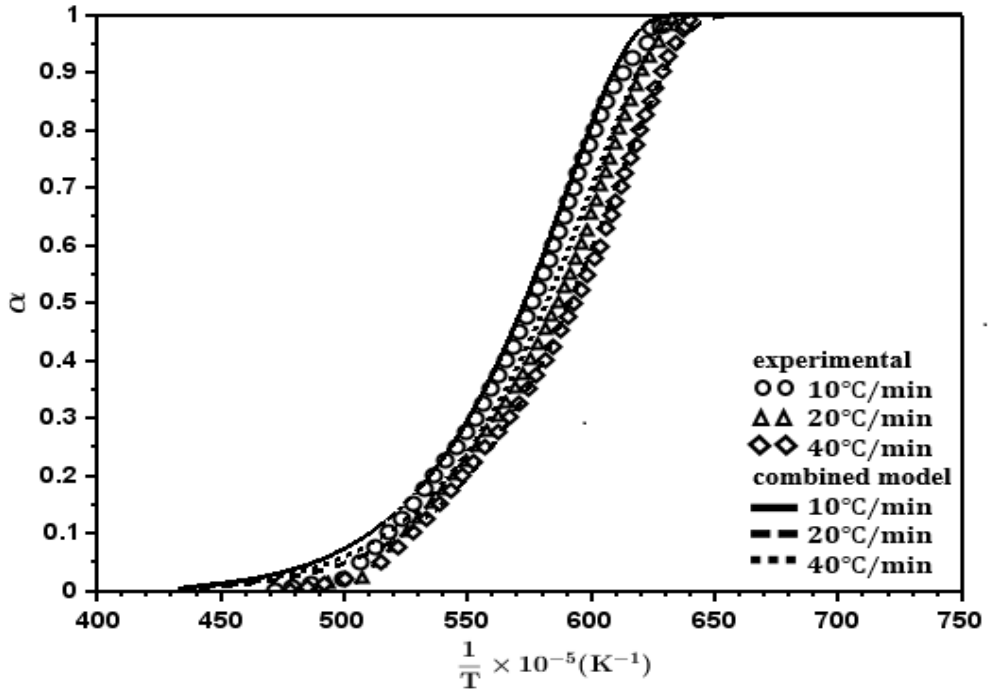

Fig. 4.22: Experimental and calculated curves obtained at different heating rates for single step devolatilization process

Eqn. (32) at three different heating rates are numerically solved by 4th-order Runge-Kutta and Milne-Simpsons predictor-corrector methods to compare experimental and theoretical conversion values. Both methods give comparable results and the comparisons

of experimental and calculated curves obtained from the Runge-Kutta method at different heating rates for the single-step devolatilization process are presented in **Fig. 4.22**.

The standard deviation as calculated from the experimental and calculated curves is ±0.6. It can be seen from Fig. 4.22 that the theoretical model gives a very slight deviation for 20 ˚C/min heating rate, compared to experimental model. Such minor discrepancies between theoretical and experimental data are very common in complex processes like biomass devolatilization, suggesting the potential application of a multistep model in biomass pyrolysis for more accuracy.

4C.7 Kinetic Compensation Effect

The pre-exponential factors (A_α) were calculated by substituting the value of $f(\alpha) = (1-\alpha)^{1.1585}\alpha^{-3.02}[-\ln(1-\alpha)]^{0.80}$ into Eq. (18). As can be seen from **Fig. 4.19**, pre-exponential factors ($\ln A_\alpha$) are not constant (lnA=32.14–49.50) but varies in a wide range, 9.14×10^{13}–1.00×10^{34} min^{-1}. A similar range of A (or A_α) values was also shown by smoked cigarette butt [35], plastic solid waste [34], etc. The linear dependence of $\ln A_\alpha$ values and the apparent activation energies (E_α) (i.e., kinetic compensation effect) on α permits us to determine the E_o and A_o values from the following equations:

$$\ln A_\alpha = b + aE_\alpha \qquad \text{.....(33)}$$

$$\ln A_o = b + aE_o \qquad \text{.....(34)}$$

where a and b are unknown parameters that can be obtained from the slope and intercept of the plot of $\ln A_\alpha$ vs E_α, respectively.

The observed weakness in linear regressions of energy compensation effects across the entire pyrolysis process indicates that a one-step reaction model is insufficient to describe biomass pyrolysis complexity. Therefore, we divided the active pyrolysis zone into three stages. Interestingly, as depicted in **Fig 4.23**, the ln(A) vs. E_a plot exhibits three distinct stages, each with a strong linear correlation.

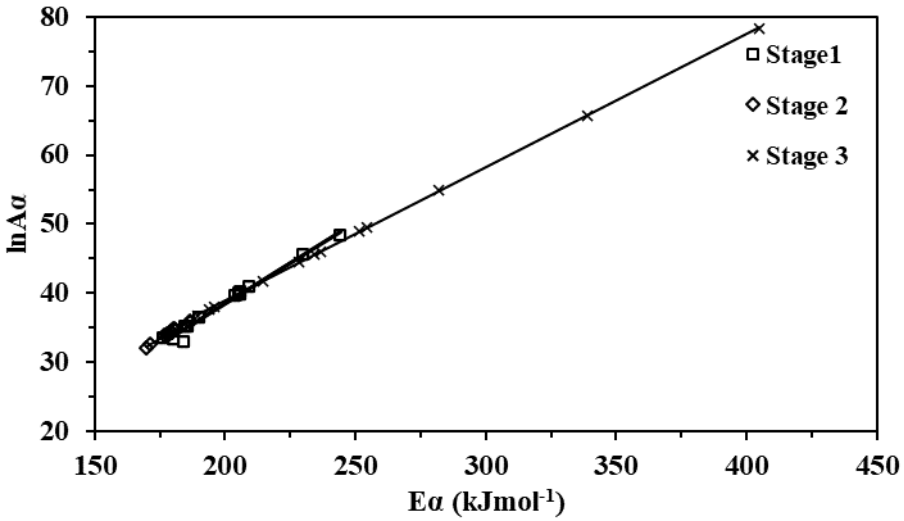

Fig. 4.23: Plots of E_α as a function of $\ln A_\alpha$ for different pyrolytic decompositions stages of TD

The conversion range of stages are 0–0.30; 0.30–0.625; 0.650–1, representing 1st stage, 2nd stage and 3rd stage respectively. The R^2 values presented in Table 4.13 demonstrate the presence of strong linear relationships for all steps. The correlation parameters (i.e., a and b) for different steps were determined from the slope and intercept of the straight lines of **Fig. 4.23** and presented in **Table 4.13**. The degradation in the 1st, 2nd, and 3rd stages may primarily indicate the breakdown of pseudo-hemicelluloses, cellulose, and lignin, respectively [30].

Table 4.13: Kinetic parameters of different stages of the one-step thermal decomposition process of TD determined by Friedman methods.

Stage I			**Stage II**			**Stage III**		
A	b	R^2	a	b	R^2	a	b	R^2
0.2355	-8.5670	0.9841	4.5549	23.3436	0.9872	5.1739	-1.2027	0.999
Kinetic parameters*								
E_o	A_o		E_o	A_o		E_o	A_o	
200.24	1.56×10^{19}		178.90	1.95×10^{13}		248.44	1.30×10^{31}	

* E_o, in kJ mol^{-1}, A_o in min^{-1}

4C.8 Summary

The assessments of thermo-kinetic and thermodynamic parameters as well as the degradation model of TD pyrolysis affirm that it is a multistep thermal devolatilization process. The outcomes demonstrated that the average activation energies (E_a) for Friedman, FWO, and KAS methods were 198.13, 196.12, and 195.54 kJ mol^{-1}, respectively. Further, the reaction chemistry of the main decomposition stage elucidated that the most probable pyrolysis kinetic model for devolatilization of the TD went through a set of order-based (F4, F3, and F2) and diffusion (D3) reactions, indicating the complex mechanism of the biomass pyrolysis. The appearance of both positive as well as negative entropy change values also supports the formation of complex products from the TD pyrolysis. A smaller difference between the enthalpies and apparent activation energies suggests that the potential energy barrier needed to generate an activated complex and subsequent product formation can be easily overcome. The values of kinetic parameters provided useful information for designing a pyrolytic processing system using *Tithonia diversifolia* as a feedstock, and establishing this weed as a potential feedstock for bioenergy and biofuel generation. Sestak-Berggren combined kinetic model (CK model) results reveal that the single-step pyrolysis of biomass can be described by $f(\alpha) = (1-\alpha)^{1.1585}\alpha^{-3.02}[-\ln(1-\alpha)]^{0.80}$. The activation energies and Arrhenius constants predicted from CK models are almost equal to the value predicted by isoconversional methods.

References

1. Bach, Q. V., and Chen, W. H., Pyrolysis characteristics and kinetics of microalgae via thermogravimetric analysis (TGA): A state-of-the-art review. *Bioresource technology*, *246*, 88-100, 2017.
2. Bridgwater, T. Biomass for energy. *Journal of the Science of Food and Agriculture* 86(12): 1755-1768, 2006.
3. Lira, T. S., Santos, K. G., Murata, V. V., Gianesella, M., and Barrozo, M. A., The use of nonlinearity measures in the estimation of kinetic parameters of sugarcane bagasse pyrolysis. *Chemical Engineering & Technology*, *33*(10), 1699-1705, 2010.
4. Choudhury, N.D., Bhuyan, N., Bordoloi, N. *et al.* Production of bio-oil from coir pith via pyrolysis: kinetics, thermodynamics, and optimization using response surface methodology. *Biomass Conversion and Biorefinery*, **11**, 2881–2898, 2021.

5. Alves, J. L. F., da Silva, J. C. G., da Silva Filho, V. F., Alves, R. F., de Araujo Galdino, W. V., and De Sena, R. F. Kinetics and thermodynamics parameters evaluation of pyrolysis of invasive aquatic macrophytes to determine their bioenergy potentials. *Biomass and bioenergy*, *121*, 28-40, 2019.
6. Alves, J. L. F., Da Silva, J. C. G., Di Domenico, M., Galdino, W. V. D. A., Andersen, S. L. F., Alves, R. F., and De Sena, R. F., Exploring Açaí seed (*Euterpe oleracea*) pyrolysis using multi-component kinetics and thermodynamics assessment towards its bioenergy potential. *BioEnergy Research*, *14*, 209-225, 2021.
7. Sahoo, A., Kumar, S., Kumar, J., & Bhaskar, T., A detailed assessment of pyrolysis kinetics of invasive lignocellulosic biomasses (*Prosopis juliflora* and *Lantana camara*) by thermogravimetric analysis. *Bioresource Technology*, *319*, 124060, 2021.
8. Collazzo, G. C., Broetto, C. C., Perondi, D., Junges, J., Dettmer, A., Dornelles Filho, A. A., ... and Godinho, M., A detailed non-isothermal kinetic study of elephant grass pyrolysis from different models. *Applied Thermal Engineering*, *110*, 1200-1211, 2017.
9. Alves, J. L. F., Da Silva, J. C. G., da Silva Filho, V. F., Alves, R. F., Ahmad, M. S., Ahmad, M. S., ... and De Sena, R. F., Bioenergy potential of red macroalgae Gelidium floridanum by pyrolysis: evaluation of kinetic triplet and thermodynamics parameters. *Bioresource technology*, *291*, 121892, 2019.
10. Li, L., Wang, X., Sun, J., Zhang, Y., and Qin, S. Pyrolytic and kinetic analysis of two coastal plant species: *Artemisia annua* and *Chenopodium glaucum*. *BioMed Research International*, *2013*(1), 162907, 2013.
11. Cai, J., Xu, D., Dong, Z., Yu, X., Yang, Y., Banks, S. W., & Bridgwater, A. V. (2018). Processing thermogravimetric analysis data for isoconversional kinetic analysis of lignocellulosic biomass pyrolysis: Case study of corn stalk. *Renewable and Sustainable Energy Reviews*, *82*, 2705-2715, 2018.
12. Ramesh, N., and Murugavelh, S. (2020). A cleaner process for conversion of invasive weed (*Prosopis juliflora*) into energy-dense fuel: kinetics, energy, and exergy analysis of pyrolysis process. *Biomass Conversion and Biorefinery*, 12: 3067–3080, 2022.

13. Vyazovkin, S., Burnham, A. K., Criado, J. M., Pérez-Maqueda, L. A., Popescu, C., and Sbirrazzuoli, N., ICTAC Kinetics Committee recommendations for performing kinetic computations on thermal analysis data. *Thermochimica acta*, *520*(1-2): 1-19, 2011.
14. Yan, H. X., Hou, F. F., Zhao, H., Wang, H. N., Gao, S., Wu, M., ... and Qin, S. Pyrolysis kinetics of invasive coastal plant *Spartina anglica* using thermogravimetric analysis. *Energy Sources, Part A: Recovery, Utilization, and Environmental Effects*, *38*(19), 2867-2875, 2016.
15. Gogoi, M., Konwar, K., Bhuyan, N., Borah, R. C., Kalita, A. C., Nath, H. P., and Saikia, N., Assessments of pyrolysis kinetics and mechanisms of biomass residues using thermogravimetry. *Bioresource technology reports*, *4*, 40-49, 2018.
16. Hu, Z., Chen, Z., Li, G., Chen, X., Hu, M., Laghari, M., ... and Guo, D., Characteristics and kinetic studies of *Hydrilla verticillata* pyrolysis via thermogravimetric analysis. *Bioresource technology*, *194*, 364-372, 2015.
17. Guo, J., and Lua, A., Effect of heating temperature on the properties of chars and activated carbons prepared from oil palm stones. *Journal of Thermal Analysis and Calorimetry*, *60*(2), 417-425, 2000.
18. de Carvalho, V. S., and Tannous, K., Thermal decomposition kinetics modeling of energy cane *Saccharum robustum*. *Thermochimica acta*, *657*, 56-65, 2017.
19. Shahid, A., Ishfaq, M., Ahmad, M. S., Malik, S., Farooq, M., Hui, Z., ... and Mehmood, M. A., Bioenergy potential of the residual microalgal biomass produced in city wastewater assessed through pyrolysis, kinetics and thermodynamics study to design algal biorefinery. *Bioresource technology*, *289*, 121701, 2019.
20. Dhaundiyal, A., Singh, S. B., Hanon, M. M., and Rawat, R., Determination of kinetic parameters for the thermal decomposition of *parthenium hysterophorus*. *Environmental and Climate Technologies*, *22*(1), 5-21, 2018.
21. Qing, X., Xiaoqian, M., Zhaosheng, Y., Zilin, C., and Changming, L., Decomposition characteristics and kinetics of microalgae in N_2 and CO_2 atmospheres by a thermogravimetry. *Journal of Combustion, 2017*. https://doi.org/10.1155/2017/6160234
22. Han, T. U., Kim, Y. M., Siddiqui, M. Z., Lee, T., Watanabe, A., Teramae, N., ... and Park, Y. K., Non-isothermal pyrolysis properties of *Laminaria japonica*. *Journal of analytical and applied pyrolysis*, *130*, 277-284, 2018.

23. Mehmood, M. A., Ye, G., Luo, H., Liu, C., Malik, S., Afzal, I., ...and Ahmad, M. S., Pyrolysis and kinetic analyses of Camel grass (*Cymbopogon schoenanthus*) for bioenergy. *Bioresource technology*, *228*, 18-24, 2017.
24. Mallick, D., Bora, B.J., Barbhuiya, S.A., Banik, R., Garg, J., Sarma, R., and Gogoi, A.K., Detailed study of pyrolysis kinetics of biomass using thermogravimetric analysis. In *AIP Conference Proceedings*, Volume 2091(1), pages 020014, 2019. AIP Publishing LLC https://doi.org/10.1063/1.5096505.
25. Vuppaladadiyam, A. K., Liu, H., Zhao, M., Soomro, A. F., Memon, M. Z., and Dupont, V Thermogravimetric and kinetic analysis to discern synergy during the co-pyrolysis of microalgae and swine manure digestate. *Biotechnology for biofuels*, *12*, 1-18, 2019.
26. Ahmad, M. S., Mehmood, M. A., Al Ayed, O. S., Ye, G., Luo, H., Ibrahim, M., ... and Qadir, G., Kinetic analyses and pyrolytic behavior of Para grass (*Urochloa mutica*) for its bioenergy potential. *Bioresource technology*, *224*, 708-713, 2017.
27. Afzal, I., Ahmad, M. S., Malik, S., Ibrahim, M., Al Ayed, O. S., Qadir, G., ... and Gull, M., Thermodynamics and kinetics parameters of Eichhornia crassipes biomass for bioenergy. *Protein and Peptide Letters*, *25*(2), 187-194, 2018.
28. Xu, X., Pan, R., Li, P., and Chen, R., Kinetics, thermodynamics, and volatile products of camphorwood pyrolysis in inert atmosphere. *Applied Biochemistry and Biotechnology*, *191*, 1605-1623, 2020.
29. Li, H., Zhou, N., Dai, L., Cheng, Y., Cobb, K., Chen, P., and Ruan, R., Effect of lime mud on the reaction kinetics and thermodynamics of biomass pyrolysis. *Bioresource Technology*, *310*, 123475, 2020.
30. Wang, X., Hu, M., Hu, W., Chen, Z., Liu, S., Hu, Z., and Xiao, B., Thermogravimetric kinetic study of agricultural residue biomass pyrolysis based on combined kinetics. *Bioresource technology*, *219*, 510-520, 2016.
31. Alhumade, H., da Silva, J. C. G., Ahmad, M. S., Çakman, G., Yıldız, A., Ceylan, S., and Elkamel, A., Investigation of pyrolysis kinetics and thermal behavior of Invasive Reed Canary (Phalaris arundinacea) for bioenergy potential. *Journal of Analytical and Applied Pyrolysis*, *140*, 385-392, 2019.
32. Nath, H. P., Dutta, B. K., Bhuyan, N., Saikia, B. K., and Saikia, N. A comprehensive study on the transition metal–catalysed pyrolysis kinetics, thermodynamics and

mechanisms of bamboo powder. *Biomass Conversion and Biorefinery*, 13, 5043–5057, 2023.

33. Cortés, A. M., and Bridgwater, A. V., Kinetic study of the pyrolysis of miscanthus and its acid hydrolysis residue by thermogravimetric analysis. *Fuel Processing Technology*, *138*, 184-193, 2015.
34. Mumbach, G. D., Alves, J. L. F., Da Silva, J. C. G., De Sena, R. F., Marangoni, C., Machado, R. A. F., & Bolzan, A., Thermal investigation of plastic solid waste pyrolysis via the deconvolution technique using the asymmetric double sigmoidal function: Determination of the kinetic triplet, thermodynamic parameters, thermal lifetime and pyrolytic oil composition for clean energy recovery. *Energy Conversion and Management*, *200*, 112031, 2019.
35. Alves, J. L. F., da Silva, J. C. G., Mumbach, G. D., da Silva Filho, V. F., Di Domenico, M., de Sena, R. F., ... & Marangoni, C.. Thermo-kinetic investigation of the multi-step pyrolysis of smoked cigarette butts towards its energy recovery potential. *Biomass Conversion and Biorefinery*, 12, 741–755, 2022..
36. Alves, J. L. F., Da Silva, J. C. G., da Silva Filho, V. F., Alves, R. F., de Araujo Galdino, W. V., Andersen, S. L. F., and De Sena, R. F., Determination of the bioenergy potential of Brazilian pine-fruit shell via pyrolysis kinetics, thermodynamic study, and evolved gas analysis. *BioEnergy Research*, *12*(1), 168-183, 2019.

Chapter 4D

Effect of Catalysts on Pyrolysis Products of *Tithonia Diversifolia*: Kinetic Study and Thermodynamics

4D.1 Introduction

Various technologies, including biological conversion and thermochemical conversions, have been explored for liquid fuel production from biomass. Pyrolysis, a sustainable thermochemical method, operates at moderate temperatures (400–700°C) without oxygen, yielding liquids, gases, and char [3]. The quantity and quality of pyrolysis products depend on experimental parameters and feedstock properties [4]. Although bio-oil, a key pyrolysis product, contains a rich variety of organic compounds that hold promise for industrial use, its high oxygen content makes it unsuitable as a direct fuel source [5, 6]. Advanced technologies (e.g., hydrogenation, catalytic pyrolysis, catalytic cracking, emulsification) are essential to reduce oxygen content in bio-oil and enhance its quality [1, 6-8]. In recent times, catalytic pyrolysis has gained attention for improving bio-oil quality through several reactions like cracking, decarbonylation, decarboxylation, and deoxygenation [9]. The catalytic pyrolysis is operable at atmospheric pressure, and hence cost-effective and it improves the quality of the bio-oil and increases product yields [3, 7]. Zeolites, among various catalysts, stand out due to their abundance, cost-effectiveness, and tunability [8]. Over the past three decades, zeolites, particularly ZSM-5, have proven to be preeminent catalysts, efficiently converting carbohydrates into aromatics and olefins, influencing oxygen reduction in pyrolytic vapors, and enhancing the carbon-to-oxygen ratio [3, 8, 10].

While there has been extensive research conducted on biomass pyrolysis applying ZSM-5 catalyst, there is limited literature available on the effects of metal-impregnated ZSM-5 catalysts on the resulting pyrolytic products using Fixed bed pyrolysis reactor. The utilization of thermogravimetric analysis (TGA) provides unique insights into biomass characteristics, aiding in the optimization of biofuel production processes, including evaluation of kinetic and thermodynamic parameters [11]. Furthermore, the kinetic study of biomass catalytic pyrolysis, which discusses the relationship between the pyrolysis mechanism and the obtained experimental data, has received very little attention. The primary objective of this research is to compare the production of pyrolytic oil or bio-oil through non-catalytic and catalytic pyrolysis of TD in a fixed-bed reactor. Our investigation aims to explore the significance of transition metals (Co and Ni) impregnated ZSM-5 catalysts on pyrolytic products distribution, and pyrolytic oil properties using different

analytical techniques. Furthermore, the study included an analysis on how these catalysts impacted the kinetics and thermodynamics of biomass.

4D.2 Characterization of Catalysts

4D.2.1 XRD

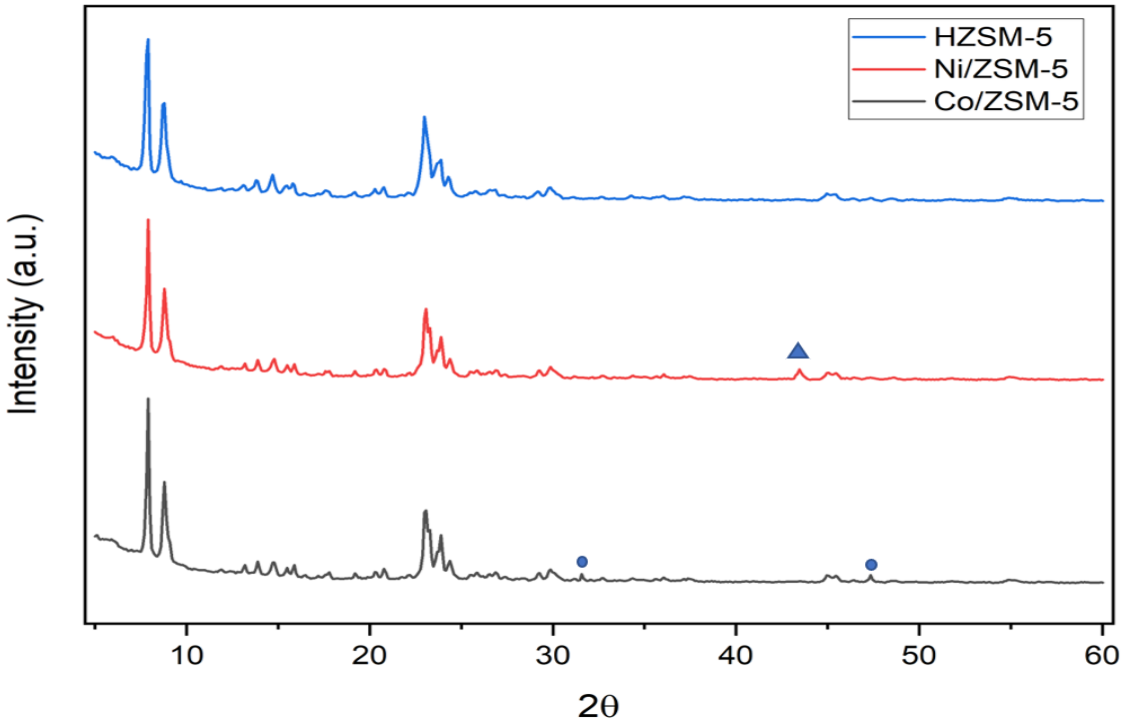

Fig. 4.24: Powder X-ray diffraction pattern of different catalysts (HZSM-5, Co/ZSM-5, and Ni/ZSM-5)

Fig. 4.24 depicts the XRD patterns of the catalysts. As all catalysts were calcined during synthesis, added metals are supposed to be in the oxide phase. All the samples have identical characteristic peaks (2θ= 7-9° and 23-25°) of the MFI structure (JCPDS no. 44–0003). However, there are only a slight variation is observed in diffraction peak intensities for the metal-impregnated catalysts [15, 16]. The low angle diffraction peak (2θ<10°) for all the samples indicates metal impregnation does not affect the orderly crystalline structure of ZSM-5. Notably, only a few diffraction peaks attributed to metal species are observed, possibly due to their very low content or uniform dispersion of Co and Ni on the ZSM-5 zeolite. Two small peaks of cobalt can be seen in the XRD pattern of Co/ZSM-5, in 2θ 31.6° and 47.3°; corresponding to the detection of Co_3O_4, in accordance with the existing

literature on cobalt-containing ZSM-5 zeolites [23]. Similarly, a small peak of NiO is observed at 2θ 43.2° [30].

4D.2.2 SEM and EDX Analysis

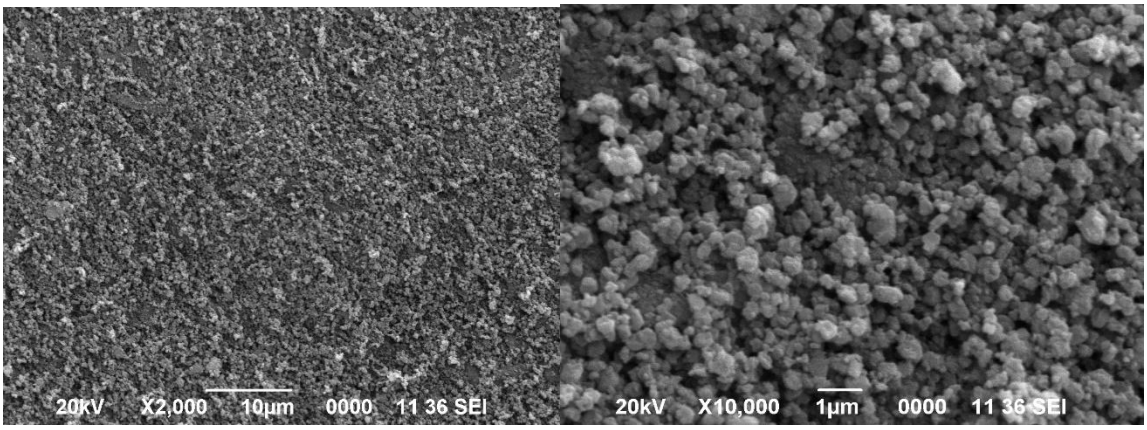

(A)

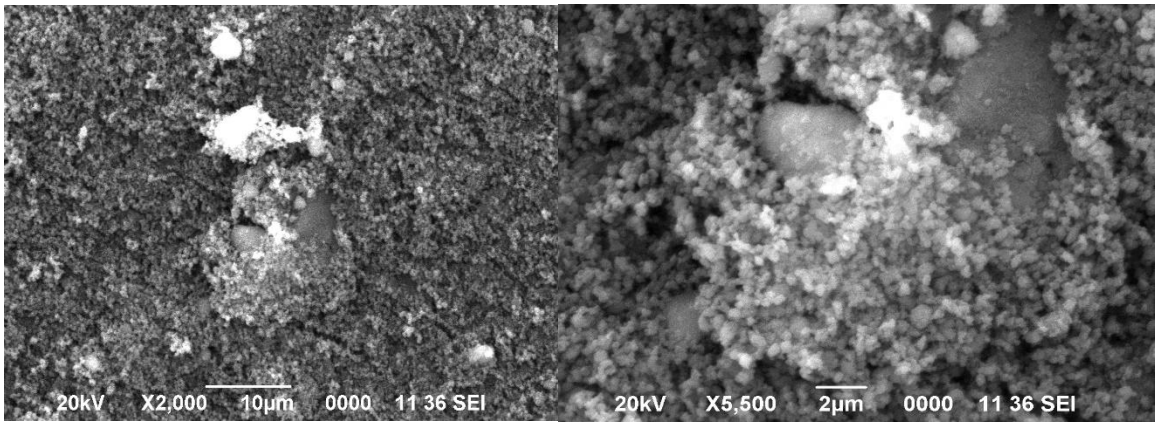

(B)

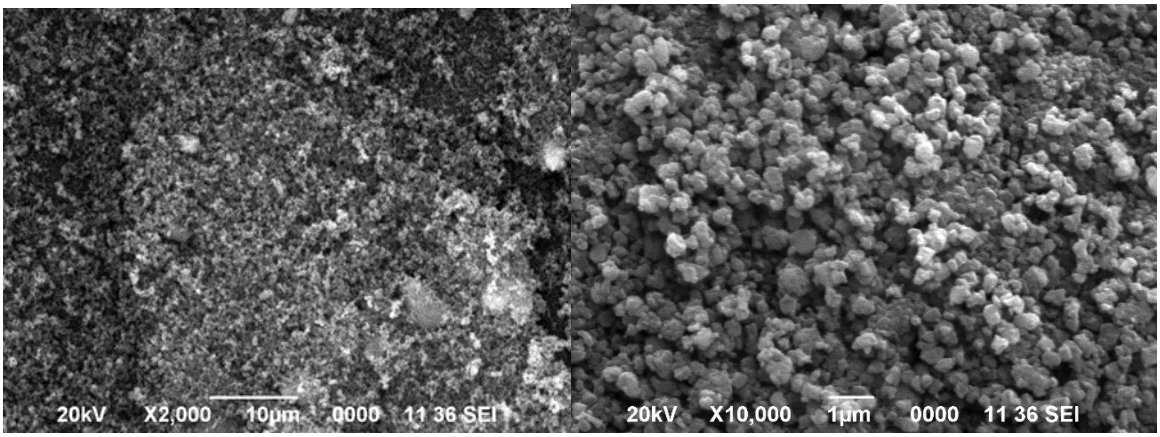

(C)

Fig. 4.25: SEM images of (A) HZSM-5, (B) Co/ZSM-5 and (C) Ni/ZSM-5

SEM was used at different magnifications (from 2000x to 10000x) to analyse the morphology of catalysts as shown in **Fig. 4.25 (A)-(C)**, which depicted the even surface of the original HZSM-5 catalyst, which slightly changes upon introduction of metals. **Fig. 4.25 (B) & (C)** depict that the metal oxides observed as agglomerates, resulting from the integration of the respective metal oxide and HZSM-5 particles. This observation indicates the effective metal ion dispersion on the support surface. However, the microstructure of HZSM-5 was retained even after metal impregnation.

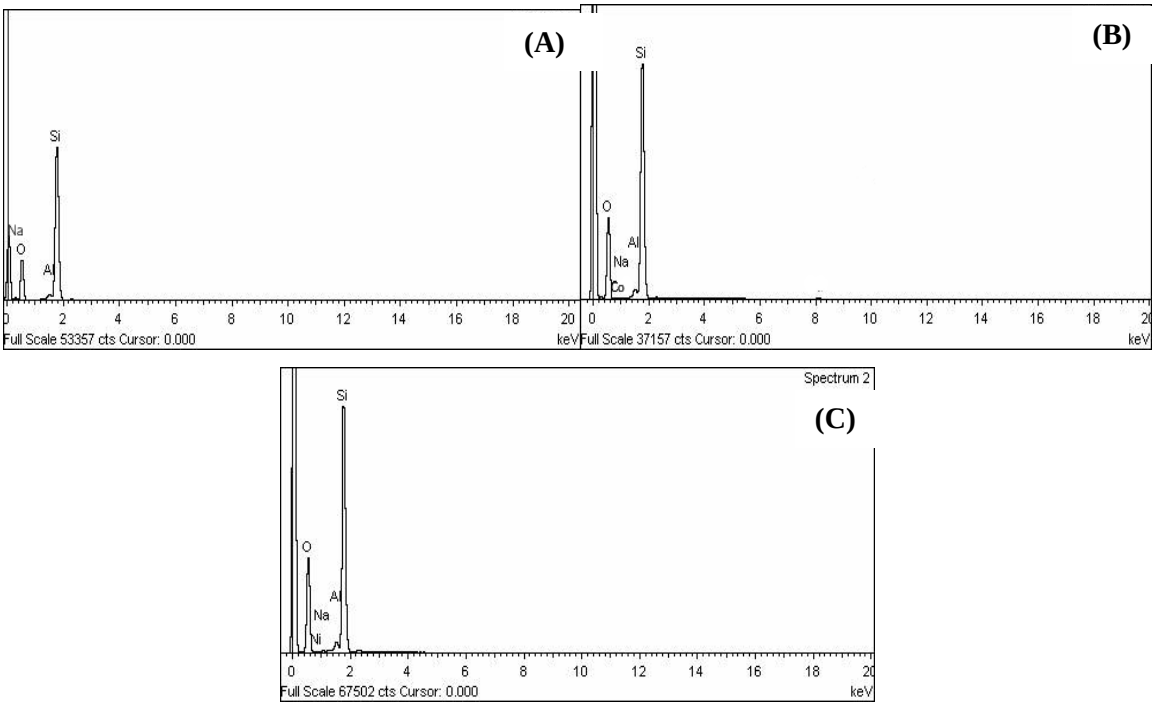

Fig. 4.26: EDX analysis of (A)HZSM-5, (B) Co/ZSM-5 and (C) Ni/ZSM-5

Fig. 4.26 displays the EDX graphs and **Table 4.14** depicts the metal content in each HZSM-5 catalyst. The measured metal loading on the impregnated catalysts was lower than the intended loading (1 wt.%). This discrepancy may be due to partial loss of the salt solution during the laboratory impregnation process, possibly caused by the equipment limitations [16].

Table 4.14: Impregnated metal content in M/ZSM-5 catalysts as per the EDX analysis

Catalysts	Co (%)	Ni (%)
Co/ZSM-5	0.93	-
Ni/ZSM-5	-	0.73

4D.2.3 Surface Analysis

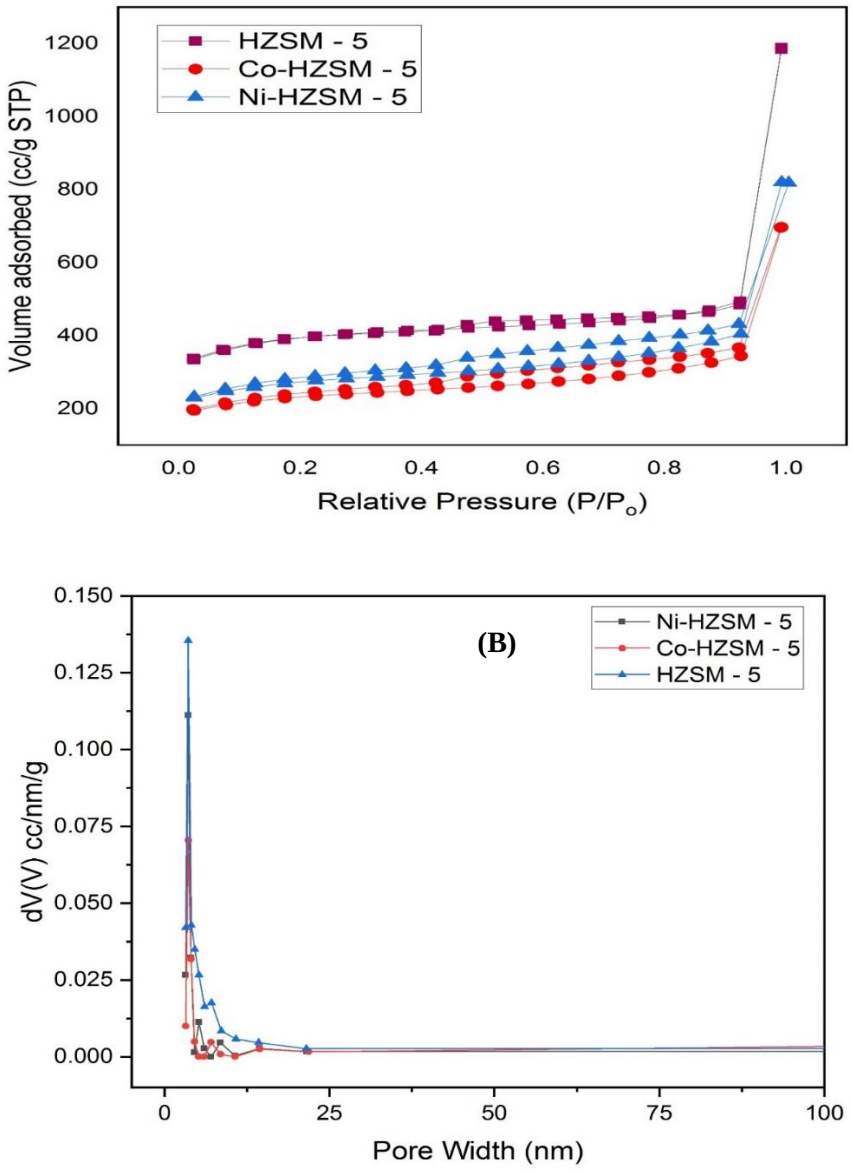

Fig.4.27: (A) N_2 adsorption-desorption isotherm of different catalysts, and(B) BJH Pore distribution

According per Brauner et al. [2] and IUPAC classifications, Adsorption isotherm curves of HZSM-5 and metal-modified HSZM 5 can be categorized as Type I isotherms with an H_3 hysteresis loop (**Fig. 4.27**), characteristics of microporous solids. Upon introduction of metal content, the shape of the adsorption-desorption isotherms changed in contrast to the HZSM-5 catalyst in its original, unaltered state. The modification of HZSM-5 likely has a minor impact on the pore shapes of the HZSM-5. The parent HZSM-5 exhibited a Type I isotherm with an H_3 hysteresis loop at high relative pressure (P/P_o). However, after metal addition, N_2 adsorption decreased as the relative pressure (P/P_o) increased. **Table 4.15** illustrates that Brunauer-Emmett-Teller (BET) and Barrett-Joyner-Halenda (BJH) surface areas of catalysts were slightly different. The BET surface area pertains to the measurement of multilayer coverage, whereas the BJH surface area relates to the surface areas of mesopores and small macropores. Furthermore, the introduction of metal impregnation into HZSM-5 leads to alterations in both BET and BJH surface areas, as well as changes in pore volume.

Table 4.15: Surface area (BET and BJH) and Pore volume for different catalysts

Sample	BET surface area	BJH Surface Area	Pore Volume
HZSM 5	329.931 m^2/g	353.086 m^2/g	0.454 cc/g
Ni-HZSM 5	318.885 m^2/g	342.364 m^2/g	0.418 cc/g
Co-HZSM 5	295.269 m^2/g	330.855 m^2/g	0.391 cc/g

The results indicated that the original HZSM-5 exhibited the highest BET surface area, measuring 329 m^2/g as well as BJH (353.086 m^2/g) surface area. Adding Co and Ni to HZSM-5 led to a slight reduction in surface area. These alterations suggest that the metals were effectively entered into the pores of HZSM-5 [17]. The reduction in surface area after metal impregnation in HZSM-5 is due to the deposition of the metal on the external surface and could have blocked some of the micropores. Similarly, the pore volume was observed to decrease as a result of impregnation. This decrease in size can be ascribed to metal oxide deposition into the HZSM-5 pores, as confirmed through SEM analysis [18, 19].

4D.3 Fixed-Bed Pyrolytic Conversion and Products Distribution

The following conditions have been considered for the pyrolysis experiments of the samples: Temperature: 500 °C at heating rate of 40 °C/min. Different catalysts were blended with the biomass at a 1:10 ratio.

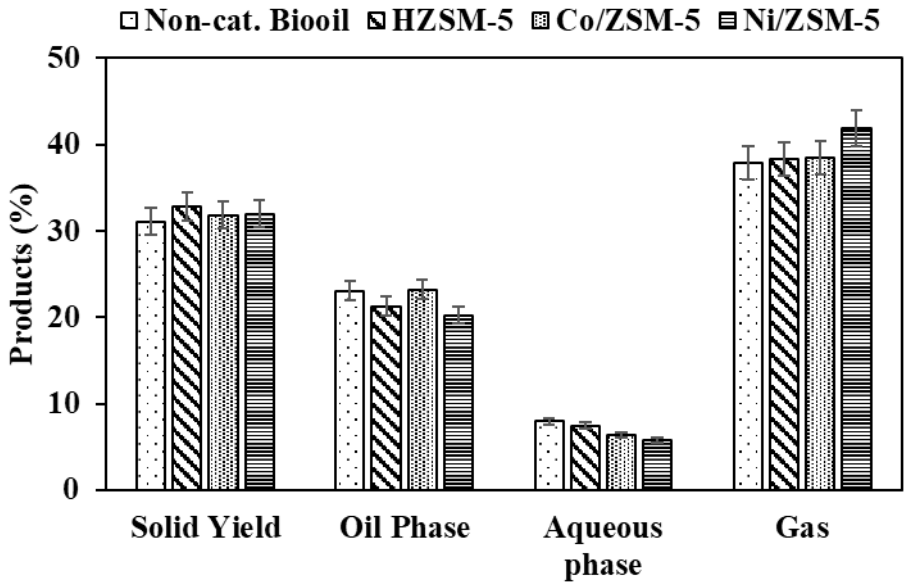

Fig. 4.28: Product distribution of the non-catalytic and catalytic pyrolysis process

The product distributions are shown in **Fig 4.28** as listed in the **Table 4.16.** Catalysts showed a noteworthy influence on biomass pyrolysis by altering product yield. All the catalyst behaves differently during pyrolysis. On using the catalysts, amounts of liquid product decreased compared to non-catalytic pyrolysis.

Nonetheless, use of cobalt-doped catalyst resulted in the reduction of the aqueous phase and surge in the organic phase (23.24±0.03%) compared to unmodified ZSM-5 (23.07±0.17%). All the catalyst's use in the pyrolysis process results in lower production of the aqueous phase of bio-oil, and among these, use of Ni-doped ZSM-5 catalysts resulted in the lowest production of aqueous phase (5.85±0.06%) as well as the lowest organic phase (20.27±0.22 %) bio-oil production, however, the gas yield was the highest (41.9±0.15%). Higher gas yield may be attributed to an increase in hydrogen yield as reported by Iliopoulou et al. [20]. On using metal into ZSM-5 the decrease in the aqueous fraction may be due to consumption of water in catalytic reforming reactions [21].

Solid yield for biomass pyrolysis also increases with the use of catalysts from 31.11±0.20 % to 32.88±0.05 %. This could be attributed to the added deposition of coke

materials in the catalytic sample. In a more detailed explanation, the volatiles released were likely to be exposed to active acid sites on the catalyst, leading to their repeated polymerization and the formation of coke within the pores and external surface of the catalyst, which potentially obstruct the diffusion route for volatiles, impeding their reaction in the pore channel. This obstruction ultimately resulted in a faster catalyst deactivation. Thus, the yield of solids is higher for all catalysts.

Table 4.16: Product distribution of the pyrolysis process

	Products	No-catalyst	HZSM-5	Co/ZSM-5	Ni/ZSM-5
	Solid yield (%)	31.11±0.20	32.88±0.05	31.85±0.03	31.98±0.05
Liquid Product	**Oil phase (%)**	23.07±0.17	21.29±0.05	23.24±0.03	20.27±0.22
	Aqueous phase (%)	7.95±0.05	7.47±0.07	6.38±0.05	5.85±0.06
	Gas yield (%)	37.87±0.08	38.36±0.03	38.53±0.08	41.9±0.15

4D.3.1 Bio-oil Characterization

4D.3.1.1 Physicochemical characterization

Table 4.17: Characteristics of non-catalytic and catalytic bio-oil

Properties	Non-catalytic	HZSM-5	Co/ZSM-5	Ni/ZSM-5
O	42.85	35.61	34.51	34.09
H	7.25	8.32	8.57	8.89
N	1.15	0.83	0.12	0.09
C	48.75	55.24	56.80	56.93
pH	3.87	4.08	4.17	4.02
HHV (MJ/kg)	23.84	27.65	28.68	28.76
Viscosity (cP)	86.1	80.5	79.6	79.5
Density @ 15 °C (kg/m^3)	1008	956	940	936

Table 4.17 lists elemental analyses, calorific value (CV), and several other bio-oil properties acquired from non-catalytic and catalytic pyrolysis. On blending the catalysts with TD in pyrolysis, the oxygen content decreased to 35.61%, 34.56%, and 34.09% for HZSM-5, Co/ZSM-5, and Ni/ZSM-5, respectively in comparison to non-catalytic pyrolysis bio-oil (42.85%). This was due to the deoxygenation reactions on the catalyst surface. Concurrently, the carbon content increased from 48.75% (in non-catalytic bio-oil) to approximately 56.93% in Ni/ZSM-5 catalysed bio-oil. While catalytic pyrolysis oil exhibited a increase in hydrogen content due to decarboxylation and dehydration processes [31], it remained relatively unchanged among all catalyst driven bio-oils. Furthermore, higher calorific values of catalytic bio-oils exhibited a significant surge in carbon content, signifying their superiority. The high acidity of pyrolytic oil negatively affects its heating value and can lead to corrosion in storage vessels and fuel liners [3]. However, the acidity of catalytic oil improves with the rise in pH (pH up to 4.17), in comparison to non-catalytic oil (pH=3.87).

Characterization of non-catalytic pyrolytic oil confirmed its higher viscosity (86.1 cP) and density (1008 kg/m^3). The presence of strongly oxygenated compounds mostly causes the high viscosity of non-catalytic bio-oil. These compounds substantially impact the bio-oil's viscosity by causing it to crystallize over time at ambient temperature. Further, the unsaturated oxygenate compounds' availability also adversely affects its stability and engine performance. These properties render bio-oil as an unsuitable transportation fuel [3]. However, the utilization of catalytic pyrolysis reduces the viscosity and density of bio-oil which is due to the facilitation of cracking reactions as well as enhanced deoxygenation.

4D.3.1.2 NMR analysis of non-catalytic and catalytic pyrolytic oil

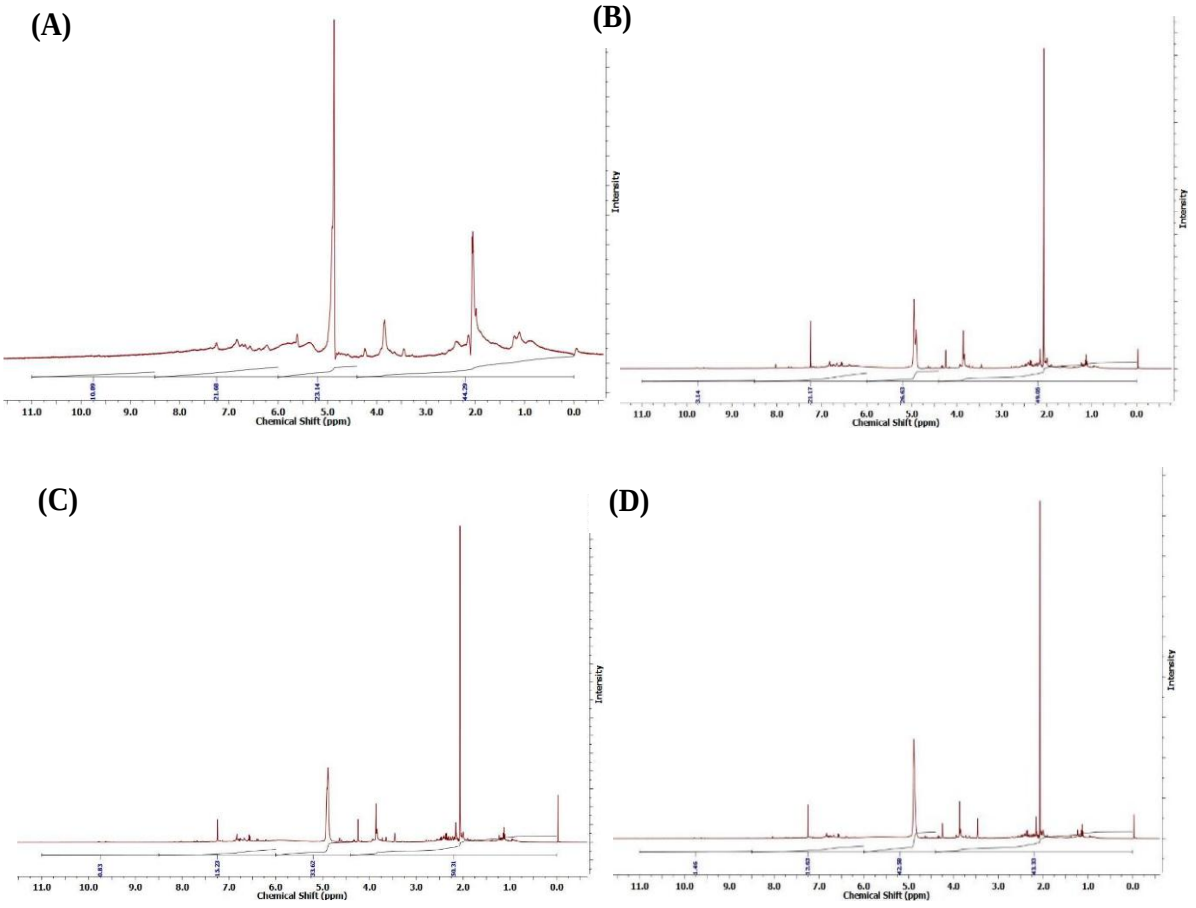

Fig. 4.29: ^{1}H-NMR analysis of different bio-oil: (A) non-catalytic, (B) HZSM-5, (C) Co/ZSM-5, and (D) Ni/ZSM-5

Fig 4.29 illustrates ^{1}H-NMR analysis of non-catalytic and catalytic bio-oils, and **Table 4.18** includes the compounds. Proton NMR study suggests the catalytic bio-oils comprise of higher aromatics and phenols than non-catalytic bio-oil (Ni/ZSM-5 > Co/ZSM-5>HZSM-5> non-catalytic bio-oil). More aliphatic compounds were observed for catalytic bio-oils than the non-catalytic one, and the order of their availability is as follows: HZSM-5 exhibits the highest performance in terms of presence of more aliphatic compounds, followed by Co/ZSM-5, Ni/ZSM-5, and lastly, the non-catalytic bio-oil. Nevertheless, the alcohols, ethers, and carbohydrates percentages decreased in catalytic pyrolysis oils than in non-catalytic oil. This reduction may be ascribed to the major occurrence of dehydration and deoxygenation reactions in catalytic pyrolysis.

Table 4.18: Percentage of H based on ^{1}H-NMR analysis of bio-oil

Chemical Shift range (ppm)	Proton assignments	% Distribution			
		Non-catalytic	HZSM-5	Co/ZSM-5	Ni/ZSM-5
0-4.4	Aliphatics	33.33	50.31	49.05	44.29
4.4-6.0	Alcohols, Ethers, Carbohydrates	42.58	33.62	26.63	23.14
6-8.5	Aromatics, Olefins, Phenols	12.63	15.23	21.17	21.68
8.5-11.0	Aldehydes, Ketones, Acids	11.46	0.83	3.14	10.89

4D.3.1.3 GC-MS

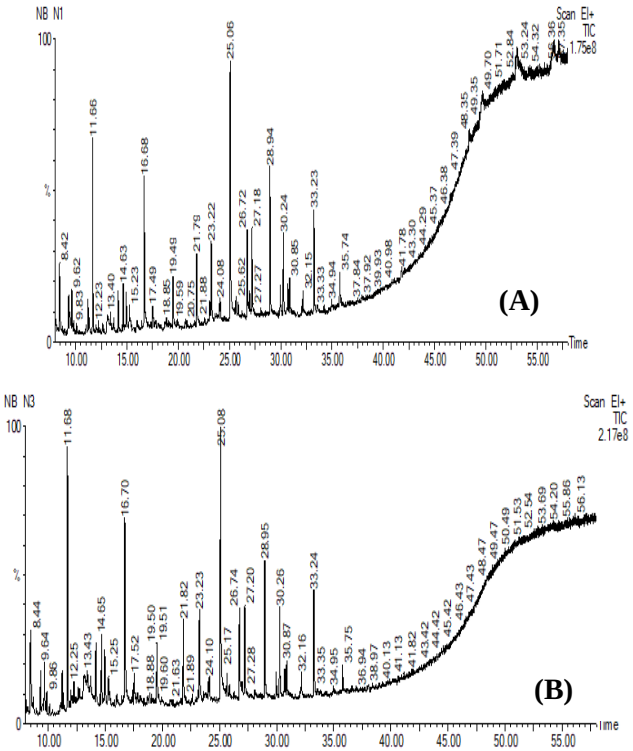

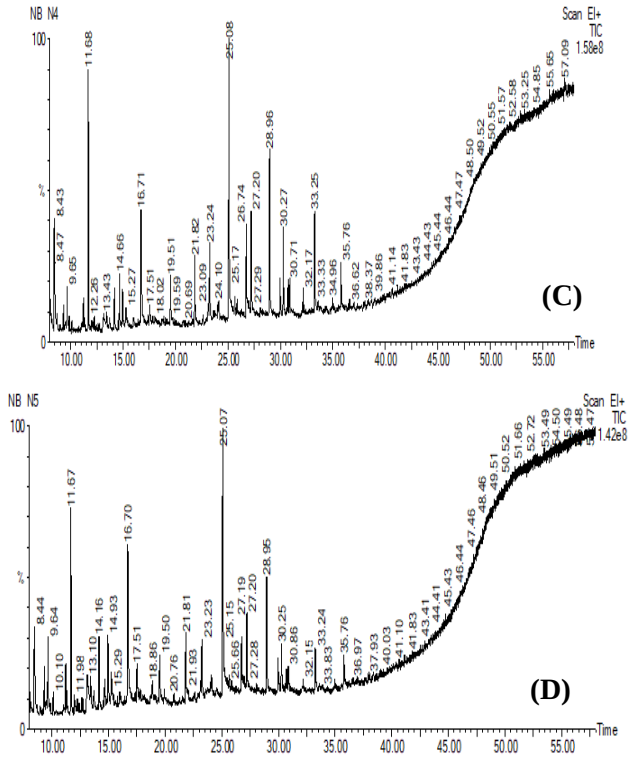

Fig. 4.30: Total ion chromatogram of different bio-oil: (A) Non-catalytic (B) HZSM-5 (C) Co/ZSM-5 and (D) Ni/ZSM-5

GC-MS was utilized to conduct a comprehensive examination of bio-oil, encompassing both quantitative and qualitative analyses. The GC-MS thermogram was compared to the National Institute of Standards and Technology (NIST) database. The pyrolytic oils consists of a complex mixture containing various organic compounds, including poly-aromatics, mono-aromatics, nitrogenates constituents, oxygenates, heterocyclic, and aliphatic [3]. These compounds as displayed in the total ion chromatogram **(Fig. 4.30)** present in non-catalytic and catalytic oils are illustrated in **Fig 4.31**, whereas major compounds, representing more than 0.5% of peak area, are listed in the *Appendices (Table S5-S7)*. The identified compounds were then categorized. This study observed that both catalytic and non-catalytic bio-oils mostly consist of aliphatic and aromatic hydrocarbons, phenols, other alcohols, ethers, esters, and ketones, among others. The identified compounds had carbon distributions within C_5–C_{16}.

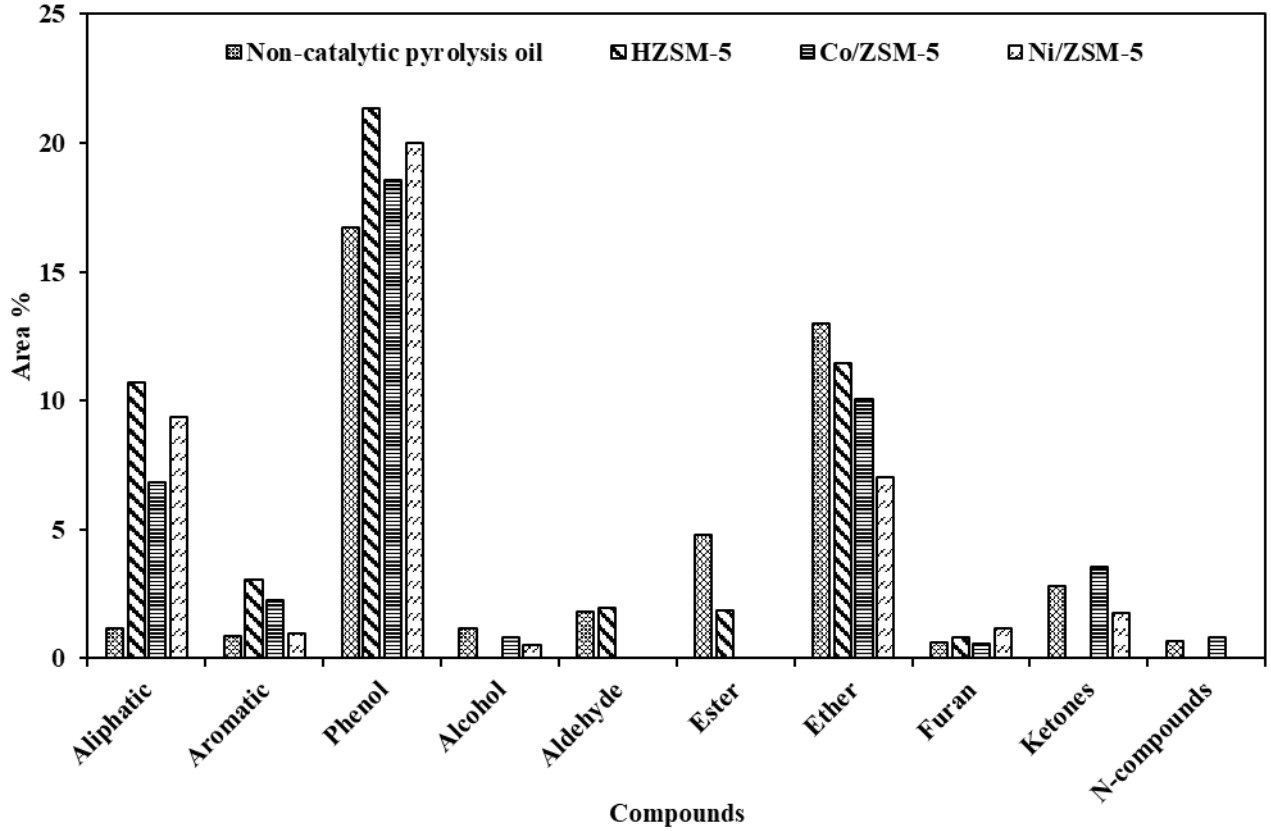

Fig. 4.31: Effect of catalyst on different types of compounds according to GC-MS data

Fig. 31 suggests that non-catalytic pyrolytic oil primarily composed of 16.71% phenols, which include various phenol derivatives like methoxy phenols and alkylphenols (e.g., methyl phenols, and propyl phenols). It also contains 2% hydrocarbons (aliphatic and aromatic), a small number of nitrogen compounds, 4.80% esters, 3% ketones, and 12.98% ethers. The phenolic compounds in non-catalytic pyrolytic oil have diverse uses like antiseptics, dye synthesis, and aspirin production [3]. Additionally, pyrolytic oil is a potential candidate for direct utilization in boilers for electricity and heat production. However, the utilization of bio-oil as transportation fuel requires blending with diesel, and appropriate upgrading methods like catalytic cracking may be required.

As per GC-MS analysis, catalyst utilization enhanced the total hydrocarbon content while significantly reducing the percentage of oxygenated compounds in terms of ethers, and esters in catalytic pyrolytic oil. This effect was attributed to decarboxylation and dehydration reactions [3]. Aromatic and aliphatic hydrocarbons, as well as alcohols, are termed as ideal biofuel- components. Phenols and furans are also regarded as important chemicals for various end-uses [22]. This investigation revealed that catalytic pyrolysis oil

could be a more ideal biofuel product and a source of value-added chemicals compared to non-catalytic pyrolysis oil. Carbonyl compounds, including ketones, aldehydes, esters, and ethers are undesirable due to their corrosiveness, instability, and reduction of bio-oil's heating value [7] and GC-MS analysis confirmed that catalytic pyrolysis oil had fewer undesirable products than non-catalytic pyrolysis oil. These findings align with the increased calorific value observed in catalytic pyrolysis oils. Additionally, **Fig. 4.31** illustrates that catalytic pyrolysis oils contain a greater percentage of aromatic compounds than non-catalytic pyrolysis oils. Upgraded bio-oil offers significant benefits due to the presence of aromatic hydrocarbons. Drawing upon GC-MS results, the catalytic oil showed potential as a suitable substitute for traditional fuels and as a source for extraction of valuable compounds.

4D.4 TG and DTG Analysis

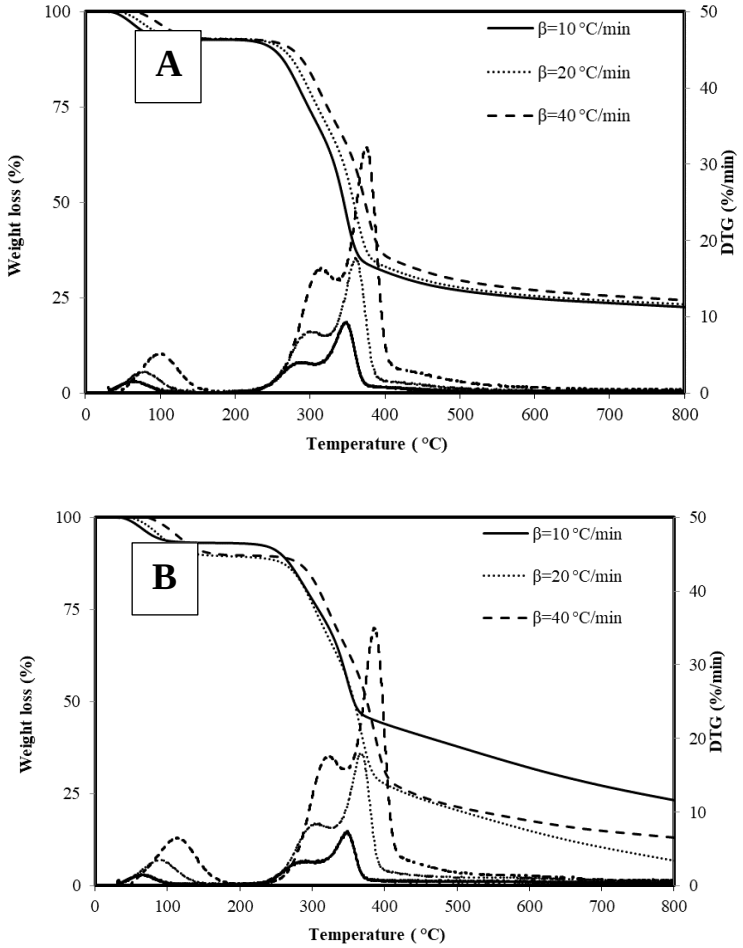

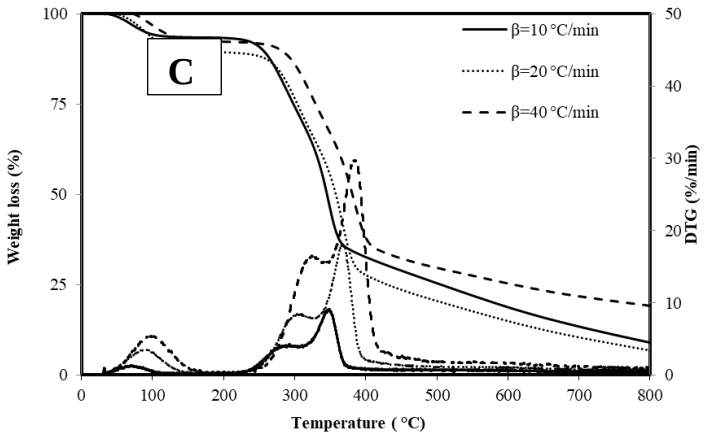

Fig.4.32 TG and DTG diagram of biomass samples containing (A) HZSM-5, (B) Co/ZSM-5, and (C) Ni/ZSM-5

Fig. 4.32 (A-C) presents the TG and DTG profiles of the catalyst blended TD biomass, revealing the predominant mass reduction in biomass occurring between the temperature range of 218 to 420 °C when subjected to a heating rate of 10°C/min. Within this temperature range, cellulose, hemicellulose, and a portion of lignin undergo decomposition. DTG analysis reveals a prominent peak for all samples within the temperature range of 340–385 °C, regardless of the heating rate employed. This peak signifies the maximum decomposition rate and likely corresponds to the primary decomposition of cellulose. Additionally, a shoulder observed between 280–330 °C is attributed to the decomposition of hemicellulose. **Table 4.19** represents the thermal analysis parameters of various catalytic and non-catalytic samples for active pyrolysis zones at heating rates of 10, 20, and 40 °C/min. For all the samples, there is an increase in onset, offset, and maximum temperatures as the heating rate goes up. The DTG_{max} also shows an increasing trend. As observed in Chapter 4(C), non-catalytic biomass exhibits lower onset and offset temperatures compared to catalytic samples. This difference may arise from the catalyst inhibiting or slowing down specific reactions within the biomass, impeding the thermal degradation process and resulting in higher onset temperatures for catalytic samples. Additionally, the catalyst may obstruct reactive sites in the biomass, due to its mechanical mixing, thereby rendering the biomass less prone to thermal degradation at lower temperatures.

Table 4.19: Thermal analysis parameters of various catalyst blended samples for active pyrolysis zone at different heating rates

	Heating Rate (°C/min)	Onset temp., T_i (°C)	Offset temp., T_f (°C)	Maximum temp., T_m (°C)	DTG_{max} (%/min)
HZSM-5	10	218	385	346	9.6
	20	230	400	359.3	17.94
	40	240	420	374.86	32.4
Co/ZSM-5	10	243	371	346.98	7.56
	20	250	395	364.07	18.06
	40	260	420	385.4	35.34
Ni/ZSM-5	10	230	366	346.28	9.18
	20	250	394	364.07	18.06
	40	270	415	382.2	30

4D.5 Evaluations of Kinetic and Thermodynamic Parameters

4D.5.1 Kinetic Parameters

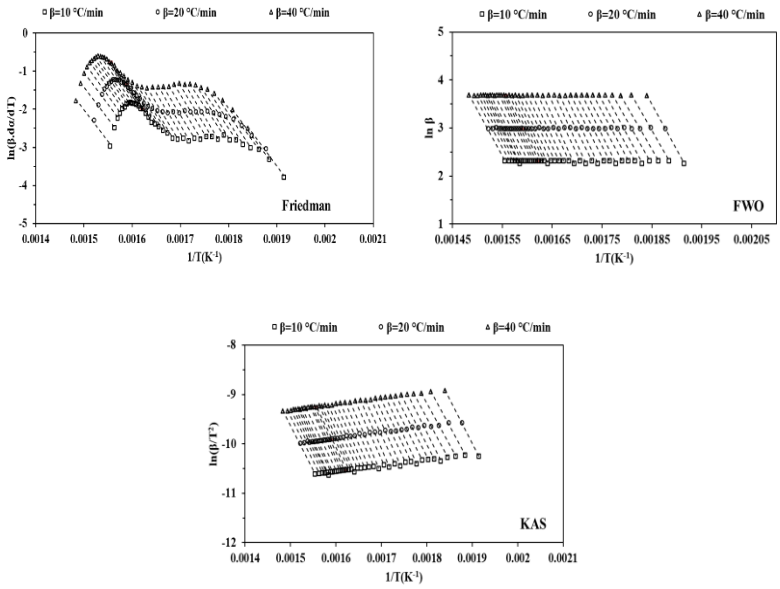

(A)

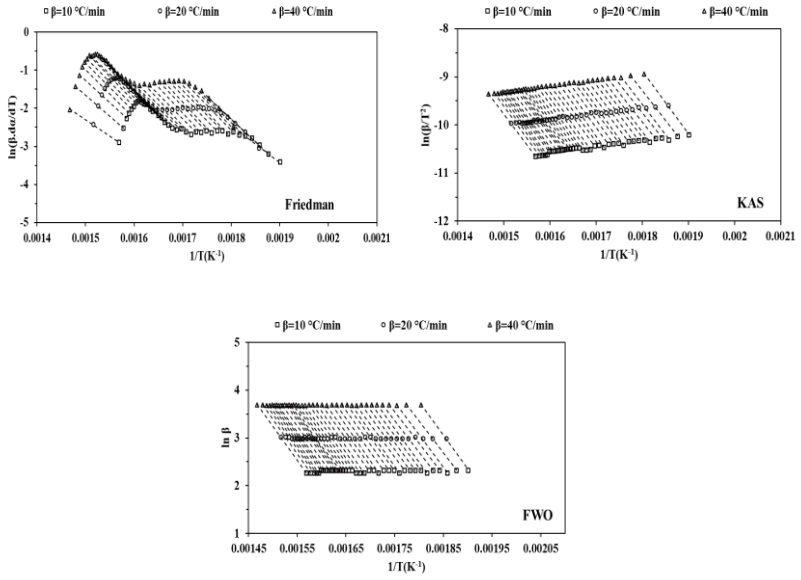

(B)

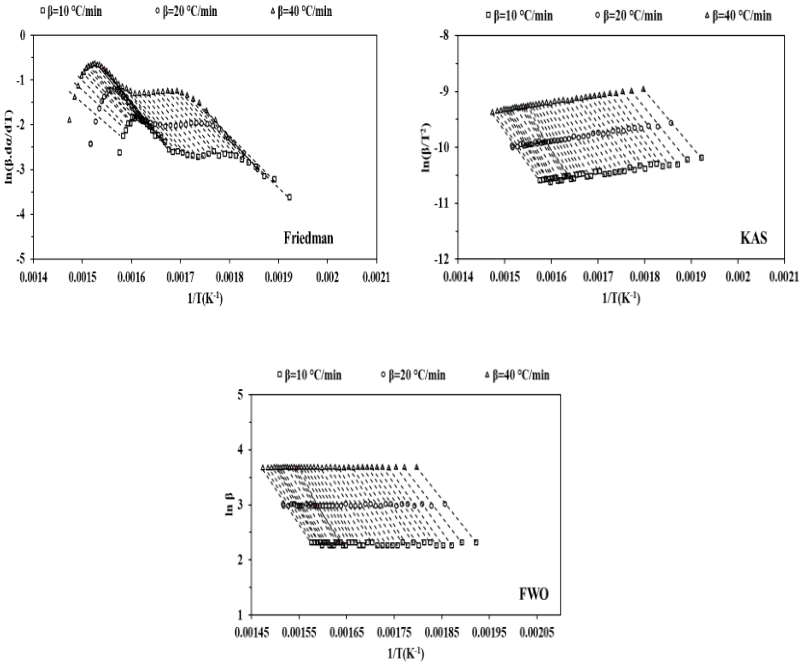

(C)

Fig.4.33: Friedman, FWO, and KAS plots for different samples: (B) TD+ ZSM-5 (C) TD+ Co/ZSM-5 (D) TD+ Ni/ZSM-5

Kinetic parameters of all the samples were evaluated within the active pyrolysis zone i.e., 215- 420°C for catalytic samples and 190-370 °C for non-catalytic samples. **Fig.**

4.33 displays the Friedman, KAS, and FWO plots for the biomass specimens falling within the fractional conversion interval from 0.025 to 0.900, with an incremental interval of 0.025, specifically focusing on the active pyrolysis zone.

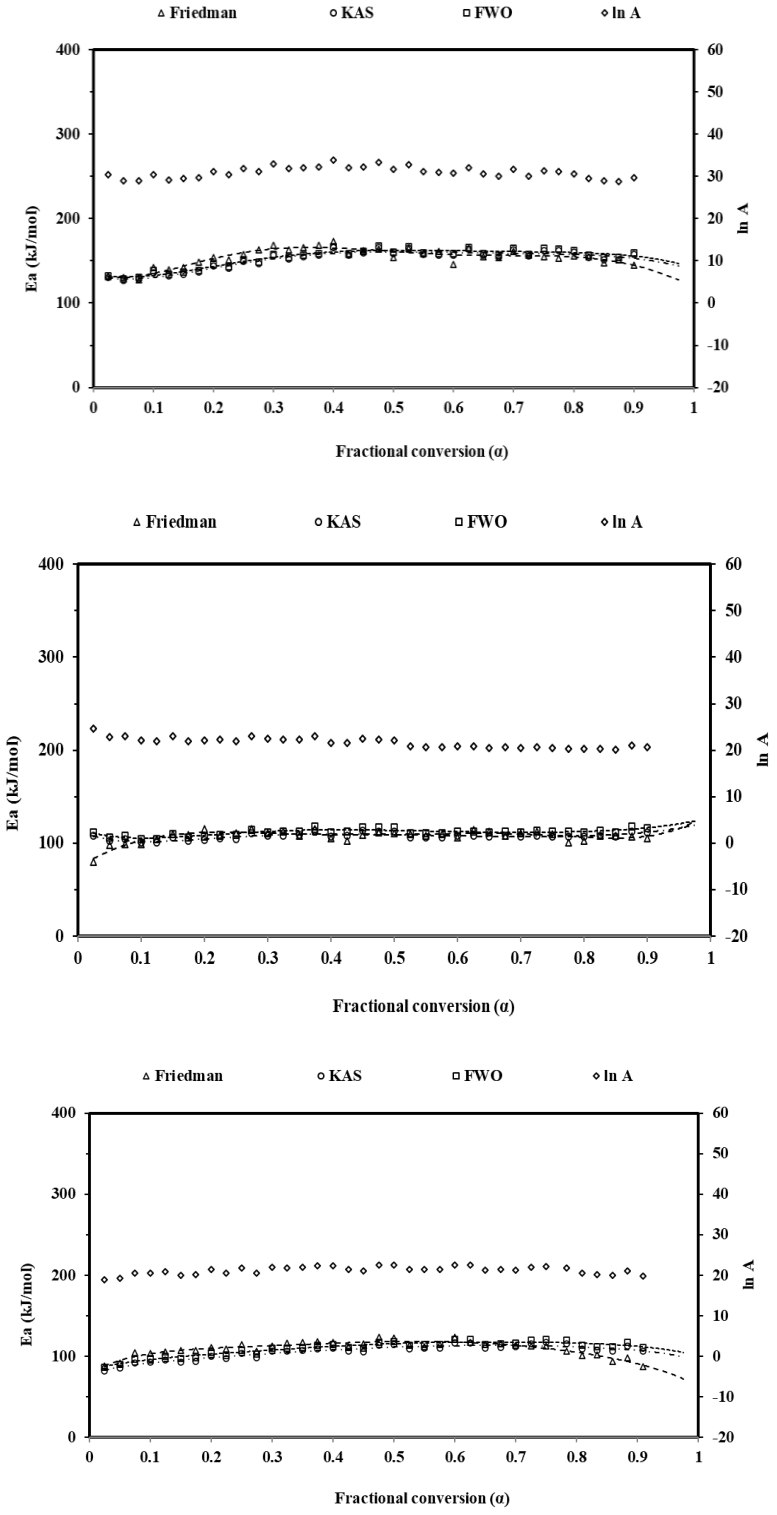

Fig.4.34: Kinetic parameters (E_α and lnA_α) for single-step pyrolysis model of biomass samples containing: (a) HZSM-5 (b) Co/ZSM-5 (c) Ni/ZSM-5

Fig. 4.34 presents the apparent activation energies (E_α) derived from linear kinetic plots using KAS, FWO, and FRD techniques. The similarities observed in the values of $E_\alpha(\alpha)$ across the different samples using all the mentioned methods indicate the precision and consistency of the presented results. In the beginning, there is a subtle rise in E_α, possibly attributed to the occurrence of several heterogeneous devolatilization reactions with an endothermic nature. Lower E_α witnessed for M/ZSM-5 samples in comparison to non-catalytic samples (**Fig. 4.35**). It suggests that catalysts effectively reduce the activation barriers associated with bond cleavage processes.

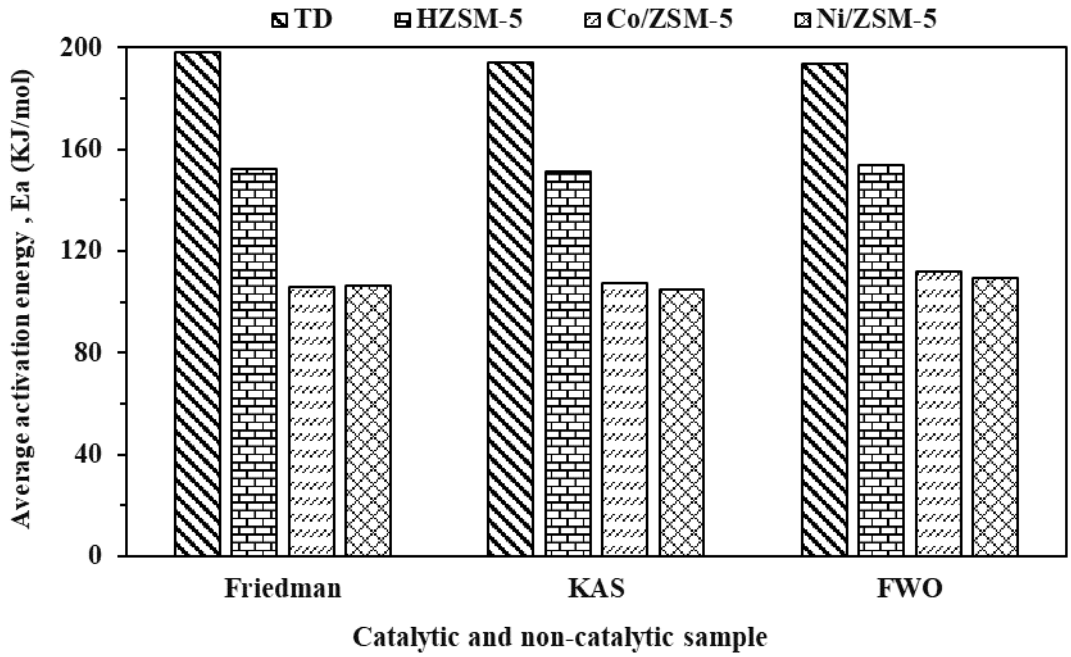

Fig.4.35: Comparison of average activation energy obtained using Friedman, KAS, and FWO methods for various catalytic and non-catalytic samples

Calculating mean values for the kinetic parameters of pyrolysis over simplifies a complex phenomenon, as it involves multiple independent parallel reactions occurring simultaneously. In the estimation of E_o, any E_α values that exceeded 30% of the average apparent E_a were excluded [12]. Likewise, E_α values associated with R^2 values below 0.900 were excluded from the analysis. The E_o for TD by FRD, KAS, and FWO techniques are 198.13, 195.54, and 196.15kJ/mol respectively. The utilization of catalysts leads to a significant reduction in the activation energy required for biomass devolatilization. **Table 26** and **Fig 4.35** revealed that among the catalytic samples, HZSM-5 exhibits the highest average E_α values, followed by Ni/ZSM-5 and Co/ZSM-5. The estimated E_o for Co/ZSM-

5 catalysts, as determined by KAS, FWO, and FRD methods, are 107.31, 111.58, and 107.36 kJ/mol, respectively. In the case of Ni/ZSM-5 catalysts, the corresponding activation energies are 105.42, 109.75, and 109.50 kJ/mol, respectively. As data obtained from the Miura-Maki method, mean Arrhenius constants of Co/ZSM-5, and Ni/ZSM-5 are respectively 4.68×10^{9} and 2.3×10^{9} min^{-1} and are significantly lower than that of TD (9.51×10^{22} min^{-1}). A similar trend of decreasing order of the average Arrhenius constant for catalytic samples using Friedman (FRD), FWO, and KAS methods is shown in **Table 4.20.** However, due to the more informative nature of Friedman plots, it will be considered for further discussion. A plot of lnA_{α} against α for the FRD method is presented in **Fig 4.36**. It is observed that use of catalysts results in a lower Arrhenius constant compared to non-catalytic samples.

Table 4.20: Kinetic parameters

Parameters	**Methods**	**TD**	**TD+HZSM-5**	**TD+ Co/ZSM-5**	**TD+Ni/ZSM-5**
Ea (kJ/mol)	**Friedman**	198.13	154.11	107.36	109.50
	FWO	196.15	151.64	107.32	105.42
	KAS	195.54	153.64	111.58	109.75
Arrhenius constant, A (min^{-1})	**Miura-Maki**	9.51×10^{22}	6.11×10^{13}	4.68×10^{9}	2.3×10^{9}
	Friedman	1.77×10^{20}	7.02×10^{13}	1.43×10^{9}	4.93×10^{8}
	FWO	4.10×10^{18}	3.63×10^{13}	1.32×10^{9}	2.37×10^{8}
	KAS	5.25×10^{18}	2.47×10^{13}	4×10^{8}	7.6×10^{8}

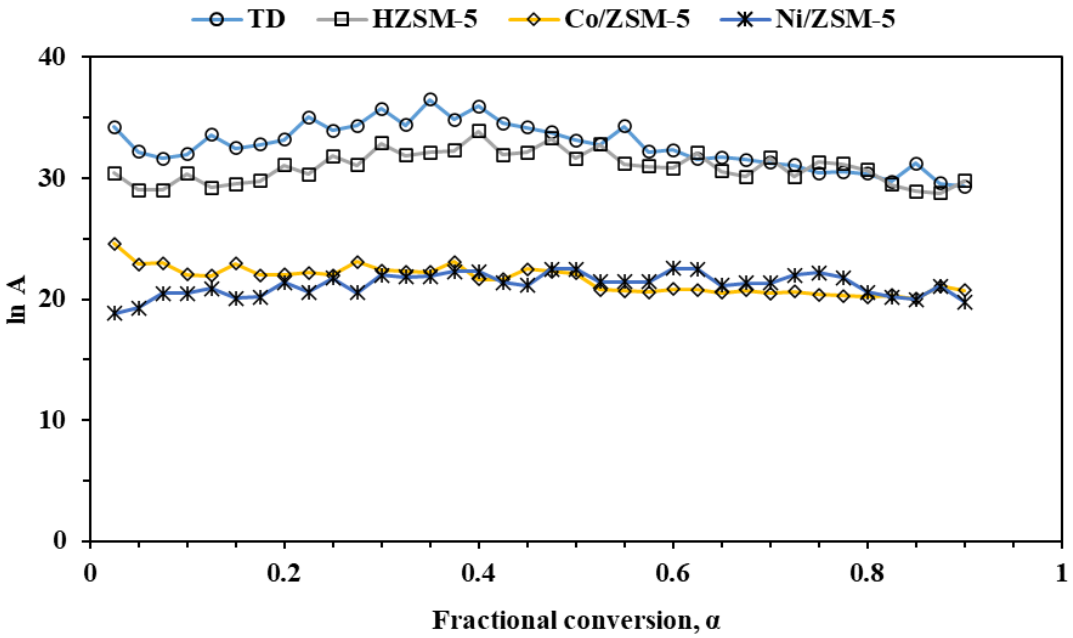

Fig. 4.36: Plot of *lnA* as a function of *α* for catalytic and non-catalytic samples for Friedman method

4D.5.2 Master Plot Method

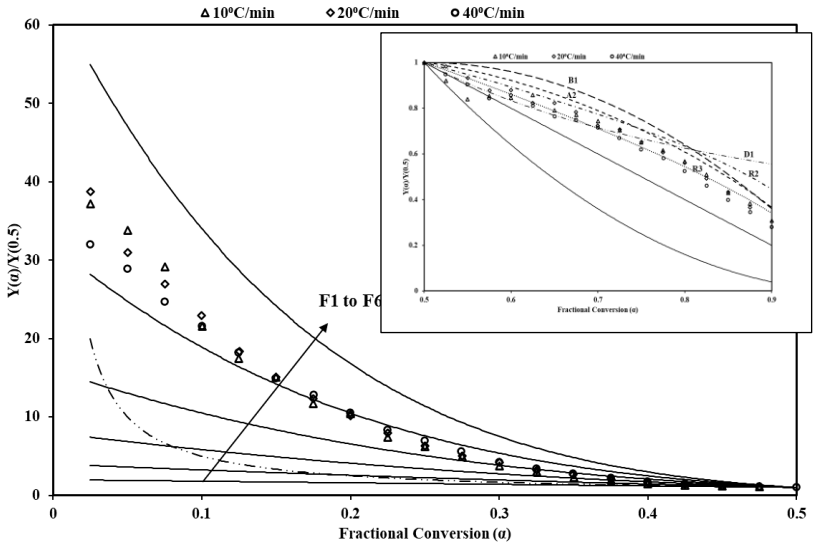

(A)

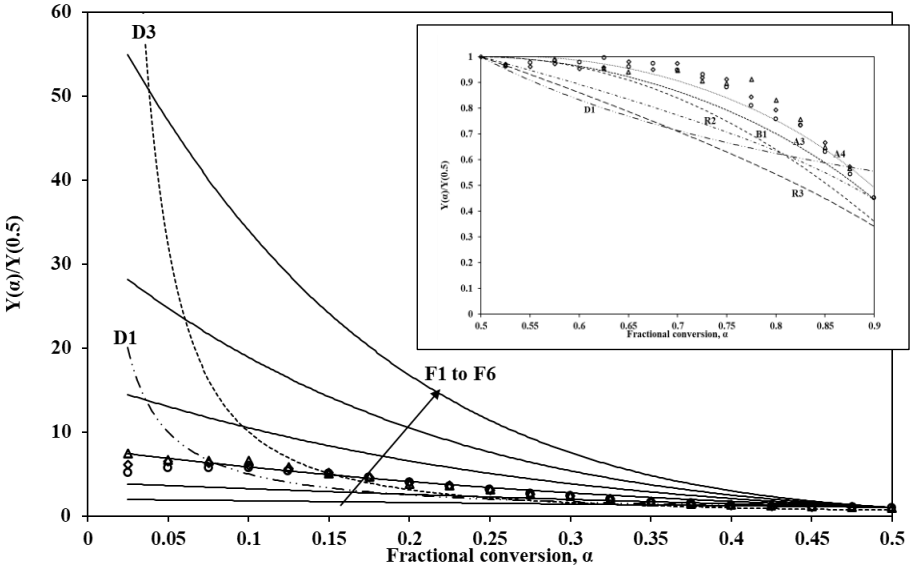

(B)

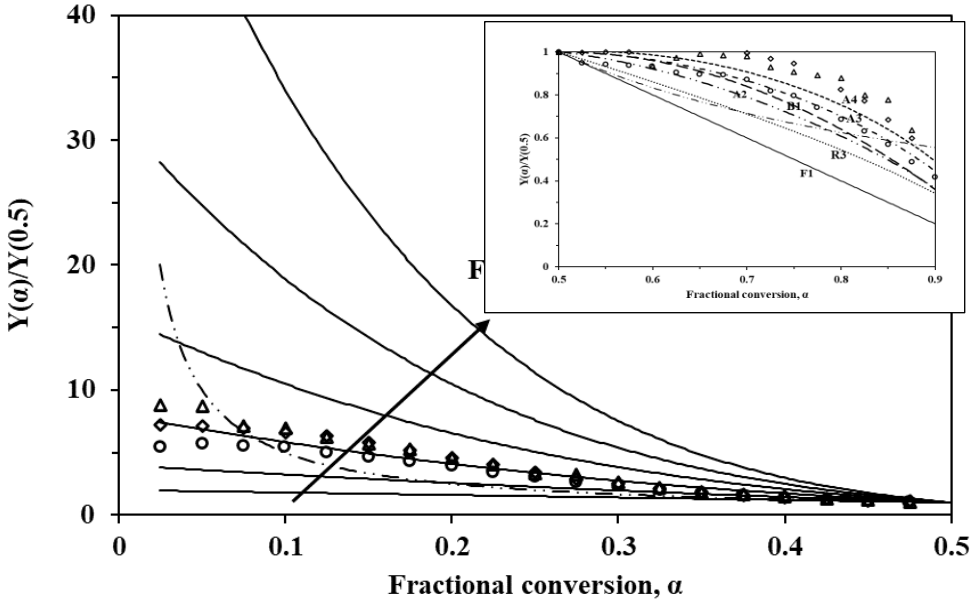

(C)

Fig.4.37: *Y(α)/Y(0.5)* master plots for single-step pyrolysis of biomass samples containing: (A) HZSM-5 (B) Co/ZSM-5 and (C) Ni/ZSM-5

Fig. 4.37 presents the *Y(α)* master plots of catalytic pyrolysis. These figures illustrate the theoretical mechanisms that align most closely with the experimental results. In order to depict a clear view between the theoretical and experimental mechanisms, figures are broken up into two parts containing fractional conversion ranges of 0-0.5 and 0.5-0.9. To identify the most appropriate mechanism, the analysis considered factors such as root mean square errors and the level of resemblance between the experimental curves and the theoretical model curves. As mentioned in **Chapter 4C**, the degradation of TD adheres to order-based models within the range of α = 0.025–0.725 and subsequently transitions to the D3 model for α = 0.725-0.900. Furthermore, the gradual transition from reaction order models (F4 to F2) suggests that biomass degradation depends upon the concentrations of remaining reactants [24]. The observation of a high reaction order for biomass in the initial stages can be ascribed to hemicellulose degradation. Hemicellulose typically undergoes decomposition with a high apparent reaction order [25]. During the early stages, when reactant concentrations are relatively high, there is a greater likelihood of combining a relatively larger number of reacting species. The gradual decrease in reaction order is, as a result, attributable to the decreasing concentrations of reacting species as the conversion level increases. The complication of the reaction is significantly elevated during the early devolatilization stage. This heightened complexity arises from the simultaneous cellulose and hemicellulose decomposition, within a short time frame, leading to the formation of several reactive species. The degradation of biomass during the initial stages results in the formation of highly porous biochar. This porous structure facilitates the diffusion of gaseous products. Hence, as the TD pyrolysis progresses, the D3 model emerges as the slowest process and begins to govern the overall conversion mechanism. Application of HZSM-5 on TD pyrolysis follows the order-based model within the α range of 0.025 to 0.525, transitioning to the geometrical contraction and nucleation model at the later stages. On application of Co/ZSM-5 catalyst on TD pyrolysis, the mechanism changes into the order-based model (F3) followed by diffusion (D3) model and nucleation model. Again, for Ni/ZSM-5 catalyst the pyrolysis mechanism follows the diffusion (D2 and D3) followed by nucleation model (A4 and A3). Thus, from the mechanisms it can be observed that the influence of catalysts on biomass pyrolysis is intricate and varied. Catalysts demonstrate the ability to impact reaction pathways, improve mass transfer, and contribute to the emergence of new phases or structures. The transition from simpler order-based and diffusion models observed in non-catalytic samples to a more diverse range of models, encompassing nucleation and geometrical contraction models in

catalytic samples, suggests that catalysts introduce additional intricacies and pathways into the pyrolysis process.

4D.5.3 Thermodynamic Parameters

Fig. 4.38 illustrates variations in Gibbs free energy change (ΔG_α), entropy change (ΔS_α), and enthalpy change (ΔH_α) with respect to α. Positive values of ΔH_α denote biomass pyrolysis as endothermic, requiring energy to break bonds. Non-catalytic biomass pyrolysis exhibits the highest ΔH_α, signifying the greatest energy demand for the dissociation of chemical bonds in its structural components when compared to the catalyzed samples. Lower ΔH_α values observed for all catalysts mixed biomass in all conversion ranges indicate that all catalysts promote the formation of activated complexes at lower temperatures. From **Fig 4.38** it has also been noticed that ΔH_α for catalytic samples are initially increasing, which might be due to the substantial energy required to initiate bond-breaking processes. The E_α-H_α provides valuable information regarding the viability of the reaction, especially when the difference is less than 5.50 kJ/mol. A minimal barrier value encourages the formation of products from activated complexes [25].

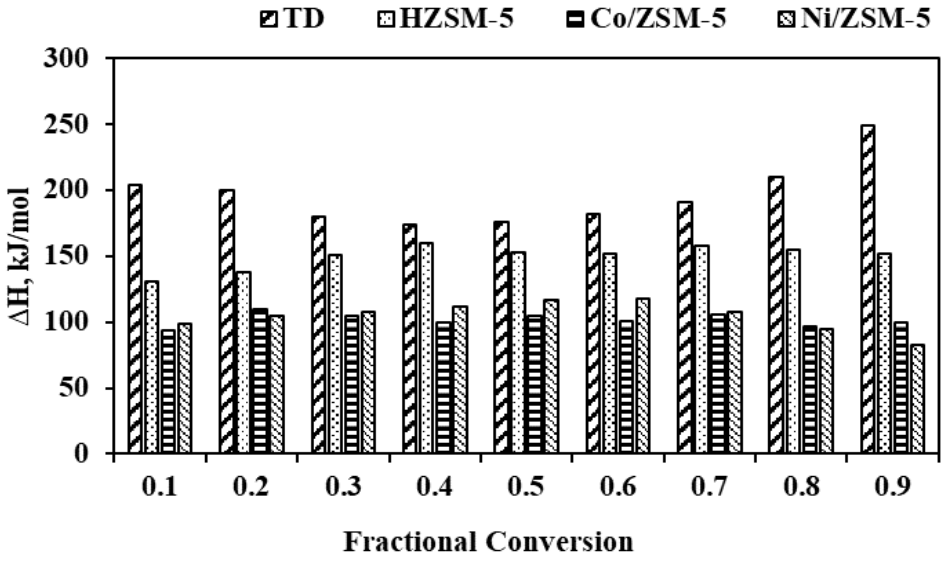

(A)

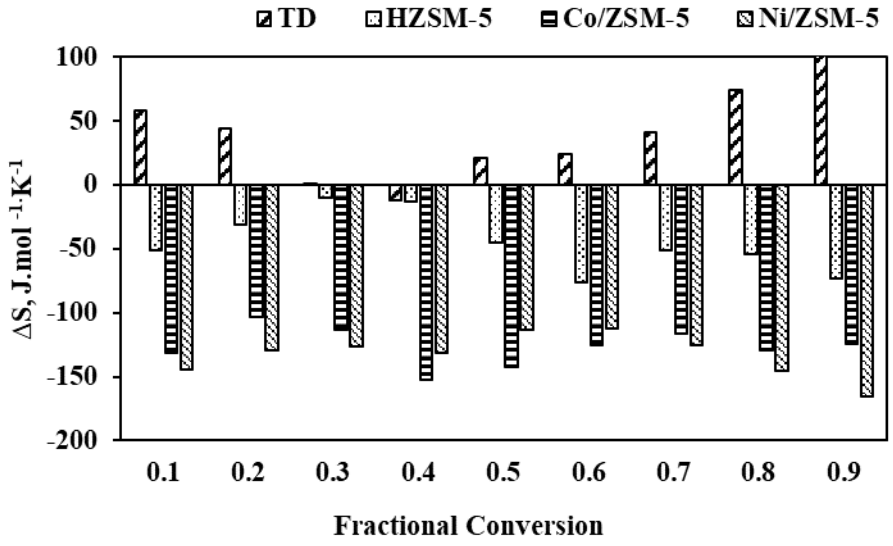

(B)

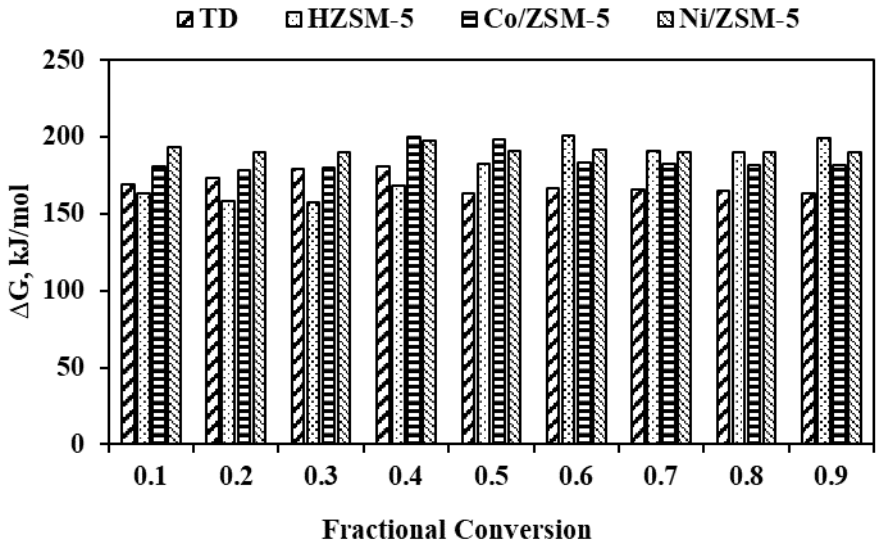

(C)

Fig. 4.38: Variations in (A) enthalpy change (ΔH_α), (B) entropy change (ΔS_α), and (C) Gibbs free energy change (ΔG_α) with respect to α

Entropy change (ΔS) offers valuable insights into the characteristics of the activated complex as well as their formation mechanism [13]. When examining non-catalytic processes within the α = 0.1–0.9 range, both negative ΔS_α (at α = 0.4) and positive ΔS_α values (excluding α = 0.4) obtained. The positive entropy change suggests a considerable degree of disorder in biomass, resulting in reduced available energy within the system for the formation of the activated complex [26]. On the other words, it can be said that the activated complex experiences a relatively weak binding, and the activation process

includes the separation of its components [27, 28]. ΔS_α for all catalyst-containing biomass is negative for all the conversion ranges, suggesting that the rate-controlling stage proceeds through an associative mechanism, in which the reactant species converge to form a more organized activated complex. The observed negative ΔS_α may be attributed to the intricate steric constraints that come into play during the development of activated complex from the reactants [29].

Positive values of ΔG_α denote the non-spontaneous nature of the solid-state reaction. Similarly, the higher ΔG_α observed for catalytic pyrolysis suggests that catalysts promote biomass devolatilization [14].

4D.6 Summary

Different catalysts affect the product distribution of the pyrolysis process differently. Further, physico-chemical characterization such as NMR, and GCMS analyses of bio-oil indicate improved properties when catalysts are employed, including reduced O and greater C content, and higher calorific values. The mean activation energy values for the non-catalytic pyrolysis were evaluated within 195.54-198.13 kJ/mol, while the catalytic pyrolysis processes involving HZSM-5 zeolite, Co/ZSM-5, and Ni/ZSM-5 were assessed in the range of 151.64-154.11 kJ/mol, 107.32-111.58 kJ/mol, and 105.42-109.75 kJ/mol, respectively, indicating that catalysts play a role in providing an alternative reaction pathway or reducing the activation energy required for specific reactions, making the overall pyrolysis process more energetically favorable. Thermodynamic analysis also supports the catalytic enhancement of biomass devolatilization. The associative mechanism is often associated with catalytic reactions where the availability of a catalyst facilitates the creation of intermediates or activated complexes, leading to faster and more controlled reactions. For catalytic pyrolysis, negative ΔS and higher ΔG values compared to ΔH implies that a significant portion of the heat energy supplied to the system is excess or surplus. Thus, the catalytic pyrolysis process becomes more exothermic than the non-catalytic pyrolysis process. This investigation offers valuable insights into ZSM-5 catalysts' pivotal role in thermo-chemical biomass conversion.

References

1. Vichaphund, S., Aht-ong, D., Sricharoenchaikul, V., and Atong, D. Production of aromatic compounds from catalytic fast pyrolysis of Jatropha residues using metal/HZSM-5 prepared by ion-exchange and impregnation methods. *Renewable energy*, *79*: 28-37, 2015.
2. Brunauer, S., Deming, L. S., Deming, W. E., and Teller, E., On a theory of the van der Waals adsorption of gases. *Journal of the American Chemical Society*, *62*(7), 1723-1732, 1940.
3. Mishra, R.K., and Mohanty, K., Pyrolysis of Cascabelathevetia seeds over ZSM-5 catalysts: fuel properties and compositional analysis. *Biomass Conversion and Biorefinery*, 12(5): 1449-1464, 2022.
4. Abnisa, F., Daud, W.W., and Sahu, J.N. Optimization and characterization studies on bio-oil production from palm shell by pyrolysis using response surface methodology. *Biomass and Bioenergy*, *35*(8): 3604-3616, 2011.
5. Mullen, C. A., and Boateng, A. A., Production of aromatic hydrocarbons via catalytic pyrolysis of biomass over Fe-modified HZSM-5 zeolites. *ACS Sustainable Chemistry & Engineering*, *3*(7), 1623-1631, 2015.
6. Sun, L., Zhang, X., Chen, L., Zhao, B., Yang, S., and Xie, X., Comparision of catalytic fast pyrolysis of biomass to aromatic hydrocarbons over ZSM-5 and Fe/ZSM-5 catalysts. *Journal of Analytical and Applied Pyrolysis*, 121: 342-346, 2016.
7. Veses, A., Puértolas, B., Callén, M. S., and García, T., Catalytic upgrading of biomass derived pyrolysis vapors over metal-loaded ZSM-5 zeolites: Effect of different metal cations on the bio-oil final properties. *Microporous and Mesoporous Materials*, *209*, 189-196, 2015.
8. Mihalcik, D. J., Mullen, C. A., and Boateng, A. A., Screening acidic zeolites for catalytic fast pyrolysis of biomass and its components. *Journal of Analytical and Applied Pyrolysis*, *92*(1), 224-232, 2011.
9. Wang, W., Li, X., Ye, D., Cai, L., and Shi, S. Q., Catalytic pyrolysis of larch sawdust for phenol-rich bio-oil using different catalysts. *Renewable Energy*, *121*, 146-152, 2018.

10. Al-Otaibi NM, Hutchings G. Aromatization of isobutene using h-zsm-5/oxide composite catalysts. Catal. letters, 2010; 134(3-4): 191-195
11. Bach, Q. V., and Chen, W.H., Pyrolysis characteristics and kinetics of microalgae via thermogravimetric analysis (TGA): A state-of-the-art review. *Bioresource Technology*, *246*, 88-100, 2017.
12. Vyazovkin, S., Burnham, A. K., Criado, J. M., Pérez-Maqueda, L. A., Popescu, C., and Sbirrazzuoli, N., ICTAC Kinetics Committee recommendations for performing kinetic computations on thermal analysis data. *Thermochimica acta*, *520*(1-2), 1-19, 2011.
13. Tinoco, I.Jr, Sauer, K., Wang, J.C., and Puglisi, J.D., Physical chemistry principles and application in biological sciences, 4th Ed. pp384, Pearson India Education Services Pvt. Ltd, Noida, 2006; ISBN 978 81 317 0975-7.
14. Vuppaladadiyam, A. K., Memon, M. Z., Ji, G., Raheem, A., Jia, T. Z., Dupont, V., & Zhao, M. (2018). Thermal characteristics and kinetic analysis of woody biomass pyrolysis in the presence of bifunctional alkali metal ceramics. *ACS sustainable chemistry & engineering*, *7*(1), 238-248.
15. Szostak, R. Molecular sieves: principles of synthesis and identification. 2nd ed. London; New York: Blackie Academic & Professional; 1998.
16. Razzaq, M., Zeeshan, M., Qaisar, S., Iftikhar, H., and Muneer, B. Investigating use of metal-modified HZSM-5 catalyst to upgrade liquid yield in co-pyrolysis of wheat straw and polystyrene. *Fuel 257:* 116119, 2019.
17. Yang, Z., Kumar, A., and Apblett, A. Integration of biomass catalytic pyrolysis and methane aromatization over Mo/HZSM-5 catalysts. *Journal of analytical and applied pyrolysis*, *120*, 484-492, 2016.
18. Zhang, S., Zhang, H., Liu, X., Zhu, S., Hu, L., and Zhang, Q., Upgrading of bio-oil from catalytic pyrolysis of pretreated rice husk over Fe-modified ZSM-5 zeolite catalyst. *Fuel Processing Technology*, *175*, 17-25, 2018.
19. Zheng, Y., Wang, F., Yang, X., Huang, Y., Liu, C., Zheng, Z., and Gu, J., Study on aromatics production via the catalytic pyrolysis vapor upgrading of biomass using metal-loaded modified H-ZSM-5. *Journal of Analytical and Applied Pyrolysis*, *126*, 169-179, 2017.
20. Iliopoulou, E. F., Stefanidis, S. D., Kalogiannis, K. G., Delimitis, A., Lappas, A. A., and Triantafyllidis, K. S., Catalytic upgrading of biomass pyrolysis vapors using

transition metal-modified ZSM-5 zeolite. *Applied Catalysis B: Environmental*, *127*, 281-290, 2012.

21. Dyer, A. C., Nahil, M. A., and Williams, P. T., Biomass: polystyrene co-pyrolysis coupled with metal-modified zeolite catalysis for liquid fuel and chemical production. *Journal of Material Cycles and Waste Management*, *24*(2), 477-490, 2022.
22. Ding, Y. L., Wang, H. Q., Xiang, M., Yu, P., Li, R. Q., and Ke, Q. P., The effect of Ni-ZSM-5 catalysts on catalytic pyrolysis and hydro-pyrolysis of biomass. *Frontiers in Chemistry*, *8*, 790, 2020.
23. Núñez, F., Chen, L., Wang, J.A., Flores, S.O., Salmones, J., Arellano, U., and Tzompantzi, F. Bifunctional Co_3O_4/ZSM-5 mesoporous catalysts for biodiesel production via esterification of unsaturated omega-9 oleic acid. *Catalysts, 12*(8): 900, 2022.
24. Khawam, A., and Flanagan, D.R. Solid-state kinetic models: basics and mathematical fundamentals. *The journal of physical chemistry B, 110*(35), 17315-17328, 2006.
25. Radojevic, M., Jankovic, B., Jovanovic, V., Stojiljkovic, D., and Manic, N. Comparative pyrolysis kinetics various biomasses based on model-free and DAEM approaches improved with numerical optimization procedure. *PLoS ONE, 13(10):* e0206657, 2018.
26. Loy, A.C.M., Gan, D.K.W., Yusup, S., Chin, B.L.F., Lam, M.K., Shahbaz, M., Unrean, P., Acda, M.N., and Rianawati, E., Thermogravimetric kinetic modelling of in-situ catalytic pyrolytic conversion of rice husk to bioenergy using rice hull ash catalyst, *Bioresource Technology*, 261: 213-222, 2018.
27. Lifshitz, C., Some recent aspects of unimolecular gas phase ion chemistry. *Chemical Society Reviews*, *30*(3), 186-192, 2001.
28. Espenson, J.H., Chemical kinetics and reaction mechanisms, first edn. pp 122, McGraw Hill, New Delhi, 1981.
29. Atkins, P., and De Paula, J. Atkin's Physical Chemistry, 10th Edn, p 899, Oxford University Press, New Delhi, 2014.
30. Chen, B.H., Chao, Z.S., He, H., Huang, C., Liu, Y.J., Yi, W.J., and Wei, X.L. Towards a full understanding of the nature of Ni (II) species and hydroxyl groups over highly siliceous HZSM-5 zeolite supported nickel catalysts prepared by a deposition–precipitation method. *Dalton Transactions*, 45 (6), 2720–2739, 2016.

31. Nanda, S., Pattnaik, F., Borugadda, V. B., Dalai, A. K., Kozinski, J. A., and Naik, S. Catalytic and noncatalytic upgrading of bio-oil to synthetic fuels: an introductory review. *Catalytic and Noncatalytic Upgrading of Oils*, ACS Symposium Series: Vol. 1379, 1-28, 2021.